

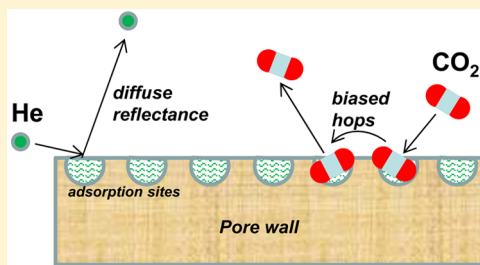
# Investigating the Validity of the Knudsen Diffusivity Prescription for Mesoporous and Macroporous Materials

Rajamani Krishna\*

Van 't Hoff Institute for Molecular Sciences, University of Amsterdam, Science Park 904, 1098 XH Amsterdam, The Netherlands

**S** Supporting Information

**ABSTRACT:** The primary objective of this article is to investigate the validity of the Knudsen prescription for pore diffusivity. Published experimental data on transient permeation of He–Ar, He–N<sub>2</sub>, He–CO<sub>2</sub>, He–C<sub>3</sub>H<sub>8</sub>, and CO<sub>2</sub>–C<sub>3</sub>H<sub>8</sub> mixtures across mesoporous and macroporous membranes are analyzed using the Maxwell–Stefan (M–S) formulation, combining molecule–wall and molecule–molecule interactions. For He–Ar and He–N<sub>2</sub> mixtures, both components are poorly adsorbed within the pores, and the experimental permeation data can be modeled adequately taking M–S diffusivity for molecule–wall interactions,  $\mathcal{D}_i = D_{i,Kn}$  the corresponding Knudsen diffusivity. For He–CO<sub>2</sub> and He–C<sub>3</sub>H<sub>8</sub> mixture permeation, the equality  $\mathcal{D}_i = D_{i,Kn}$  holds only for He. For either CO<sub>2</sub> or C<sub>3</sub>H<sub>8</sub>,  $\mathcal{D}_i$  is lower than  $D_{i,Kn}$  by a factor ranging from 0.55 to 0.98, depending on the species and operating temperature. The stronger the adsorption strength, the lower the ratio  $\mathcal{D}_i/D_{i,Kn}$ . The observed lowering in the M–S diffusivity below the Knudsen value,  $D_{i,Kn}$  is in line with the published Molecular Dynamics (MD) data for cylindrical mesopores. The Knudsen prescription is based on the requirement that a molecule experiences diffuse reflection on collision with the pore wall, i.e., the angle of reflection bears no relation to the angle of incidence. Adsorption at the pore wall introduces a bias that makes a molecule hop to a neighboring site on the surface rather than return to the bulk; this bias increases with increasing adsorption strength and has the effect of reducing the pore diffusivity.



## 1. INTRODUCTION

The proper description of diffusion inside a porous matrix is important in a wide variety of contexts such as catalysis, adsorption, membrane separations, and exploitation of shale gas reserves. Because of the wide range of pore sizes encountered in practice, typically  $0.3 \text{ nm} < d_p < 200 \text{ nm}$ , there is a wide variation in the characteristics of the diffusivities. For example, the organic matter in shale reservoirs have pore sizes in the range of  $2 \text{ nm} < d_p < 50 \text{ nm}$ .<sup>1,2</sup> To set the scene for this article and to underscore the influence of pore diameter,  $d_p$ , on diffusion mechanisms, consider the interactions between guest molecules He, Ar, CH<sub>4</sub>, and CO<sub>2</sub> and the walls of a silica pore. The Lennard–Jones (L–J) interaction potential with the pore wall, normalized with respect to  $RT$ , is shown in Figure 1. The minimum in the potential energy occurs at a distance  $\approx 2^{1/6} \sigma$ , where  $\sigma$  is the L–J size parameter. Of the four species, CO<sub>2</sub> has the highest adsorption strength, and this is evidenced by the deep well in the interaction energy. The energies of interaction follow the hierarchy  $\text{CO}_2 > \text{CH}_4 > \text{Ar} > \text{He}$ . For distances greater than about 0.7 nm from the pore wall, the interaction potential is virtually zero for all three species. This implies that for mesoporous ( $2 \text{ nm} < d_p < 50 \text{ nm}$ ) and macroporous materials ( $d_p > 50 \text{ nm}$ ), there is a central core region where the influence of interactions of the molecules with the pore wall is either small or negligible. The threshold value of  $d_p = 50 \text{ nm}$  for transition from mesopore to the macropore category is rather arbitrary; both mesopore and macropore diffusion are governed by a combination of molecule–molecule and molecule–wall interactions.

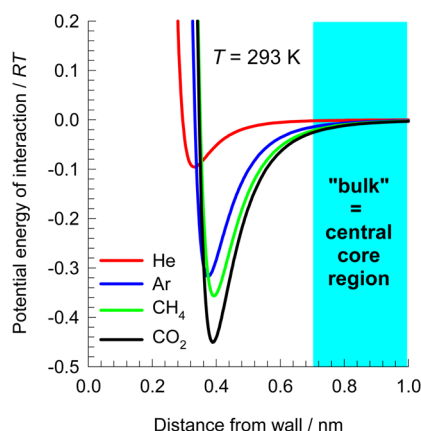


**Figure 1.** Lennard–Jones interaction potential, normalized with respect to  $RT$ , for He, Ar, CH<sub>4</sub>, and CO<sub>2</sub> and a silica pore wall. The parameter values are taken from Talu and Myers.<sup>36</sup>

The Maxwell–Stefan (M–S) formulation, which has its basis in irreversible thermodynamics, provides a unified framework for modeling diffusion in porous materials.<sup>3,4</sup>

**Received:** February 25, 2016

**Revised:** April 1, 2016

**Accepted:** April 1, 2016

**Published:** April 1, 2016

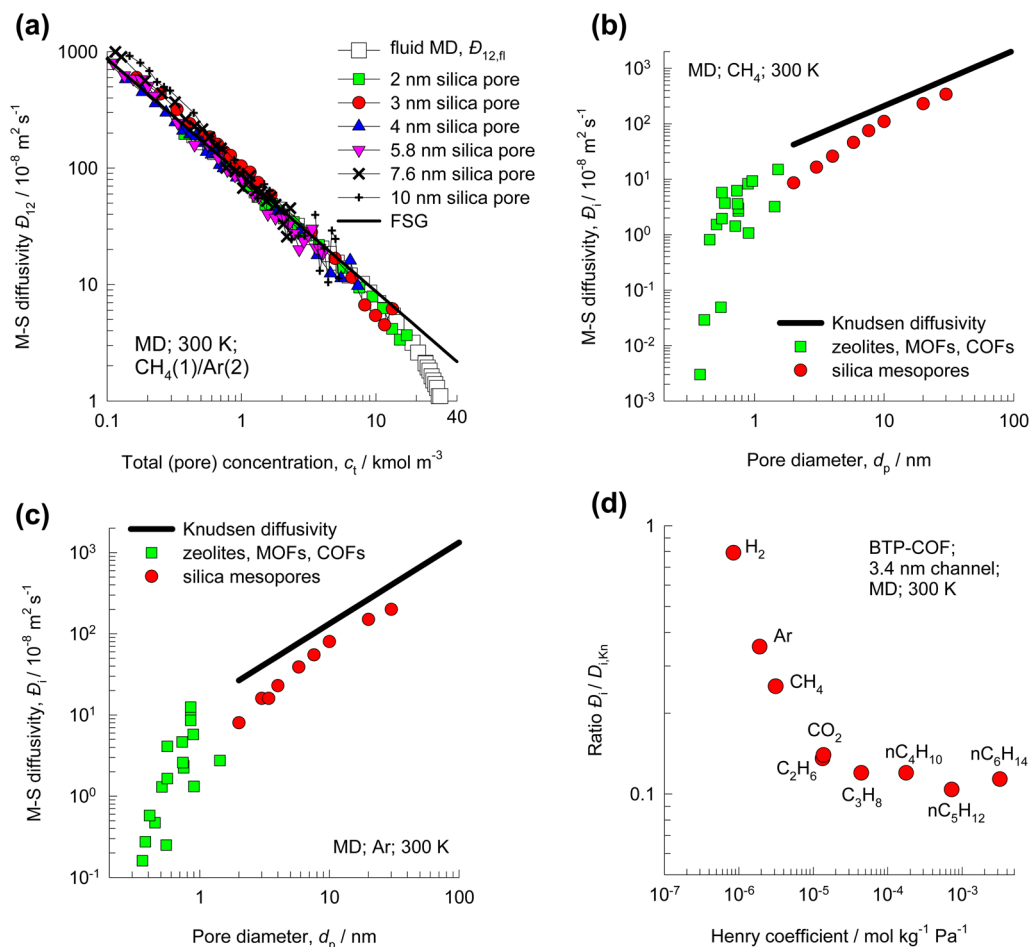


**Figure 2.** (a) MD data<sup>3,4</sup> on the Maxwell-Stefan diffusivity  $D_{12}$ , for equimolar ( $c_1 = c_2$ ) binary mixture of  $\text{CH}_4$ –Ar in silica pores with diameters in the range of 2–10 nm. Also shown (square symbols) are the  $D_{12,\text{fl}}$  data for binary fluid  $\text{CH}_4$ –Ar mixture diffusion. (b and c) M-S diffusivity at zero-loading,  $D_i$ , of (b)  $\text{CH}_4$  and (c) Ar in zeolites, MOFs, and silica mesopores. The data has been culled from various MD simulation data sources.<sup>3,8,9</sup> (d) Ratio of the MD data<sup>12</sup> on the zero-loading M-S diffusivity to the calculated Knudsen diffusivity,  $D_i/D_{i,Kn}$ , for various guest molecules ( $\text{H}_2$ , Ar,  $\text{CH}_4$ ,  $\text{C}_2\text{H}_6$ ,  $\text{C}_3\text{H}_8$ ,  $\text{nC}_4\text{H}_{10}$ ,  $\text{nC}_5\text{H}_{12}$ , and  $\text{nC}_6\text{H}_{14}$ ) in BTP-COF, plotted as a function of the Henry coefficient for adsorption.

$$-\varepsilon \frac{c_i}{RT} \frac{\partial \mu_i}{\partial z} = \sum_{j=1, j \neq i}^n \left( \frac{x_j N_i - x_i N_j}{D_{ij}} \right) + \frac{N_i}{D_i}; \quad i = 1, 2, \dots, n \quad (1)$$

In eq 1,  $c_i$  is the molar concentration of species  $i$  based on the accessible pore volume,  $x_i \equiv c_i/c_t$  is mole fraction, and the fluxes  $N_i$  are defined as the moles transported per  $\text{m}^2$  of total external surface area of the porous material:

$$N_i \equiv \varepsilon c_i u_i; \quad i = 1, 2, \dots, n \quad (2)$$

The species velocities  $u_i$  are defined in a reference framework with respect to the pore walls. The porosity  $\varepsilon$  appears on the left member of eq 1 because only a fraction  $\varepsilon$  of the external surface is available for influx or efflux of guest molecules. Molecule ( $i$ )–wall interactions are quantified by the diffusivity  $D_i$ ; molecule ( $i$ )–molecule ( $j$ ) interactions are characterized by the  $D_{ij}$  coefficients.

For mesoporous, and macroporous materials with the fluid phase in the gaseous state,  $c_i = \frac{p_i}{RT}$ ;  $\frac{\partial \mu_i}{\partial z} = \frac{RT}{p_i} \frac{\partial p_i}{\partial z}$  and eq 1 simplifies to

$$-\varepsilon \frac{1}{RT} \frac{\partial p_i}{\partial z} = \sum_{j=1, j \neq i}^n \left( \frac{x_j N_i - x_i N_j}{D_{ij}} \right) + \frac{N_i}{D_i}; \quad i = 1, 2, \dots, n \quad (3)$$

Extensive sets of Molecular Dynamics (MD) simulation data for unary and binary mixtures of species in mesopores with diameters in the range of 2–10 nm<sup>3,4</sup> provide insights into the magnitude and characteristics of the M-S diffusivities  $D_{ij}$  and  $D_i$ .

As illustration, Figure 2a presents MD data on M-S diffusivity  $D_{12}$  for equimolar ( $c_1 = c_2$ ) binary  $\text{CH}_4$ –Ar mixtures in silica mesopores. Also shown (square symbols) are the  $D_{12,\text{fl}}$  data for binary fluid mixture diffusion, obtained from independent MD simulations. The molecule–molecule interactions are independent of the pore diameter and equal the corresponding values of the fluid phase diffusivity. The straight line represents the estimations of the gas-phase diffusivity  $D_{12,\text{fl}}$  using the Fuller–Schettler–Giddings method.<sup>5,6</sup> The MD data suggest that the FSG method can be used to provide accurate estimations of the M-S diffusivity  $D_{12}$  in mesopores and macropores.

The M-S diffusivity  $D_i$  is to be interpreted as an inverse drag coefficient between the guest molecule species  $i$  and the pore wall. Figure 2b,c presents MD data on the M-S diffusivity of  $\text{CH}_4$  and Ar in silica mesopores, along with data for microporous zeolites, metal–organic frameworks (MOFs), and covalent

organic frameworks (COFs). Also shown in Figure 2b,c are the calculations for the Knudsen diffusivity values

$$D_{i,Kn} = \frac{d_p}{3} \sqrt{\frac{8RT}{\pi M_i}} \quad (4)$$

We note that the MD data fall consistently below the values prescribed by eq 4; this departure is the main focus of this article. For gases such as H<sub>2</sub> and He that have poor adsorption strength, MD data<sup>3,4,7–12</sup> show that the M-S diffusivity  $\mathcal{D}_i$  equals the Knudsen diffusivity. For guest molecules that have finite adsorption on the pore walls, the M-S diffusivity  $\mathcal{D}_i$  is found to be significantly lower than the value predicted by eq 4. Adsorption on the pore walls causes the molecules to bind to the wall and perhaps hop to a neighboring adsorption site rather than return to the bulk after collision; this introduces a bias in the molecular hops (see Abstract graphic). This bias increases with increasing adsorption strength, causing a violation of the diffuse reflectance assumption that is invoked in deriving eq 4.<sup>3,7,10</sup> The biased hops are best appreciated by viewing the video animations provided in earlier work<sup>3</sup> that trace the hopping trajectories of H<sub>2</sub>, Ar, and CH<sub>4</sub> within a 2 nm silica pore. The departures from the Knudsen prescription correlate with the binding energy for adsorption of the molecules at the pore walls.<sup>12,13</sup> As illustration, Figure 2d presents MD data on  $\mathcal{D}_i/D_{i,Kn}$  for a number of guest species in BTP-COF,<sup>12,13</sup> a COF that has 3.4 nm hexagonal channels. The  $\mathcal{D}_i/D_{i,Kn}$  values range from approximately unity for H<sub>2</sub> to a value of 0.1 for *n*-hexane (*n*C6). Furthermore,  $\mathcal{D}_i/D_{i,Kn}$  is seen to correlate very well with the Henry coefficient for adsorption. The higher the adsorption strength, the higher the sticking tendency of that species with the pore wall, leading to diminished pore mobility.

Bhatia and co-workers<sup>14–18</sup> have reanalyzed a variety of experimental data for diffusion in mesopores in order to demonstrate the failure of the Knudsen formula; they provide a rationalization of the departure from the Knudsen prescription in terms of an oscillator model that quantifies the nonlinear molecular trajectories resulting from adsorption at the pore walls.

The validity of the Knudsen prescription has been the subject of some debate in the literature.<sup>14,18–21</sup> Particularly noteworthy is the observation made by D.M. Ruthven:<sup>20</sup> “molecular dynamic simulations ... have suggested that the Knudsen model fails when there is significant surface adsorption. ...no experimental evidence was given to support such a conclusion, but, if it turns out to be correct, this would require a major change in our approach to the modelling and design of catalysts and adsorbents...”. In his reanalysis of the diffusivity data of Reyes et al.,<sup>22</sup> Ruthven<sup>21</sup> has concluded that the Knudsen formula holds with good accuracy. In the work of Higgins et al.,<sup>23</sup> the steady-state permeation of He, Ar, N<sub>2</sub>, CH<sub>4</sub>, C<sub>3</sub>H<sub>8</sub>, and CO<sub>2</sub> across mesoporous silica membrane have been investigated. Even though the molar masses of C<sub>3</sub>H<sub>8</sub> and CO<sub>2</sub> are the same, their component permeances differ by about 25%.

The primary objective of this article is to obtain confirmation of the influence of adsorption strength on the M-S diffusivity  $\mathcal{D}_i$  using published experimental data. For this purpose, we reinterpret and reanalyze the experimental data of Tuchlenski et al.,<sup>24</sup> Yang et al.,<sup>25</sup> and Veldsink et al.<sup>26</sup> for transient binary mixture permeation across mesoporous and macroporous membranes. Attempting to match experimental data on transient mixture diffusion places greater demands on the M-S model parameters than the matching of steady-state characteristics.

Consequently, it is easier to discriminate between different model assumptions.

The secondary objective is to compare and contrast the membrane permeation results obtained from the M-S eq 3, with those using the dusty gas model (DGM):<sup>27</sup>

$$\begin{aligned} & -\varepsilon \frac{p_t}{RT} \frac{\partial x_i}{\partial z} - \varepsilon \left( \frac{x_i}{RT} \right) \left( \frac{B_0 p_t}{\eta D_{i,Kn}} + 1 \right) \frac{\partial p_t}{\partial z} \\ & = \sum_{j=1}^n \left( \frac{x_j N_j - x_i N_j}{\mathcal{D}_{ij}} \right) + \frac{N_i}{D_{i,Kn}}; \quad i = 1, 2, \dots, n \end{aligned} \quad (5)$$

There are important differences between the two approaches. In the DGM, the term containing the permeability,  $B_0$ , quantifies the viscous flow contribution; the treatment of this contribution is the subject of intense debate and criticism.<sup>28,29</sup> In the M-S approach, the viscous flow contribution is subsumed into the M-S diffusivities  $\mathcal{D}_i$  and  $\mathcal{D}_{ij}$ .<sup>30</sup>

In the DGM, the influence of species adsorption on the pore walls is treated differently; the motion of adsorbed molecules along the surface of the pore walls is accounted for as an additional, parallel contribution to the fluxes (see schematic in Figure 3)<sup>24,27</sup>

$$N_{i,surface} = -\mathcal{D}_{i,s} \frac{c_i}{RT} \frac{d\mu_i}{dz}; \quad i = 1, 2, \dots, n \quad (6)$$

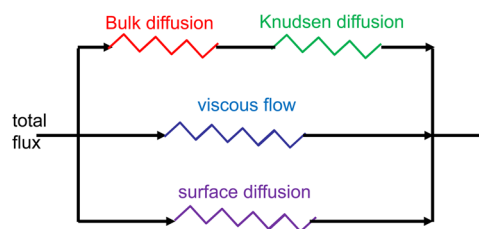


Figure 3. Electric analog circuit picturing the flux of the diffusing species within a porous medium. Adapted from Mason and Malinauskas.<sup>27</sup>

In eq 6,  $c_i$  represents the concentration of species  $i$  in the adsorbed phase that is dictated by adsorption equilibrium. The combination of eq 5 with eq 6 has been illustrated by Argönül and Keil<sup>31</sup> for pore diffusion, by Tuchlenski et al.<sup>24</sup> for membrane permeation, and by Wu et al.<sup>2</sup> for transport in shale reservoirs. In the M-S eq 3, as applied to mesoporous materials, there is no additional accounting for surface diffusion.

The Supporting Information accompanying this article provides detailed discussions and comparisons between the DGM and the M-S formulations.

## 2. TRANSIENT MIXTURE PERMEATION WITH POORLY ADSORBING GASES

Figure 4 presents a schematic of the two-compartment membrane setup used in the dynamic experiments reported by Tuchlenski et al.,<sup>24</sup> Yang et al.,<sup>25</sup> and Veldsink et al.<sup>26</sup> The two compartments are separated by a porous membrane. The Tuchlenski and Yang experiments are for a mesoporous Vycor glass membrane, with an average pore size of the membrane  $d_p \approx 4$  nm. The Veldsink experiments are for an alumina membrane with an average pore diameter  $d_p \approx 100$  nm.

The transient membrane experiments reported by the three different authors are analogous in character. The upstream

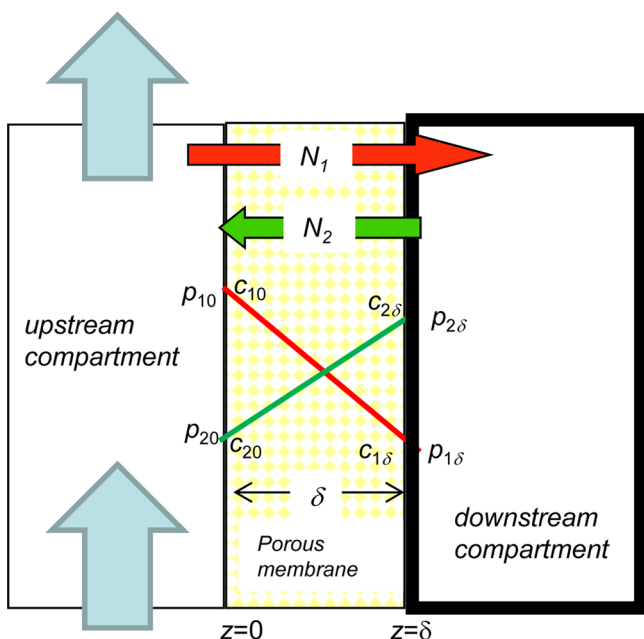


**Figure 4.** Schematic showing the two-compartment membrane setup used in the experiments reported by Tuchlenski et al.,<sup>24</sup> Yang et al.,<sup>25</sup> and Veldsink et al.<sup>26</sup>

compartment is maintained at constant composition by maintaining a through-flow of the gas mixture at constant composition. The total system pressure in the upstream compartment is  $10^5$  Pa. The downstream compartment is closed and is initially maintained at  $p_{i0} = 10^5$  Pa. To elucidate the experiments, let us consider the data reported by Tuchlenski et al.<sup>24</sup> for He(1)–Ar(2) mixtures at 293 K; their data are indicated by the circle and square symbols in Figure 5a. For each mixture, two sets of experiments were performed. In the first set of experiments, the downstream compartment is initially filled with pure Ar, and the upstream compartment is fed with pure He. Initially, the total system pressure in the downstream compartment is  $p_{i0} = 10^5$  Pa. Because of rapid diffusion of He into the downstream compartment, the total pressure,  $p_t$ , in the downstream compartment increases in magnitude. This pressure increase,  $(p_t - p_{i0})$ , is measured and is indicated in Figure 5a by circles. The system will evolve to a steady state wherein the total downstream pressure will equilibrate to  $10^5$  Pa, corresponding also to the total system pressure in the upstream compartment.

In the second experiment, the compositions in the upstream and downstream compartments are reversed. Initially, the downstream compartment contains pure He and the upstream compartment is fed and flushed with pure Ar. The rapid efflux of He from the downstream compartment, with concomitant influx of Ar, results in a decrease in the downstream pressure,  $p_i$ ; the experimental data are shown by the square symbols in Figure 5a.

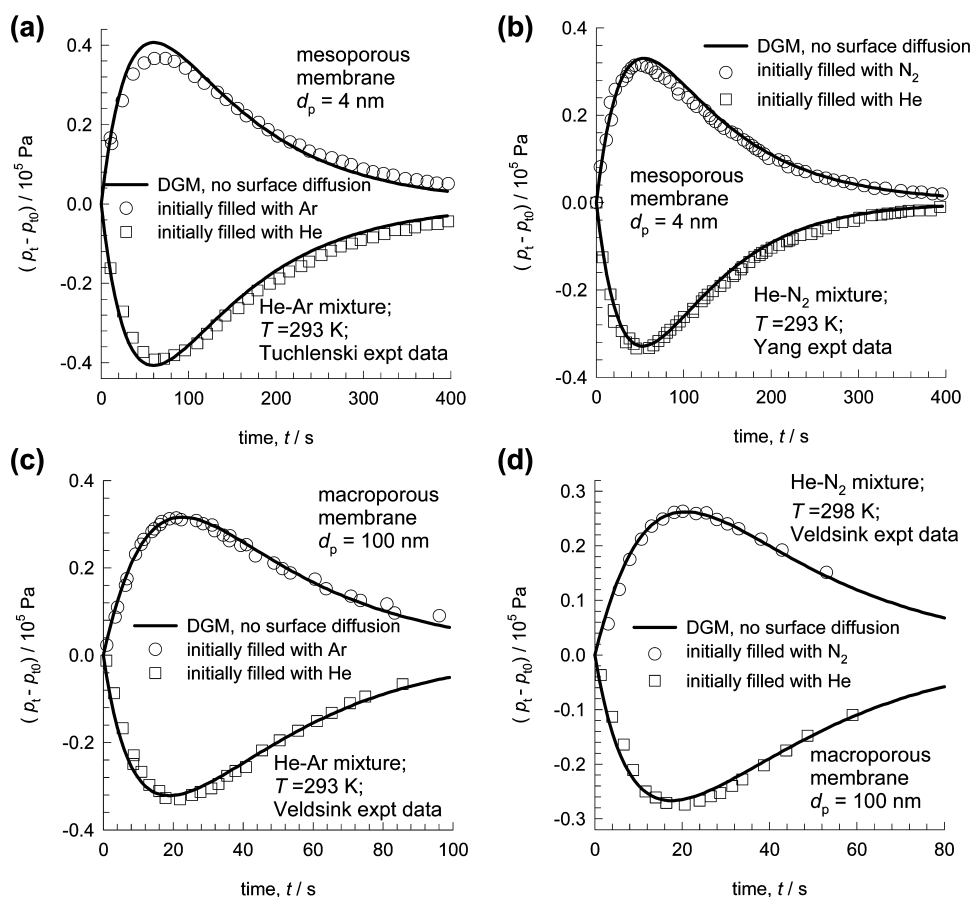


**Figure 5.** Experimental data of for the dynamic pressure increase in the downstream for (a) He–Ar mixtures at 293 K,<sup>24</sup> (b) He–N<sub>2</sub> mixtures at 293 K,<sup>25</sup> (c) He–Ar mixtures at 293 K,<sup>26</sup> and (d) He–N<sub>2</sub> mixtures at 298 K.<sup>26</sup> The continuous solid lines are the calculations using the DGM model using the structural parameters as provided in Tables S2–S4.

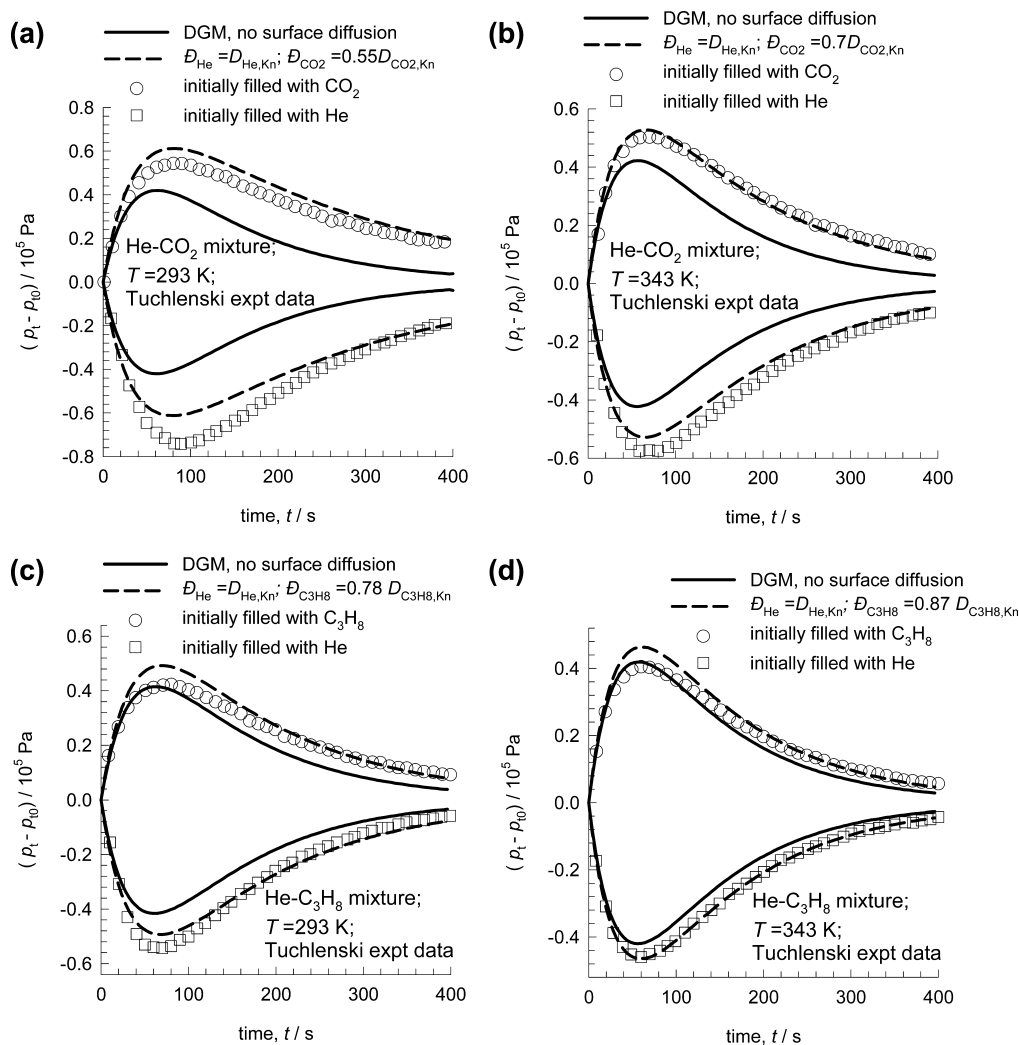


**Figure 6.** Experimental data of Tuchlenski et al.<sup>24</sup> for the dynamic pressure increase in the downstream compartment for (a) He–CO<sub>2</sub> mixtures at 293 K, (b) He–CO<sub>2</sub> mixtures at 343 K, (c) He–C<sub>3</sub>H<sub>8</sub> mixtures at 293 K, and (d) He–C<sub>3</sub>H<sub>8</sub> mixtures at 343 K. The continuous solid lines are the calculations using the DGM, neglecting surface diffusion. The dashed lines are the calculations using the M-S model with adjusted M-S diffusivities.

For each set of experiments, the precise structural characteristics of the membrane porosity,  $\varepsilon$ , and tortuosity,  $\tau$ , were determined by performing unary permeation experiments with noble gases; these data were used in our simulations (see Tables S2–S4 for details). For diffusion of binary gas mixtures in mesopores, eq 3 may be recast in 2D matrix notation to enable explicit calculation of the fluxes

$$\begin{pmatrix} N_1(t) \\ N_2(t) \end{pmatrix} = \frac{(\varepsilon/\tau)}{RT\delta} \begin{bmatrix} \frac{1}{D_1} + \frac{x_2}{D_{12}} & -\frac{x_1}{D_{12}} \\ -\frac{x_2}{D_{12}} & \frac{1}{D_2} + \frac{x_1}{D_{12}} \end{bmatrix}^{-1} \begin{pmatrix} p_{10} - p_1(t) \\ p_{20} - p_2(t) \end{pmatrix} \quad (7)$$

A differential balance over the “closed” downstream compartment (volume =  $V_{\text{compartment}}$ ) results in

$$V_{\text{compartment}} \frac{1}{RT} \frac{\partial p_i(t)}{\partial t} = A_{\text{membrane}} (N_1(t) + N_2(t)) \quad (8)$$

The “hold-up” of either component within the membrane layer due to any species adsorption is of negligible importance because the membrane pore volume is about 3 orders of magnitude smaller than the volume of the downstream

compartment,  $\frac{V_{\text{pore}}}{V_{\text{compartment}}} = 1.7 \times 10^{-3}$  for the Tuchlenski and Yang experiments.

The Supporting Information provides details of the solution to eq 8, in combination with the DGM and M-S model formulations.

For the experiments in Figure 5a, the viscous flow contributions to the change in the total pressure  $\frac{B_{0f} p_i}{\eta} \left( \frac{x_1}{D_{1,Kn}} + \frac{x_2}{D_{2,Kn}} \right) = 8.8 \times 10^{-3}$  is negligibly small. Because both gases are poorly adsorbing,  $D_i = D_{i,Kn}$  and there is virtually no distinction between the results obtained with the DGM and M-S model formulations. The transport fluxes are dominated by molecule–wall interactions, as is evident from the values  $\frac{D_{1,Kn}}{D_{12}} = 0.05$ , and  $\frac{D_{2,Kn}}{D_{12}} = 0.016$ . The continuous solid lines in Figure 5a are the solutions to eq 8, in combination with eq 5. There is excellent agreement between the experimental data and the DGM that coincides with the M-S model. Similar good agreement between model calculations and experimental data<sup>25</sup> for He(1)–N<sub>2</sub>(2) mixtures at 293 K is realized; see Figure 5b.

Consider next the data of Veldsink et al.<sup>26</sup> for He(1)–Ar(2) mixture permeation across a macroporous ( $d_p \approx 100$  nm) membrane; see Figure 5c. The viscous flow contribution to the change in the total pressure  $\frac{B_0 p_t}{\eta} \left( \frac{x_1}{D_{1,Kn}} + \frac{x_2}{D_{2,Kn}} \right) = 0.098$  is relatively small. The transport fluxes are dictated by both molecule–wall and molecule–molecule interactions, as is evident from the values  $\frac{D_{1,Kn}}{D_{12}} = 0.916$ , and  $\frac{D_{2,Kn}}{D_{12}} = 0.29$ . The model predictions, shown by the continuous solid lines, are in good agreement with experimental data. Similar good agreement is obtained for He(1)–N<sub>2</sub>(2) mixture permeation across the macroporous membrane; see Figure 5d.

Gruener and Huber<sup>32</sup> have conducted careful experiments to determine the diffusivities of He and Ar in silicon nanochannels. Both guest molecules have negligible adsorption strength on the silicon walls; therefore, it is not surprising that the experimental data are in good agreement with the estimations using Knudsen prescription.

Though no new fresh insights have emerged from the data presented in Figure 5 for poorly adsorbing gases, the comparisons between model calculations and experiments serve to validate the accuracy of the numerical procedures employed in the simulations.

### 3. TRANSIENT PERMEATION OF ADSORBING GASES ACROSS MESOPOROUS MEMBRANES

Tuchlenski et al.<sup>24</sup> report experimental data for dynamic pressure changes during permeation of He–CO<sub>2</sub> and He(1)–C<sub>3</sub>H<sub>8</sub>(2) mixtures at 293 and 343 K. Their experimental data are shown by the circle and square symbols in Figure 6a–d. The simulations using the DGM, neglecting surface diffusion, tend to underestimate severely the magnitude of the overshoots and undershoots in the downstream pressure in the He–CO<sub>2</sub> experiments. Tuchlenski et al.<sup>24</sup> properly recognize that the deviations are due to finite adsorption on the pore walls of CO<sub>2</sub> and C<sub>3</sub>H<sub>8</sub>. The authors have also measured the adsorption isotherms for CO<sub>2</sub> and C<sub>3</sub>H<sub>8</sub> at 293 and 343 K. On the basis of the unary isotherm data, we note that CO<sub>2</sub> has a stronger adsorption strength than C<sub>3</sub>H<sub>8</sub>, most likely due to Coulombic interactions with the pore wall.

In applying the M-S eqs 3 to model the Tuchlenski experiments in Figure 6, there is only one adjustable parameter,  $\mathcal{D}_{CO_2}$  or  $\mathcal{D}_{C_3H_8}$ , for each experimental set. Because the MD data for silica mesopores indicate that the M-S diffusivity  $\mathcal{D}_i$  is lowered with increasing adsorption strength, we should expect the following hierarchy of M-S diffusivities:  $\mathcal{D}_{CO_2} < \mathcal{D}_{C_3H_8}$ . Because the adsorption strength decreases with increasing temperature, we should also expect  $\mathcal{D}_{CO_2,293K} < \mathcal{D}_{CO_2,343K}$  and  $\mathcal{D}_{C_3H_8,293K} < \mathcal{D}_{C_3H_8,343K}$ .

For the He–CO<sub>2</sub> mixture permeation data at 293 and 343 K shown in Figure 6a,b, reasonably good match with experiments is obtained by taking  $\mathcal{D}_{CO_2} = 0.55D_{CO_2,Kn}$  for data at 293 K and  $\mathcal{D}_{CO_2} = 0.7D_{CO_2,Kn}$  for data at 343 K. The higher value of  $\mathcal{D}_{CO_2}$  at 343 K is because the adsorption strength is lower at the higher temperature.

For the He–C<sub>3</sub>H<sub>8</sub> mixture permeation data at 293 and 343 K in Figure 6c,d, reasonably good match with experiments is obtained by taking  $\mathcal{D}_{C_3H_8} = 0.78D_{C_3H_8,Kn}$  for data at 293 K and  $\mathcal{D}_{C_3H_8} = 0.87D_{C_3H_8,Kn}$  for data at 343 K. The higher value of  $\mathcal{D}_{C_3H_8}$

at 343 K is because the adsorption strength is lower at the higher temperature.

Tuchlenski et al.<sup>24</sup> have also published experimental data for CO<sub>2</sub>(1)–C<sub>3</sub>H<sub>8</sub>(2) mixtures at 293 K; see Figure 7a. The two sets of experiments are for switching pure CO<sub>2</sub> with 1:1 CO<sub>2</sub>/C<sub>3</sub>H<sub>8</sub> mixture and vice versa. In this case, the DGM predicts no pressure increase or decrease. To rationalize this observation, we sum eq 5 over both species to obtain

$$-\frac{1}{RT} \left( 1 + \frac{B_0 p_t}{\eta} \sum_{i=1}^2 \frac{x_i}{D_{i,Kn}} \right) \frac{\partial p_t}{\partial z} = \sum_{i=1}^2 \frac{N_i}{D_{i,Kn}} \quad (9)$$

Because both CO<sub>2</sub> and C<sub>3</sub>H<sub>8</sub> have equal molar masses,  $D_{CO_2,Kn} = D_{C_3H_8,Kn}$ , eq 9 predicts that for equimolar counter-diffusion in the binary mixture there should be no change in the total pressure.

The experimental data in Figure 7a provide us with an opportunity to test the predictive capability of the M-S formulation because the values  $\mathcal{D}_{CO_2} = 0.55D_{CO_2,Kn}$  and  $\mathcal{D}_{C_3H_8} = 0.78D_{C_3H_8,Kn}$  at 293 K are already available from the earlier fits shown in Figure 6. The dashed lines in Figure 7a are the calculations from the M-S model using the same input data values. The agreement between the simulations and experimental data is reasonably good and confirms the predictive capability of the M-S theory.

The M-S model calculations are extremely sensitive to the choice of the values of the M-S diffusivities  $\mathcal{D}_{CO_2}$  and  $\mathcal{D}_{C_3H_8}$ . To demonstrate this, we compare the experimental data with different scenarios for  $\mathcal{D}_{CO_2}$  while maintaining the value  $\mathcal{D}_{C_3H_8} = 0.78D_{C_3H_8,Kn}$ . For the experiment in which the downstream compartment is pure CO<sub>2</sub> and the upstream compartment contains a 1:1 CO<sub>2</sub>/C<sub>3</sub>H<sub>8</sub> mixture of constant composition, the M-S model calculations taking  $\mathcal{D}_{CO_2}$  as a factor 1.0, 0.78, 0.55, and 0.45 times the Knudsen prescription are shown in Figure 7b. For the choice  $\mathcal{D}_{CO_2} = 1.0D_{CO_2,Kn}$ , the model predicts a decrease in the downstream compartment pressure because C<sub>3</sub>H<sub>8</sub> is the tardier component in this scenario. The Knudsen prescription for CO<sub>2</sub> is clearly not valid because the experimental data show that the downstream pressure increases during equilibration. The choice  $\mathcal{D}_{CO_2} = 0.78D_{CO_2,Kn}$  anticipates no increase or decrease in the total pressure because the mobilities of both guest species are identical. Put another way, the changes in the downstream pressure are linked to differences in the mobilities of the guest molecules. The choice  $\mathcal{D}_{CO_2} = 0.45D_{CO_2,Kn}$  predicts a significantly larger increase in the downstream pressure than that observed in the experiments.

To elucidate the differences in the DGM model (neglecting surface diffusion) and the M-S model with adjusted values of  $\mathcal{D}_{CO_2}$  and  $\mathcal{D}_{C_3H_8}$ , Figure 7c provides a comparison of the transmembrane fluxes calculated by the DGM (continuous solid lines) and M-S (dashed lines) models. Because the Knudsen diffusivities of  $D_{CO_2,Kn}$  and  $D_{C_3H_8,Kn}$  are almost identical, the transmembrane fluxes sum to zero,  $N_1 + N_2 = N_t \approx 0$ , for the DGM; this follows directly from eq 9. In the M-S model, because of the stronger adsorption of CO<sub>2</sub>, this component moves more tardily within the pores. This implies that CO<sub>2</sub> vacates the downstream compartment less quickly than the influx of C<sub>3</sub>H<sub>8</sub> from the upstream compartment. The net result is a positive total

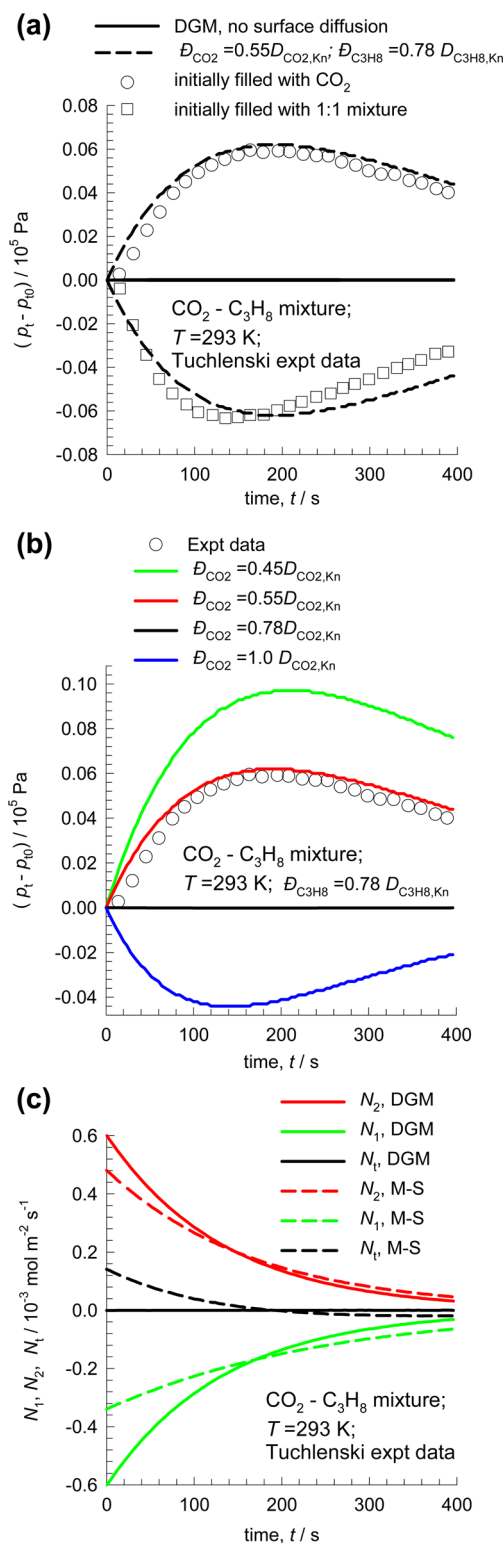


**Figure 7.** (a) Experimental data of Tuchlenski et al.<sup>24</sup> for the dynamic pressure increase in the downstream compartment for  $\text{CO}_2$ - $\text{C}_3\text{H}_8$  mixtures at 293 K. The continuous solid lines are the calculations using the DGM, neglecting surface diffusion. The dashed lines are the calculations using the M-S model, taking  $D_{\text{CO}_2} = 0.55D_{\text{CO}_2, \text{Kn}}$  and  $D_{\text{C}_3\text{H}_8} = 0.78D_{\text{C}_3\text{H}_8, \text{Kn}}$ . (b) Comparison of experimental data for the dynamic pressure increase in the downstream compartment, initially filled with  $\text{CO}_2$ , with four different scenarios for  $D_{\text{CO}_2}$ . (c) Comparing the transmembrane fluxes calculated by the DGM (continuous solid lines) and Maxwell-Stefan (dashed lines) models.

flux  $N_1 + N_2 = N_t > 0$  directed into the downstream compartment during early transience; see the dashed lines in Figure 7c.

Figure 8a presents a comparison of experimental data of Yang et al.<sup>25</sup> for the dynamic pressure increase in the downstream

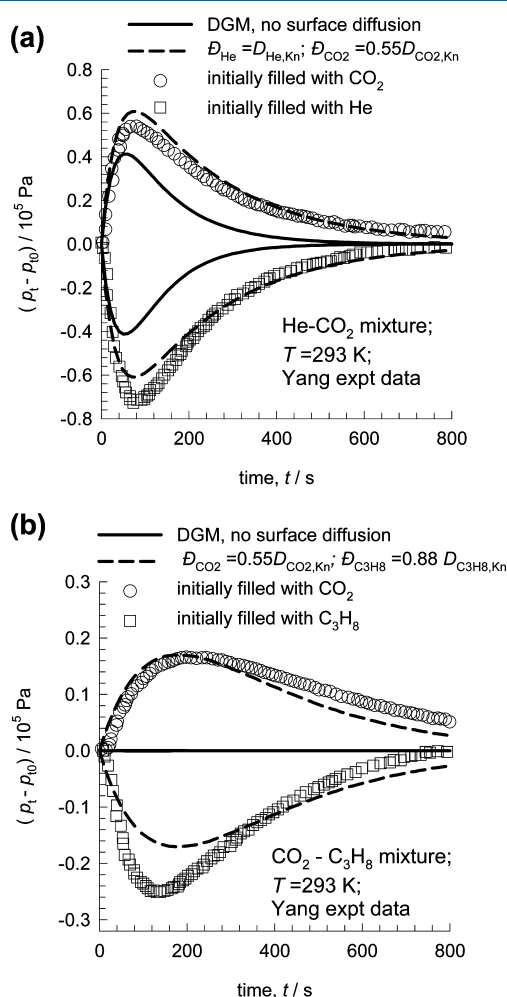


**Figure 8.** Experimental data of Yang et al.<sup>25</sup> for the dynamic pressure increase in the downstream compartment for (a) He- $\text{CO}_2$  and (b)  $\text{CO}_2$ - $\text{C}_3\text{H}_8$  mixtures at 293 K. The continuous solid lines are the calculations using the DGM, neglecting surface diffusion. The dashed lines are the calculations using the M-S model with adjusted diffusivities.

compartment for He- $\text{CO}_2$  mixtures at 293 K with model calculations. The DGM, neglecting surface diffusion, underestimates the magnitude of the pressure changes during permeation. The dashed lines are the calculations using the M-S model, taking  $D_{\text{He}} = D_{\text{He, Kn}}$  and  $D_{\text{CO}_2} = 0.55D_{\text{CO}_2, \text{Kn}}$ . The adjusted M-S diffusivity of  $\text{CO}_2$  for use in the modeling of the Yang experiments is nearly the same as that used to model the Tuchlenski experiments; the M-S diffusivity of  $\text{CO}_2$  is lowered below the corresponding Knudsen prescription because of strong adsorption on the pore walls.

Figure 8b compares the experimental data of Yang et al.<sup>25</sup> for the dynamic pressure increase for  $\text{CO}_2(1)$ - $\text{C}_3\text{H}_8(2)$  mixtures with the DGM and M-S models. The two sets of experiments are for switching pure  $\text{CO}_2$  with pure  $\text{C}_3\text{H}_8$  and vice versa. The DGM model, neglecting surface diffusion, anticipates no change in the downstream pressure because of the equal molar masses of  $\text{CO}_2$  and  $\text{C}_3\text{H}_8$ . The dashed lines are the calculations using the M-S

model, taking  $\bar{D}_{\text{CO}_2} = 0.55\bar{D}_{\text{CO}_2,Kn}$  (same value as in Figure 8a) and  $\bar{D}_{\text{C}_3\text{H}_8} = 0.88\bar{D}_{\text{C}_3\text{H}_8,Kn}$ . The M-S model is able to capture the essential characteristics of the transient pressure equilibration. These results are entirely analogous to those presented in Figure 7a for the Tuchlenski data.

Figure 9 presents a plot of the ratio  $\bar{D}_i/D_{i,Kn}$  determined in the foregoing analyses of Tuchlenski and Yang experiments plotted

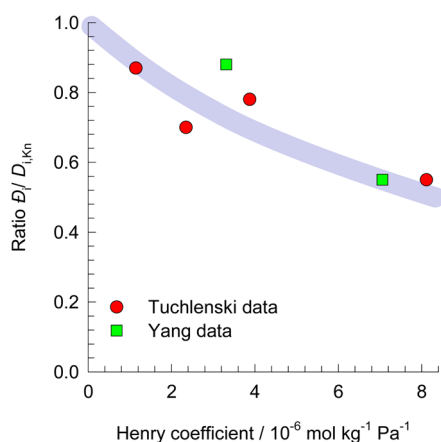


**Figure 9.** Ratio  $\bar{D}_i/D_{i,Kn}$  obtained from the simulations of Tuchlenski and Yang experiments plotted as a function of the Henry coefficient for adsorption. The calculation details are provided in the Supporting Information.

as a function of the Henry coefficient for adsorption. The data on the Henry coefficients are obtained from the unary isotherms as reported by the authors. This plot confirms that the lowering in the M-S diffusivity below the Knudsen prescription increases with increasing adsorption strength and is analogous to the data determined from MD simulations, shown in Figure 2d. The information contained in this graph provides an engineering approach to the estimation of the M-S diffusivity  $\bar{D}_i$  by using the Knudsen diffusivity  $D_{i,Kn}$  as a pivotal value.

Further experimental evidence on departure from the Knudsen prescription is provided by the experimental data reported by Petukhov and Eliseev<sup>33</sup> on the permeances

$$\Pi_i \equiv N_i / (p_{i0} - p_{i\delta}) \quad (10)$$

of  $\text{CO}_2$  and  $\text{C}_3\text{H}_8$  across an alumina membrane with an average pore diameter  $d_p = 45$  nm. Their data show that permeance of  $\text{CO}_2$  is about 90% lower than that of  $\text{C}_3\text{H}_8$ . From eq 7,  $\Pi_i = (\epsilon/\tau) \bar{D}_i/RT\delta$  for the scenario in which molecule–wall collisions dominate. The data of Petukhov indicate that  $\bar{D}_{\text{CO}_2} \approx 0.9\bar{D}_{\text{C}_3\text{H}_8}$  at variance with the expectations from eq 4.

#### 4. TRANSIENT PERMEATION OF ADSORBING GASES ACROSS MACROPOROUS MEMBRANES

Veldsink et al.<sup>26</sup> report experimental data on the dynamic pressure changes for He– $\text{CO}_2$  mixtures at 293 and 434 K; see Figure 10a,b. Good agreement is obtained with the M-S formulation taking  $\bar{D}_{\text{CO}_2} = 0.85\bar{D}_{\text{CO}_2,Kn}$  at 293 K and  $\bar{D}_{\text{CO}_2} = 0.9\bar{D}_{\text{CO}_2,Kn}$  at 434 K.

The experimental data of Veldsink et al.<sup>26</sup> for He– $\text{C}_3\text{H}_8$  mixtures at 293 and 416 K are shown in Figure 10c,d. These data can be matched very well by taking  $\bar{D}_{\text{C}_3\text{H}_8} = 0.95\bar{D}_{\text{C}_3\text{H}_8,Kn}$  at 293 K and  $\bar{D}_{\text{C}_3\text{H}_8} = 0.98\bar{D}_{\text{C}_3\text{H}_8,Kn}$  at 416 K. These M-S diffusivity

values are higher than the corresponding values for  $\text{CO}_2$  (see Figure 10a,b) because of the lower adsorption strength of  $\text{C}_3\text{H}_8$ .

For the macroporous membrane, the fitted values of  $\bar{D}_{\text{CO}_2}$  and  $\bar{D}_{\text{C}_3\text{H}_8}$  are somewhat higher than the values obtained for fitting the corresponding Tuchlenski data in Figure 6a,b. The reason is that the pore size of the membrane in the Veldsink experiments is 100 nm, considerably larger than the 4 nm pore sized membrane used in the Tuchlenski and Yang experiments. The larger the pore size, the closer the approach of the M-S diffusivity  $\bar{D}_{\text{CO}_2}$  to the Knudsen limit; this is in conformity with MD simulation data reported in the literature.<sup>10</sup> This is evidenced, for example, in Figure 2b,c, which shows MD data for  $\bar{D}_{\text{CH}_4}$  and  $\bar{D}_{\text{Ar}}$  in silica mesopores tend to approach the Knudsen value as the pore diameter increases to about 100 nm.

#### 5. SIMULATIONS OF $\text{CO}_2/\text{C}_3\text{H}_8$ PERMEATION EXPERIMENTS WITH A SURFACE DIFFUSION MODEL

In the foregoing analysis of Tuchlenski experiments with  $\text{CO}_2(1)\text{--}\text{C}_3\text{H}_8(2)$  mixtures, no explicit account was taken of surface adsorption; the pore concentrations,  $c_i$ , were determined from the bulk phase partial pressures  $c_i = \frac{p_i}{RT}$ . The model calculations were based on the assumption that the sole influence of adsorption on the pore walls is to introduce a bias in molecular hops along the surface and thereby reduce the M-S diffusivities  $\bar{D}_{\text{CO}_2}$  and  $\bar{D}_{\text{C}_3\text{H}_8}$  below those prescribed by the Knudsen formula. A different modeling approach is to assume that the mechanism of transport of both  $\text{CO}_2$ , and  $\text{C}_3\text{H}_8$  is exclusively by diffusion along the surface; in this scenario the pore concentrations,  $c_i$ , are determined from mixture adsorption equilibrium. Because molecule–molecule interactions are of negligible importance, the surface diffusion fluxes are described by eq 6.

The chemical potential gradients may be related to the gradients in the concentrations of the adsorbed species by defining a matrix of thermodynamic factors  $\Gamma_{ij}$

$$\frac{c_i}{RT} \frac{\partial \mu_i}{\partial z} = \sum_{j=1}^2 \Gamma_{ij} \frac{\partial c_j}{\partial z}; \Gamma_{ij} = \frac{c_i}{p_i} \frac{\partial p_i}{\partial c_j}; i, j = 1, 2 \quad (11)$$

The driving forces are the differences in the molar concentrations in the pore at the upstream face ( $c_{i0}$ , maintained constant) and the downstream face of the membrane ( $c_{i\delta}(t)$ , varying with time). The pore concentrations are calculated using mixed-gas Langmuir model

$$\frac{c_1}{c_{1,\text{sat}}} = \theta_1 = \frac{b_1 p_1}{1 + b_1 p_1 + b_2 p_2};$$

$$\frac{c_2}{c_{2,\text{sat}}} = \theta_2 = \frac{b_2 p_2}{1 + b_1 p_1 + b_2 p_2} \quad (12)$$

using the partial pressures  $p_{i0}$  and  $p_{i\delta}(t)$  at either faces of the membrane.

For the mixed-gas Langmuir model, eq 12, we can derive simple analytic expressions for the four elements of the matrix of thermodynamic factors:<sup>34</sup>



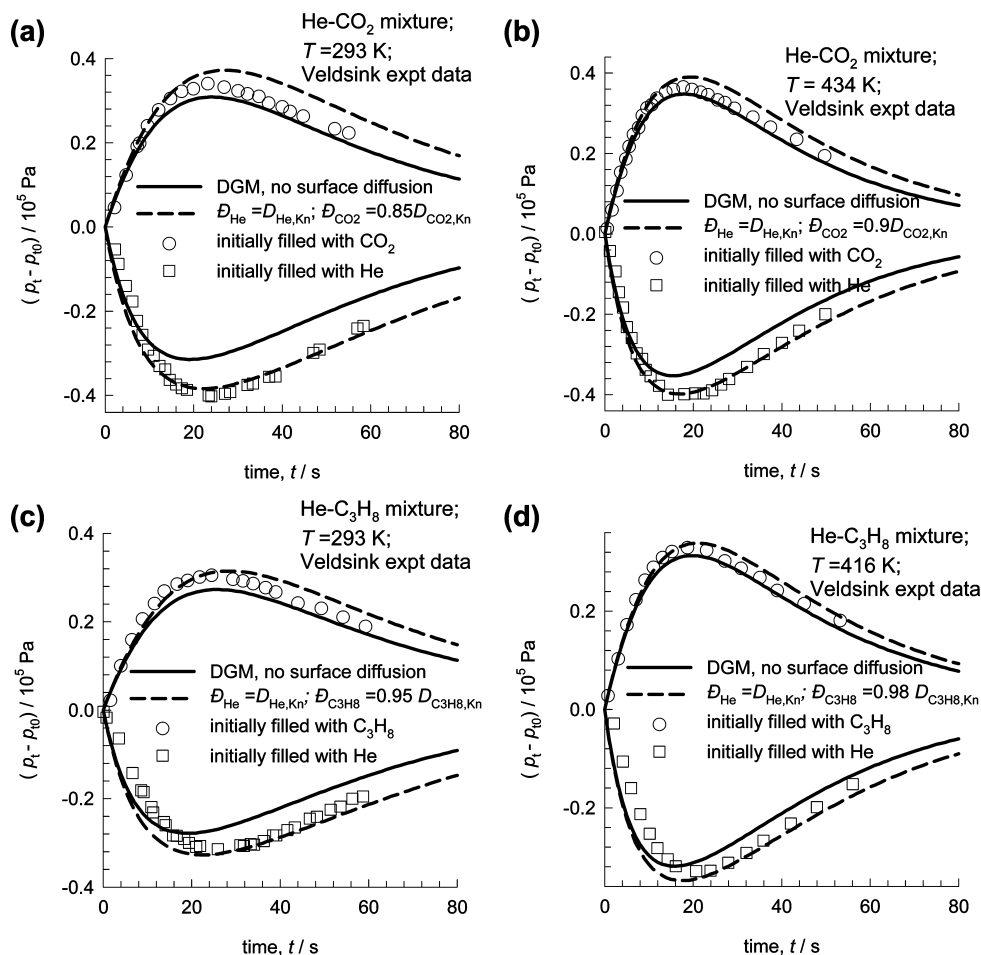


**Figure 10.** Experimental data of Veldsink et al.<sup>26</sup> for the dynamic pressure increase in the downstream compartment for (a) He–CO<sub>2</sub> at 293 K, (b) He–CO<sub>2</sub> at 434 K, (c) He–C<sub>3</sub>H<sub>8</sub> at 293 K, and (d) He–C<sub>3</sub>H<sub>8</sub> at 416 K. The continuous solid lines are the calculations using the DGM, neglecting surface diffusion. The dashed lines are the calculations using the M-S model with adjusted diffusivities.

$$\begin{bmatrix} \Gamma_{11} & \Gamma_{12} \\ \Gamma_{21} & \Gamma_{22} \end{bmatrix} = \frac{1}{1 - \theta_1 - \theta_2} \begin{bmatrix} 1 - \theta_2 & \frac{c_{1,\text{sat}}}{c_{2,\text{sat}}} \theta_1 \\ \frac{c_{2,\text{sat}}}{c_{1,\text{sat}}} \theta_2 & 1 - \theta_1 \end{bmatrix} \quad (13)$$

In 2D matrix notation, the flux relations for surface diffusion are

$$\begin{pmatrix} N_1(t) \\ N_2(t) \end{pmatrix} = \frac{(\varepsilon/\tau)}{\delta} \begin{bmatrix} \mathcal{D}_{1,s} & 0 \\ 0 & \mathcal{D}_{2,s} \end{bmatrix} \begin{bmatrix} \Gamma_{11} & \Gamma_{12} \\ \Gamma_{21} & \Gamma_{22} \end{bmatrix} \begin{pmatrix} c_{10} - c_{1\delta}(t) \\ c_{20} - c_{2\delta}(t) \end{pmatrix} \quad (14)$$

We now attempt to try to determine the surface diffusivities,  $\mathcal{D}_{i,s}$ , of CO<sub>2</sub> and C<sub>3</sub>H<sub>8</sub> by matching simulation results with experimental data on transient pressure changes in the downstream compartment. For this purpose, we assume that the  $\mathcal{D}_{i,s}$  values are independent of pore concentrations as a first approximation. A reasonably good match of the experimental data of Tuchlenski et al.<sup>24</sup> is obtained by taking the values of the M-S surface diffusivities  $\mathcal{D}_{\text{CO}_2,s} = 0.5\mathcal{D}_{\text{CO}_2,\text{Kn}}$  and  $\mathcal{D}_{\text{C}_3\text{H}_8,s} = 0.85\mathcal{D}_{\text{C}_3\text{H}_8,\text{Kn}}$ ; see the simulation results indicated by the continuous solid lines in Figure 11. The calculations of the surface diffusion model are in good agreement with the “mesopore diffusion” model, eq 3, in which the M-S diffusivities

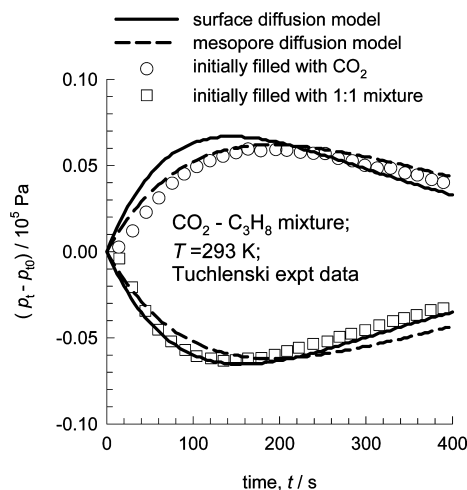


**Figure 11.** Experimental data of Tuchlenski et al.<sup>24</sup> for the dynamic pressure increase in the downstream compartment for CO<sub>2</sub>–C<sub>3</sub>H<sub>8</sub> mixtures at 293 K. Comparison of simulations with the mesopore diffusion (flux eq 7) with surface diffusion model (flux eq 14).

for hopping along the pore walls was taken as  $\mathcal{D}_{\text{CO}_2} = 0.55\mathcal{D}_{\text{CO}_2,\text{Kn}}$  and  $\mathcal{D}_{\text{C}_3\text{H}_8} = 0.8\mathcal{D}_{\text{C}_3\text{H}_8,\text{Kn}}$ . Remarkably, the use of the surface diffusion model also leads to the conclusion that the M-S surface diffusivities are lowered below the Knudsen prescription, by

approximately the same factors. The small differences in the values of the M-S surface diffusivities  $D_{i,s}$  with the corresponding values of mesopore diffusivities  $D_i$  arise because of the influence of mixture adsorption equilibrium.

Implicit in the results presented in Figure 11 is that the surface diffusion should not be viewed as an additional contribution to the fluxes as suggested by schematic in Figure 3;<sup>27</sup> there is no enhancement of fluxes of adsorbing gases above the values predicted by the DGM, eq 5.

## 6. CONCLUSIONS

The following conclusions may be drawn from our reinterpretation and reanalysis of the Tuchlenski, Yang, and Veldsink experiments. (1) For binary mixtures of poorly adsorbing gases, the transient pressure equilibration in the downstream compartment can be predicted with excellent accuracy by the DGM. The DGM model, neglecting surface diffusion, fails to provide good agreement with experimental data for mixtures for which one or both species have strong adsorption characteristics. (2) The Maxwell-Stefan (M-S) model, with adjusted values of the M-S diffusivities describing molecule-wall interactions,  $D_i$ , provides a reasonably good quantitative description of the transient pressure equilibration experiments with adsorbing gases. The adjusted values of the M-S diffusivities  $D_i$  are lower, by about 45–95%, than the corresponding values of the Knudsen diffusivities,  $D_{i,Kn}$ . The ratio  $D_i/D_{i,Kn}$  correlates reasonably with the Henry adsorption constant (cf. Figure 9). This lowering in the Knudsen diffusivity value for adsorbing gases is in line with the published MD simulation data. (3) The analysis of the data on macroporous membranes indicates that the ratio  $D_i/D_{i,Kn}$  is closer to unity. This suggests that the Knudsen prescription can be used for macropore diffusion as a reasonable approximation. (4) As compared to the DGM, the M-S formulation (eq 1) is more convenient for use to describe diffusion in mesoporous and macroporous materials because there is no need to separately account for surface diffusion effects. Indeed, our analysis of the transient CO<sub>2</sub>–C<sub>3</sub>H<sub>8</sub> mixture permeation indicates that surface diffusion should be not treated as an additional contribution as is suggested in the electrical analog schematic in Figure 3.

There are important consequences of the above set of conclusions for a variety of other applications in chemical engineering practice. For example, we may expect severe consequences for effectiveness factor calculations in mesoporous catalysts for which the DGM is almost invariably used;<sup>35</sup> this topic is currently being investigated.

## ■ ASSOCIATED CONTENT

### Supporting Information

The Supporting Information is available free of charge on the ACS Publications website at DOI: 10.1021/acs.iecr.6b00762.

Comparisons of the dusty gas and Maxwell–Stefan models for mesopore and macropore diffusion, details of the experiments for transient membrane permeation, and numerical procedures for solving the set of coupled differential equations. (PDF)

## ■ AUTHOR INFORMATION

### Corresponding Author

\*Tel.: +31 20 6270990. Fax: + 31 20 5255604. E-mail: r.krishna@contact.uva.nl.

### Notes

The authors declare no competing financial interest.

## ■ ABBREVIATIONS

- $A_{\text{membrane}}$  = cross-sectional area of membrane, m<sup>2</sup>
- $B_0$  = permeability of pore, m<sup>2</sup>
- $c_i$  = molar concentration of species  $i$ , mol m<sup>-3</sup>
- $c_{i,\text{sat}}$  = saturation capacity of species  $i$ , mol m<sup>-3</sup>
- $c_t$  = total molar concentration of mixture, mol m<sup>-3</sup>
- $d_p$  = diameter of pore, m
- $D_i$  = M-S diffusivity for molecule–wall interaction, m<sup>2</sup> s<sup>-1</sup>
- $D_{i,s}$  = M-S diffusivity for surface diffusion, m<sup>2</sup> s<sup>-1</sup>
- $D_{i,Kn}$  = Knudsen diffusivity of species  $i$ , m<sup>2</sup> s<sup>-1</sup>
- $D_{ij}$  = Maxwell-Stefan “bulk” diffusivity for  $i$ – $j$  pair, m<sup>2</sup> s<sup>-1</sup>
- $n$  = number of species in the mixture, dimensionless
- $N_i$  = molar flux of species  $i$ , mol m<sup>-2</sup> s<sup>-1</sup>
- $p_i$  = partial pressure of species  $i$  in mixture, Pa
- $p_t$  = total system pressure, Pa
- $R$  = gas constant, 8.314 J mol<sup>-1</sup> K<sup>-1</sup>
- $u_i$  = velocity of motion of species  $i$  with respect to pore wall, m s<sup>-1</sup>
- $V_{\text{compartment}}$  = volume of downstream compartment, m<sup>3</sup>
- $x_i$  = mole fraction of species  $i$  within pore, dimensionless
- $T$  = absolute temperature, K
- $z$  = distance coordinate, m

## Greek Letters

- $\delta$  = thickness of membrane, m
- $\Gamma_{ij}$  = thermodynamic factors, dimensionless
- $[\Gamma]$  = matrix of thermodynamic factors, dimensionless
- $\varepsilon$  = pore voidage, dimensionless
- $\mu_i$  = molar chemical potential of component  $i$ , J mol<sup>-1</sup>
- $\eta$  = viscosity of gas mixture, Pa s
- $\Pi_i$  = permeance of species  $i$  in mixture mol m<sup>-2</sup> s<sup>-1</sup> Pa<sup>-1</sup>
- $\mu_i$  = molar chemical potential of component  $i$ , J mol<sup>-1</sup>
- $\sigma$  = Lennard-Jones size parameter, m
- $\tau$  = tortuosity, dimensionless

## Subscripts

- $i$  = referring to component  $i$
- $t$  = referring to total mixture

## ■ REFERENCES

- (1) Chen, L.; Zhang, L.; Kang, Q.; Viswanathan, H. S.; Yao, J.; Tao, W. Nanoscale Simulation of Shale Transport Properties Using the Lattice Boltzmann Method: Permeability and Diffusivity. *Sci. Rep.* **2015**, *5*, 8089.
- (2) Wu, K.; Li, X.; Wang, C.; Yu, W.; Chen, Z. Model for Surface Diffusion of Adsorbed Gas in Nanopores of Shale Gas Reservoirs. *Ind. Eng. Chem. Res.* **2015**, *54*, 3225.
- (3) Krishna, R. Describing the Diffusion of Guest Molecules inside Porous Structures. *J. Phys. Chem. C* **2009**, *113*, 19756.
- (4) Krishna, R. Diffusion in Porous Crystalline Materials. *Chem. Soc. Rev.* **2012**, *41*, 3099.
- (5) Fuller, E. N.; Schettler, P. D.; Giddings, J. C. A New Method for Prediction of Binary Gas-phase Diffusion Coefficients. *Ind. Eng. Chem.* **1966**, *58*, 18.
- (6) Reid, R. C.; Prausnitz, J. M.; Poling, B. E. *The Properties of Gases and Liquids*, 4th ed.; McGraw-Hill: New York, 1986.
- (7) Bhatia, S. K.; Bonilla, M. R.; Nicholson, D. Molecular Transport in Nanopores: A Theoretical Perspective. *Phys. Chem. Chem. Phys.* **2011**, *13*, 15350.
- (8) Krishna, R.; van Baten, J. M. An Investigation of the Characteristics of Maxwell-Stefan Diffusivities of Binary Mixtures in Silica Nanopores. *Chem. Eng. Sci.* **2009**, *64*, 870.
- (9) Krishna, R.; van Baten, J. M. Unified Maxwell-Stefan Description of Binary Mixture Diffusion in Micro- and Meso- Porous Materials. *Chem. Eng. Sci.* **2009**, *64*, 3159.

- (10) Krishna, R.; van Baten, J. M. A Molecular Dynamics Investigation of the Unusual Concentration Dependencies of Fick Diffusivities in Silica Mesopores. *Microporous Mesoporous Mater.* **2011**, *138*, 228.
- (11) Krishna, R.; van Baten, J. M. Influence of Adsorption on the Diffusion Selectivity for Mixture Permeation across Mesoporous Membranes. *J. Membr. Sci.* **2011**, *369*, 545.
- (12) Krishna, R.; van Baten, J. M. Investigating the Validity of the Knudsen Prescription for Diffusivities in a Mesoporous Covalent Organic Framework. *Ind. Eng. Chem. Res.* **2011**, *50*, 7083.
- (13) Krishna, R.; van Baten, J. M. Investigating the Validity of the Bosanquet Formula for Estimation of Diffusivities in Mesopores. *Chem. Eng. Sci.* **2012**, *69*, 684.
- (14) Bhatia, S. K.; Nicholson, D. Comments on "Diffusion in a Mesoporous Silica Membrane: Validity of the Knudsen Diffusion Model". *Chem. Eng. Sci.* **2010**, *65*, 4519.
- (15) Bhatia, S. K.; Jepps, O.; Nicholson, D. Tractable Molecular Theory of Transport of Lennard-Jones Fluids in Nanopores. *J. Chem. Phys.* **2004**, *120*, 4472.
- (16) Bhatia, S. K.; Nicholson, D. Transport of Simple Fluids in Nanopores: Theory and Simulation. *AIChE J.* **2006**, *52*, 29.
- (17) Bhatia, S. K. Modeling Pure Gas Permeation in Nanoporous Materials and Membranes. *Langmuir* **2010**, *26*, 8373.
- (18) Bhatia, S. K.; Nicholson, D. Some Pitfalls in the Use of the Knudsen Equation in Modelling Diffusion in Nanoporous Materials. *Chem. Eng. Sci.* **2011**, *66*, 284.
- (19) Petropoulos, J. H.; Papadokostaki, K. G. May the Knudsen Equation be Legitimately, or at Least Usefully, Applied to Dilute Adsorbable Gas Flow in Mesoporous Media? *Chem. Eng. Sci.* **2012**, *68*, 392.
- (20) Ruthven, D. M.; DeSisto, W.; Higgins, S. Diffusion in a Mesoporous Silica Membrane: Validity of the Knudsen Diffusion Model. *Chem. Eng. Sci.* **2009**, *64*, 3201.
- (21) Ruthven, D. M. Letter to the Editor. Response to Comments from S.K. Bhatia and D. Nicholson. *Chem. Eng. Sci.* **2010**, *65*, 4521.
- (22) Reyes, S. C.; Sinfelt, J. H.; DeMartin, G. J.; Ernst, R. H.; Iglesia, E. Frequency Modulation Methods for Diffusion and Adsorption Measurements in Porous Solids. *J. Phys. Chem. B* **1997**, *101*, 614.
- (23) Higgins, S.; DeSisto, W.; Ruthven, D. M. Diffusive Transport through Mesoporous Silica Membranes. *Microporous Mesoporous Mater.* **2009**, *117*, 268.
- (24) Tuchlenski, A.; Uchytel, P.; Seidel-Morgenstern, A. An Experimental Study of Combined Gas Phase and Surface Diffusion in Porous Glass. *J. Membr. Sci.* **1998**, *140*, 165.
- (25) Yang, J.; Čermáková, J.; Uchytel, P.; Hamel, C.; Seidel-Morgenstern, A. Gas Phase Transport, Adsorption and Surface Diffusion in a Porous Glass Membrane. *Catal. Today* **2005**, *104*, 344.
- (26) Veldsink, J. W.; Versteeg, G. F.; Van Swaaij, W. P. M. An Experimental Study of Diffusion and Convection of Multicomponent Gases through Catalytic and Non-Catalytic Membranes. *J. Membr. Sci.* **1994**, *92*, 275.
- (27) Mason, E. A.; Malinauskas, A. P. *Gas Transport in Porous Media: The Dusty-Gas Model*; Elsevier: Amsterdam, 1983.
- (28) Young, J. B.; Todd, B. Modelling of Multi-Component Gas Flows in Capillaries and Porous Solids. *Int. J. Heat Mass Transfer* **2005**, *48*, 5338.
- (29) Kerkhof, P. J. A. M. A Modified Maxwell-Stefan Model for Transport Through Inert Membranes: The Binary Friction Model. *Chem. Eng. J.* **1996**, *64*, 319.
- (30) Krishna, R.; Wesselingh, J. A. The Maxwell-Stefan Approach to Mass Transfer. *Chem. Eng. Sci.* **1997**, *52*, 861.
- (31) Argönül, A.; Keil, F. J. An Alternative Procedure for Modeling of Knudsen Flow and Surface Diffusion. *Period. Polytech., Chem. Eng.* **2008**, *52*, 37.
- (32) Gruener, S.; Huber, P. Knudsen Diffusion in Dilicon Nanochannels. *Phys. Rev. Lett.* **2008**, *100*, 064502.
- (33) Petukhov, D. I.; Eliseev, A. A. Gas Permeation Through Nanoporous Membranes in the Transitional Flow Region. *Nanotechnology* **2016**, *27*, 085707.
- (34) Krishna, R.; Baur, R. Modelling Issues in Zeolite Based Separation Processes. *Sep. Purif. Technol.* **2003**, *33*, 213.
- (35) Jackson, R. *Transport in Porous Catalysts*; Elsevier: Amsterdam, 1977.
- (36) Talu, O.; Myers, A. L. Reference Potentials for Adsorption of Helium, Argon, Methane and Krypton in High-Silica Zeolites. *Colloids Surf., A* **2001**, *187–188*, 83.

*Supplementary Information (SI)*

# Investigating the Validity of the Knudsen Diffusivity Prescription for Mesoporous and Macroporous Materials

**Rajamani Krishna**

Van 't Hoff Institute for Molecular Sciences, University of Amsterdam, Science Park 904,

1098 XH Amsterdam, The Netherlands

\*CORRESPONDING AUTHOR Tel +31 20 6270990; Fax: + 31 20 5255604;

email: [r.krishna@contact.uva.nl](mailto:r.krishna@contact.uva.nl)

## Table of Contents

1. Preamble.....	3
2. The Dusty Gas Model for mixture diffusion.....	3
3. The linearized solution to the DGM.....	7
4. The Dusty Gas Model (DGM) for unary diffusion .....	8
5. The Maxwell-Stefan model for mesopore diffusion .....	9
6. The linearized solution to the M-S diffusion equations .....	13
7. Description of Tuchlenski, Yang, and Veldsink experiments.....	16
8. Simulations of transient experiments with poorly adsorbing gases .....	19
9. Transient overshoots/undershoots for mixture uptake within adsorbent particles.....	21
10. Simulations of Tuchlenski experiments with adsorbing gases .....	23
11. Simulations of Yang experiments with adsorbing gases .....	26
12. Ratio of M-S diffusivity to Knudsen diffusivity plotted as a function of Henry coefficient for adsorption .....	28
13. Simulations of Veldsink experiments with adsorbing gases .....	28
14. Comparison of Tuchlenski CO <sub>2</sub> /C <sub>3</sub> H <sub>8</sub> experiments with surface diffusion model.....	29
15. Comparison of Yang CO <sub>2</sub> /C <sub>3</sub> H <sub>8</sub> experiments with surface diffusion model.....	31
16. Notation .....	33
17. References .....	40
18. Caption for Figures.....	42

## 1. Preamble

This Supporting Information (SI) accompanying the article *Investigating the Validity of the Knudsen Diffusivity Prescription for Mesoporous and Macroporous Materials* provides (a) detailed comparisons of the Dusty Gas, and the Maxwell-Stefan models for mesopore and macropore diffusion, (b) details of the Veldsink, Tuchlenski, and Yang experiments for transient mixture permeations, (c) details of the numerical solutions to the equations describing transient mixture diffusion across membranes, (d) input data on the parameters used to model Tuchlenski, Yang and, and Veldsink experiments, and (e) detailed comparisons of experimental data with model simulations.

For ease of reading, this Supplementary Material is written as a stand-alone document; as a consequence, there is some overlap of material with the main manuscript.

## 2. The Dusty Gas Model for mixture diffusion

For  $n$ -component diffusion in a cylindrical pore, the DGM flux relations are commonly written as<sup>1</sup>

$$-\varepsilon \frac{p_i}{RT} \frac{\partial x_i}{\partial z} - \varepsilon \left( \frac{x_i}{RT} \right) \left( \frac{B_0 p_i}{\eta D_{i,Kn}} + 1 \right) \frac{\partial p_i}{\partial z} = \sum_{\substack{j=1 \\ j \neq i}}^n \left( \frac{x_j N_j - x_i N_i}{D_{ij}} \right) + \frac{N_i}{D_{i,Kn}}; \quad i = 1, 2, \dots, n \quad (1)$$

The fluxes  $N_i$  are defined as the moles transported per  $m^2$  of total external surface area of the porous material

$$N_i \equiv \varepsilon \frac{p_i}{RT} u_i; \quad i = 1, 2, \dots, n \quad (2)$$

The species velocities  $u_i$  are defined in a reference framework with respect to the pore walls. The porosity  $\varepsilon$  appears on the left member of equation (2) because only a fraction  $\varepsilon$  of the external surface is available for influx of guest molecules.

Equation (1) combines the contributions to the fluxes  $N_i$  arising from (a) molecule-wall collisions, reflected in the Knudsen diffusivity,  $D_{i,Kn}$ , (b) molecule-molecule collisions, reflected in the bulk gas

phase diffusivity,  $D_{ij}$ , and (c) viscous flow with the permeability coefficient  $B_0$ ; see schematic in Figure 1 that is adapted from Mason and Malinauskas.<sup>1</sup>

The bulk gas phase diffusivities  $D_{ij}$  for a *binary* mixture of species  $i$  and species  $j$  can be estimated using the kinetic theory of gases or from empirical procedures such as the Fuller-Schettler-Giddings method.<sup>2, 3</sup> These values are the same for the  $i - j$  combination in an  $n$ -component mixture. For ideal gas mixtures, the bulk gas phase diffusivities are inversely proportional to the pressure.

For a cylindrical pore of diameter  $d_p$ , the permeability  $B_0$  is

$$B_0 = \frac{d_p^2}{32} \quad (3)$$

The Knudsen prescription is

$$D_{i,Kn} = \frac{d_p}{3} \sqrt{\frac{8RT}{\pi M_i}} \quad (4)$$

The formula (4), that was first put forward by Knudsen<sup>4</sup> and subsequently refined by Smoluchowski,<sup>5</sup> needs further elucidation. Equation (4) is based on the assumption that the reflections of a molecule after collision with the pore wall are purely *diffuse* in nature, i.e. the angle of reflection bears no relation to the angle of incidence at which the molecule strikes the pore wall.

In order to get an appreciation of the relative importance of molecule-wall and molecule-molecule interactions, Figure 2a presents a comparison Knudsen ( $D_{He,Kn}$ ,  $D_{Ar,Kn}$ ), and bulk diffusivities ( $D_{He,Ar}$ ) of He/Ar mixtures at 293 K in cylindrical mesopores and macropores. The calculations of the bulk diffusivities  $D_{He,Ar}$  are at total pressures of 0.1 MPa. These results show that, generally speaking, diffusion in mesopores is dominated by molecule-wall collisions.

Increasing the system pressure, lowers the bulk diffusivities and therefore molecule-molecule collisions become of increasing importance for high pressure operations. Figure 2b compares the Knudsen ( $D_{He,Kn}$ ,  $D_{Ar,Kn}$ ), and bulk diffusivities ( $D_{He,Ar}$ ) of He/Ar mixtures at 293 K for a mesopore of

10 nm, at varying system pressures. At pressures above 2 MPa, the molecule-molecule collisions become comparable in importance as molecule-wall collisions.

For non-cylindrical pores, with tortuosity  $\tau$ , the DGM are re-written in the form

$$-\frac{p_t}{RT} \frac{\partial x_i}{\partial z} - \left( \frac{x_i}{RT} \right) \left( \frac{B_0 p_t}{\eta D_{i,Kn}} + 1 \right) \frac{\partial p_t}{\partial z} = \sum_{j=1, j \neq i}^n \left( \frac{x_j N_i - x_i N_j}{(\varepsilon/\tau) D_{ij}} \right) + \frac{N_i}{(\varepsilon/\tau) D_{i,Kn}}; \quad i = 1, 2 \dots n \quad (5)$$

It is common practice to define “effective” coefficients

$$D_{i,Kn}^e = (\varepsilon/\tau) D_{i,Kn}; \quad D_{ij}^e = (\varepsilon/\tau) D_{ij}; \quad B_0^e = (\varepsilon/\tau) d_p^2/32; \quad B_0^e/D_{i,Kn}^e \equiv B_0/D_{i,Kn} \quad (6)$$

and re-write equation (5) as

$$-\frac{p_t}{RT} \frac{\partial x_i}{\partial z} - \left( \frac{x_i}{RT} \right) \left( \frac{B_0 p_t}{\eta D_{i,Kn}} + 1 \right) \frac{\partial p_t}{\partial z} = \sum_{j=1, j \neq i}^n \left( \frac{x_j N_i - x_i N_j}{D_{ij}^e} \right) + \frac{N_i}{D_{i,Kn}^e}; \quad i = 1, 2 \dots n \quad (7)$$

For a cylindrical pore, the tortuosity  $\tau=1$  and equation (7) reduces to equation (1).

Summing equation (7) over all the  $n$ -species we obtain

$$-\frac{1}{RT} \left( 1 + \frac{B_0 p_t}{\eta} \sum_{i=1}^n \frac{x_i}{D_{i,Kn}} \right) \frac{\partial p_t}{\partial z} = \sum_{i=1}^n \frac{N_i}{D_{i,Kn}^e} \quad (8)$$

The term  $\frac{B_0 p_t}{\eta} \sum_{i=1}^n \frac{x_i}{D_{i,Kn}}$  indicates the fractional contribution of viscous flow to the changes in the

total pressure.

For the DGM model, we define the square matrix  $[B]$

$$[B] = \begin{bmatrix} \frac{1}{D_{1,Kn}^e} + \frac{x_2}{D_{12}^e} & -\frac{x_1}{D_{12}^e} \\ -\frac{x_2}{D_{12}^e} & \frac{1}{D_{2,Kn}^e} + \frac{x_1}{D_{12}^e} \end{bmatrix}; \quad \text{DGM model} \quad (9)$$

Equation (7) can be re-cast into 2-dimensional matrix notation for explicit evaluation of the fluxes



$$\begin{pmatrix} N_1 \\ N_2 \end{pmatrix} = -\frac{1}{RT} [B]^{-1} \begin{pmatrix} \frac{\partial p_1}{\partial z} + x_1 \left( \frac{B_0 p_t}{\eta D_{1,Kn}} + 1 \right) \frac{\partial p_t}{\partial z} \\ \frac{\partial p_2}{\partial z} + x_2 \left( \frac{B_0 p_t}{\eta D_{2,Kn}} + 1 \right) \frac{\partial p_t}{\partial z} \end{pmatrix}; \quad \text{DGM model} \quad (10)$$

For mixtures of non-adsorbing gases such as He-Ar, the DGM equations (7) are in good agreement with experimental data.<sup>1,6</sup>

In practice, the guest molecules have finite adsorption on the pore walls. In the DGM model concept as put forward by Mason and Malinauskas,<sup>1</sup> the motion of adsorbed molecules along the surface of the pore walls needs to be accounted for as an additional, parallel, contribution; see schematic in Figure 1. The surface diffusion contribution is appropriately described in the Maxwell-Stefan (M-S) formulation<sup>7</sup>,

$$N_{i,surface} = -D_{i,s} \frac{c_i}{RT} \frac{d\mu_i}{dz}; \quad i = 1, 2, \dots, n \quad (11)$$

In equation (11),  $c_i$  is the molar concentration of species  $i$  in the *adsorbed* phase expressed in terms of moles per m<sup>3</sup> of the accessible pore volume,  $\mu_i$  is the chemical potential of species  $i$  in the adsorbed phase, and  $D_{i,s}$  is the M-S surface diffusivity of species  $i$ . It is convenient to re-write Equation (11) in terms of the gradients in the molar concentrations of the components in the adsorbed phase. Towards this end, we define a matrix of thermodynamic factors  $\Gamma_{ij}$

$$\frac{c_i}{RT} \frac{\partial \mu_i}{\partial z} = \sum_{j=1}^n \Gamma_{ij} \frac{\partial c_j}{\partial z}; \quad \Gamma_{ij} = \frac{c_i}{p_i} \frac{\partial p_i}{\partial c_j}; \quad i, j = 1, 2, \dots, n \quad (12)$$

and so

$$N_{i,surface} = -D_{i,s} \sum_{j=1}^n \Gamma_{ij} \frac{dc_j}{dz}; \quad i = 1, 2, \dots, n \quad (13)$$

Most commonly, the surface diffusivity decreases with surface coverage

$$D_{i,s} = D_{i,s}(0)(1 - \theta_1 - \theta_2 - \dots - \theta_n) \quad (14)$$

Since there are no predictive methods for estimation of the surface diffusivities in equation (11), experimental data are required.

The work of Tuchlenski et al.<sup>9</sup> provides an excellent account of how the DGM equation (7) can be combined with the M-S equation (11) for surface diffusion<sup>7, 8</sup> in order to model transient mixture permeation across a Vycor glass mesoporous membrane of average pore diameter  $d_p \approx 4$  nm. The surface diffusivities are fitted to match the experimental data on membrane permeation.

Wu et al.<sup>10</sup> develop a model to combine surface diffusion in shale reservoirs with the other flux contributions.

The DGM model formulation has been subject to criticism in the recent literature due to some inconsistencies in handling the viscous flow contribution.<sup>11, 12</sup>

### 3. The linearized solution to the DGM

For explicit calculations of the transfer fluxes, a linearization technique has been suggested by Krishna.<sup>13</sup> as explained below. The “linearization” procedure essentially involves the assumption that the matrix  $[B]$ , defined in equation (9) for DGM, can be considered to be constant during the discretized time interval, provided it is evaluated at the average compositions  $\bar{x}_1$  and  $\bar{x}_2$  within the capillary membrane, of thickness  $\delta$ .

The linearized DGM model yields

$$\begin{pmatrix} N_1 \\ N_2 \end{pmatrix} = \frac{1}{RT\delta} [B]^{-1} \begin{pmatrix} (p_{10} - p_{1\delta}) + \bar{x}_1 \left( \frac{B_0 p_t}{\eta D_{1,Kn}} + 1 \right) (p_{t0} - p_{t\delta}) \\ (p_{20} - p_{2\delta}) + \bar{x}_2 \left( \frac{B_0 p_t}{\eta D_{2,Kn}} + 1 \right) (p_{t0} - p_{t\delta}) \end{pmatrix} \quad (15)$$

This linearized procedure is used in all of the model calculations presented in this article. In order to verify the validity of the linearized procedure, we shall compare the calculations using equation (15) with the experimental data of Remick and Geankoplis.<sup>14</sup>

Remick and Geankoplis<sup>14</sup> have measured the fluxes of helium (1), neon (2) and argon (3) across a porous capillary diffusion cell made up of cylindrical capillaries of diameter  $d_p = 39.1$   $\mu\text{m}$ , and length  $\delta$

= 9.6 mm. The experiments were performed in such a way that the pressure drop across the capillary diffusion cell was zero, so that there was no viscous flow. The average system pressure,  $p_{av}$ , was varied and so were partial pressure driving forces,  $p_{i0} - p_{i\delta}$ ; the data are tabulated in Table 1 of their paper.

Figure 3a presents a comparison of the experimental data (shown by symbols) of Remick and Geankoplis<sup>14</sup> for the fluxes of helium (1), neon (2) and argon (3) with the calculations using the linearized equation (15). There is very good agreement between the calculated fluxes and experimental data over the wide range of system pressures. With increasing pressure, the bulk gas phase diffusivities,  $D_{ij}$ , are reduced and molecule-molecule collisions become increasingly important. Conversely, molecule-wall collisions are important at lower pressures. The DGM correctly predicts the transition between Knudsen controlled and bulk diffusion controlled regimes. In the Knudsen regime, the transfer fluxes linearly proportional to the system pressure. In bulk diffusion regime, the transfer fluxes are independent of pressure.

Figure 3b presents calculations of the fluxes as a function of the capillary diameter,  $d_p$ , maintaining the total pressure =  $10^3$  Pa. Three regimes can again be distinguished. In the Knudsen regime, the flux is proportional to the capillary diameter,  $d_p$ . In the bulk diffusion regime, the flux is independent of the pore diameter.

#### 4. The Dusty Gas Model (DGM) for unary diffusion

For unary diffusion, the total contributions of Knudsen diffusion, surface diffusion, and viscous flow are

$$N_i = -\frac{1}{RT} \left( \frac{B_0 p_i}{\eta_i D_{i,Kn}} + 1 \right) D_{i,Kn}^e \frac{dp_i}{dz} - D_{i,s} \frac{c_i}{RT} \frac{d\mu_i}{dz} \quad (16)$$

The chemical potential gradients can be related to the gradients of the molar concentrations in the adsorbed phase by introducing the thermodynamic factor  $\Gamma_i$

$$\frac{c_i}{RT} \frac{d\mu_i}{dz} = \Gamma_i \frac{dc_i}{dz}; \quad \Gamma \equiv \frac{c_i}{p_i} \frac{\partial p_i}{\partial c_i} \quad (17)$$

For mono-layer Langmuir adsorption,

$$\theta_i = \frac{c_i}{c_{i,sat}} = \frac{b_i p_i}{1 + b_i p_i}; \quad \Gamma_i = (1 + b_i p_i) = \frac{1}{1 - \theta_i} \quad (18)$$

where  $\theta_i$  is the fractional surface coverage. The fractional vacancy,  $\theta_v$ , is

$$\theta_v = 1 - \theta_i = \frac{1}{1 + b_i p_i} \quad (19)$$

Differentiating the Langmuir Equation (18), we can write

$$\frac{dc_i}{dz} = \frac{c_{i,sat} b_i}{(1 + b_i p_i)^2} \frac{dp_i}{dz} \quad (20)$$

Combining Equations (14), (16), (18), and (20) we obtain

$$N_i = -\frac{1}{RT} \left( \frac{B_0 p_i}{\eta_i D_{i,Kn}} + 1 \right) D_{i,Kn}^e \frac{dp_i}{dz} - D_{i,s}(0) \frac{c_{i,sat} b_i}{(1 + b_i p_i)} \frac{dp_i}{dz} \quad (21)$$

We shall illustrate the use of equation (21) to calculate the fluxes. Figure 4 shows the unary CO<sub>2</sub> permeation fluxes across Vycor glass membrane at (a) 293 K, and (b) 343 K as a function of upstream pressure (keeping the downstream pressure constant at 101 kPa). Also shown in Figure 4 are the calculations neglecting the contribution of the second member on the right hand side of the equality. Figure 4 shows that the DGM concept anticipates a slight enhancement of the flux due to surface diffusion.

## 5. The Maxwell-Stefan model for mesopore diffusion

In recent works, a different approach to the description of diffusion in porous materials has been developed, using the Maxwell-Stefan approach,<sup>15-19</sup> employing chemical potential gradients as driving forces:

$$-\rho V_p \frac{c_i}{RT} \frac{\partial \mu_i}{\partial z} = \sum_{\substack{j=1 \\ j \neq i}}^n \left( \frac{x_j N_i - x_i N_j}{D_{ij}} \right) + \frac{N_i}{D_i}; \quad i = 1, 2, \dots, n \quad (22)$$

In equation (22),  $c_i$  is the molar concentration of species  $i$  based on the accessible pore volume,  $V_p$  ( $= \text{m}^3 \text{ pore volume per kg framework}$ ), and  $\rho$  is the material framework density. The quantity  $\rho V_p$  is the fractional pore volume

$$\rho V_p = \left( \frac{\text{kg framework}}{\text{m}^3 \text{ framework}} \right) \left( \frac{\text{m}^3 \text{ pore volume}}{\text{kg framework}} \right) = \left( \frac{\text{m}^3 \text{ pore volume}}{\text{m}^3 \text{ framework}} \right) = \varepsilon \quad (23)$$

Equation (22) applies to microporous, mesoporous, and macroporous materials. For mesoporous, and macroporous materials with the fluid phase in the gaseous state,  $c_i = \frac{p_i}{RT}$ ;  $\frac{\partial \mu_i}{\partial z} = \frac{RT}{p_i} \frac{\partial p_i}{\partial z}$ , the left hand side of equaton (22) simplifies to yield

$$-\varepsilon \frac{1}{RT} \frac{\partial p_i}{\partial z} = \sum_{\substack{j=1 \\ j \neq i}}^n \left( \frac{x_j N_i - x_i N_j}{D_{ij}} \right) + \frac{N_i}{D_i}; \quad i = 1, 2, \dots, n \quad (24)$$

For pores with tortuosity  $\tau$ , equation (24) may be modified as follows

$$-\frac{1}{RT} \frac{\partial p_i}{\partial z} = \sum_{\substack{j=1 \\ j \neq i}}^n \left( \frac{x_j N_i - x_i N_j}{(\varepsilon/\tau) D_{ij}} \right) + \frac{N_i}{(\varepsilon/\tau) D_i}; \quad i = 1, 2, \dots, n \quad (25)$$

and is comparable, but not equivalent with the corresponding DGM equation (5). In the M-S formulation (25), the M-S diffusivity  $D_i$  describes the interaction between species  $i$  and the pore wall. The Maxwell-Stefan diffusion formulation is essentially a “friction formulation”; the M-S diffusivity  $D_i$ , is to be interpreted as an inverse drag coefficient between the guest molecule and the surface of the framework material; this diffusivity reflects both the Knudsen and surface diffusion characteristics. In other words, the surface diffusion is not separately accounted for. Furthermore, any viscous flow contribution is also subsumed into the M-S diffusivities  $D_i$ , and  $D_{ij}$ . Comparing equation (25) with the DGM equation (1) we may derive; see Krishna and Wesselingh<sup>20</sup>

$$D_i = D_{i,Kn} \left( 1 + \frac{B_0 p_t}{\eta} \sum_{j=1}^n \frac{x_j}{D_{j,Kn}} \right); \quad i = 1, 2, \dots, n \quad (26)$$

For explicit evaluation of the fluxes, it is convenient to define a square matrix

$$[B] = \begin{bmatrix} \frac{1}{D_1(\varepsilon/\tau)} + \frac{x_2}{D_{12}(\varepsilon/\tau)} & -\frac{x_1}{D_{12}(\varepsilon/\tau)} \\ -\frac{x_2}{D_{12}(\varepsilon/\tau)} & \frac{1}{D_2(\varepsilon/\tau)} + \frac{x_1}{D_{12}(\varepsilon/\tau)} \end{bmatrix}; \quad \text{M-S model} \quad (27)$$

Equation (25) may be re-written to enable explicit calculation of the fluxes

$$\begin{pmatrix} N_1 \\ N_2 \end{pmatrix} = -\frac{1}{RT} [B]^{-1} \begin{pmatrix} \frac{\partial p_1}{\partial z} \\ \frac{\partial p_2}{\partial z} \end{pmatrix}; \quad \text{M-S model} \quad (28)$$

Figure 5a presents MD data on Maxwell-Stefan diffusivity  $D_{12}$ , for equimolar ( $c_1 = c_2$ ) binary mixture of CH<sub>4</sub>-Ar in silica pores with diameters in the range 2 nm to 10 nm. Also shown (square symbols) are the  $D_{12,\text{fl}}$  data for binary fluid CH<sub>4</sub>-Ar mixture diffusion, obtained from independent MD simulations. The molecule-molecule interactions are independent of the pore diameter, and equal the corresponding values of the fluid phase diffusivity. The straight line represents the estimations of the gas phase diffusivity  $D_{12,\text{fl}}$  using the Fuller-Schettler-Giddings method.<sup>2,3</sup> The results of Figure 5a indicate that the FSG method can be used to estimate the M-S diffusivity  $D_{12}$  in cylindrical mesopores.

Figure 5b, c, d, e present MD data on the Maxwell-Stefan diffusivity  $D_{12}$ , for equimolar ( $c_1 = c_2$ ) binary mixtures CO<sub>2</sub>- CH<sub>4</sub>, CH<sub>4</sub>- H<sub>2</sub>, CO<sub>2</sub>- H<sub>2</sub>, and Ar- H<sub>2</sub> in BTP-COF, a covalent organic framework with 3.4 nm hexagonal channels. The values are comparable in magnitude with corresponding values of the  $D_{12,\text{fl}}$  data for binary fluid mixture diffusion, obtained from independent MD simulations.

Extensive data set of MD simulations for mesoporous channels show that the M-S diffusivity  $D_i$  equals the Knudsen diffusivity value given by equation (4) for gases such as H<sub>2</sub> that have poor adsorption strength.<sup>15-19, 21-23</sup> For gaseous molecules that have finite adsorption on the pore walls, the M-S diffusivity  $D_i$  is significantly lower than the value predicted by equation (4). The reasons for this departure must be attributed to the failure of the Knudsen formula for molecules with strong adsorption strength; this failure has been highlighted in several recent publications.<sup>15-19, 21-23</sup> Adsorption causes the

molecules to bind to the wall, and perhaps hop to a neighboring adsorption site, rather than return to the bulk after collision; this introduces a *bias* in the molecular hops. This bias increases with increasing adsorption strength, causing a violation of the diffuse reflectance assumption that is invoked in deriving equation (4).<sup>17, 21, 22</sup> It has been demonstrated that the departures from the Knudsen formula correlates with the binding energy for adsorption of the molecules at the pore walls.<sup>23</sup>

As illustration, Figure 6a presents MD data<sup>23, 24</sup> on the M-S diffusivity  $D_i$  for various guest molecules (hydrogen, argon, carbon dioxide, methane, ethane, propane) in BTP-COF, that has 3.4 nm hexagonal channels, plotted as function of the pore concentration,  $c_i$ . The M-S diffusivities show a slight increase with increasing pore concentration. In the limit of zero-pore concentration, we denote the value of the diffusivity as  $D_i(0)$ . Figure 6b presents the values of  $D_i(0)/D_{i,Kn}$  for BTP-COF, where the Knudsen diffusivity is estimated using equation (4). The  $D_i(0)/D_{i,Kn}$  values range from approximately unity for H<sub>2</sub> to a value of 0.1 for n-hexane (nC6). Furthermore,  $D_i(0)/D_{i,Kn}$  is seen to correlate very well with the Henry coefficient for adsorption. This is a rational result. The higher the binding energy, the higher is the sticking tendency of that species with the pore wall, leading to greater departure from the Knudsen prescription of diffuse reflectance.

Figure 6c presents a plot of the  $D_i(0)/D_{i,Kn}$  for linear alkanes as a function of carbon number in BTP-COF, 2 nm cylindrical silica pore, and 3 nm cylindrical pore. In all these mesoporous structures, the decrease in  $D_i(0)/D_{i,Kn}$  with increasing carbon number is due to increased adsorption strength.

Figure 7 shows MD data of M-S diffusivity at zero-loading,  $D_i$ , of (a) CH<sub>4</sub>, (b) Ar, (c) CO<sub>2</sub>, and (c) C<sub>3</sub>H<sub>8</sub> in zeolites, MOFs, and silica mesopores, plotted as a function of the pore dimension. The data has been culled from various MD simulation data sources.<sup>15-17</sup> We note that the MD data fall consistently below the values prescribed by the Knudsen formula. The guest molecules CO<sub>2</sub>, and C<sub>3</sub>H<sub>8</sub> are strongly adsorbed on the silica pore walls, and the M-S diffusivity is significantly lower than then Knudsen diffusivity value.

## 6. The linearized solution to the M-S diffusion equations

Before analyzing the experimental data on meso- and macro-porous membranes, let us gain some insights into the relative importance of molecule-wall, molecule-molecule interactions in meso- and macro-porous materials.

For this purpose we analyze, and model, the two-bulb diffusion experiments of Duncan and Toor<sup>25</sup> with ternary H<sub>2</sub>(1)/N<sub>2</sub>(2)/CO<sub>2</sub>(3) gas mixtures. The experimental set-up consisted of a two bulb diffusion cells, pictured in Figure 8. The two bulbs were connected by means of capillary tube of length  $\delta = 86$  mm, with a diameter,  $d_p = 2.08$  mm. The total system pressures in either bulb at the start of the experiment is  $p_{t0,A} = p_{t0,B} = 10^5$  Pa. At time  $t = 0$ , the stopcock separating the two composition environments at the center of the capillary was opened and diffusion of the three species was allowed to take place.

The initial compositions (mole fractions in the two bulbs, Bulb A and Bulb B), are

$$\begin{aligned} \text{Bulb A : } & x_{10,A} = 0.00000; x_{20,A} = 0.50086; x_{30,A} = 0.49914 \\ \text{Bulb B : } & x_{10,B} = 0.50121; x_{20,B} = 0.49879; x_{30,B} = 0.00000 \end{aligned} \quad (29)$$

The initial partial pressures in the two bulbs are

$$\begin{aligned} \text{Bulb A : } & p_{t0,A} = x_{i0,A} P_{t0,A} \\ \text{Bulb B : } & p_{t0,B} = x_{i0,B} P_{t0,B} \end{aligned} \quad (30)$$

The final equilibrated partial pressures will be equal in both bulbs

$$p_{t,eq} = \frac{p_{t0,A} + p_{t0,B}}{2} \quad (31)$$

The composition trajectories for each of the three diffusing species in either bulb has been presented in Figure 9. We note that despite the fact that the driving force for nitrogen is practically zero, it does transfer from one bulb to the other, exhibiting over-shoot and under-shoot phenomena when approaching equilibrium. The transient equilibration trajectories of H<sub>2</sub>, and CO<sub>2</sub> are “normal”, with their compositions in the two bulbs approaching equilibrium in a monotonous manner.



Let us now model the experiments. The flux relations are given by the Maxwell-Stefan equations

(24):

$$\begin{aligned}
 -\frac{1}{RT} \frac{dp_1}{dz} &= \frac{x_2 N_1 - x_1 N_2}{D_{12}} + \frac{x_3 N_1 - x_1 N_3}{D_{13}} + \frac{1}{D_1}; \\
 -\frac{1}{RT} \frac{dp_2}{dz} &= \frac{x_1 N_2 - x_2 N_1}{D_{12}} + \frac{x_3 N_2 - x_2 N_3}{D_{23}} + \frac{1}{D_2}; \\
 -\frac{1}{RT} \frac{dp_3}{dz} &= \frac{x_1 N_3 - x_3 N_1}{D_{13}} + \frac{x_2 N_3 - x_3 N_2}{D_{23}} + \frac{1}{D_3}
 \end{aligned} \tag{32}$$

We have omitted the porosity  $\varepsilon$ , because the  $N_i$  in equation (32) are defined in terms of the cross-sectional area of the cylindrical pore.

The M-S diffusivities for the three binary pairs at  $T = 308.3$  K are (see Krishna<sup>26</sup> for further details)

$$\begin{aligned}
 D_{12} &= 8.33 \times 10^{-5} \text{ m}^2 \text{ s}^{-1} \\
 D_{13} &= 6.8 \times 10^{-5} \text{ m}^2 \text{ s}^{-1} \\
 D_{23} &= 1.68 \times 10^{-5} \text{ m}^2 \text{ s}^{-1}
 \end{aligned} \tag{33}$$

The adsorption on the pore walls of the capillary tube are considered to be of negligible importance, and the Knudsen formula (4) is applied to calculate the M-S diffusivities  $D_i$ . In our simulations we ignore viscous flow contributions.

The transient partial pressures in Bulb A are given by

$$V_{Bulb} \frac{1}{RT} \frac{\partial p_{i,A}(t)}{\partial t} = -A_{pore} N_i \tag{34}$$

In equation (34), the flux is considered positive if directed from Bulb A to Bulb B. If we apply the linearization approach of Krishna,<sup>13</sup> and assume the matrix  $[B]$  (defined by equation (27), appropriately generalized), evaluated at the final equilibrated compositions, the set of equations (32) and (34) can be solved analytically to yield the 3-dimensional matrix differential equation describing the partial pressure transience in Bulb A, and Bulb B

$$\begin{aligned} (p_A(t) - p_{eq}) &= \exp\left(-\frac{A_{pore}}{V_{Bulb}\delta} [B]^{-1} t\right) (p_{0,A} - p_{eq}) \\ (p_B(t) - p_{eq}) &= (p_{eq} - p_A(t)) \end{aligned} \quad (35)$$

For pore diameters,  $d_p$  larger than about 2  $\mu\text{m}$ , the molecule-wall collisions are of negligible importance, and the diffusion is in the “bulk diffusion controlled regime”. In this case, the simulation results in Figure 9 (shown by the continuous solid lines (for Bulb A) and dashed lines (for Bulb B)) are in excellent quantitative agreement with the experimental data of Duncan and Toor.<sup>25</sup> The overshoot experienced by nitrogen signifies uphill diffusion, as explained in considerable detail in earlier work.<sup>26</sup> The overshoots and undershoots experienced by nitrogen emanate from the differences in the binary pair M-S diffusivities of the constituent binary pairs  $D_{12}, D_{13}, D_{23}$ ; see the values in equation (33).

Having established the accuracy of the M-S model to describe the transient diffusion for capillary diameters  $d_p > 2 \mu\text{m}$ , we proceed to examine two other scenarios:  $d_p = 200 \text{ nm}$  (macropore), and  $d_p = 2 \text{ nm}$  (mesopore); the simulation results are presented in Figure 10, and Figure 11.

For both these cases, the molecule-wall collisions are important. The inclusions of molecule-wall interactions leads to differences in the total pressures,  $p_{t,A}$ , and  $p_{t,B}$ , in the two bulbs; see Figure 10b, and Figure 11b. These pressure overshoots are precisely analogous to those experienced in the Tuchlenski, Yang, and Veldsink membrane permeation experiments. The pressure overshoot is stronger for the mesopore capillary,  $d_p = 2 \text{ nm}$  than for the macropore capillary  $d_p = 200 \text{ nm}$ .

There is however, an important difference in the transient partial pressure equilibrations. For the  $d_p = 200 \text{ nm}$  macropore, the overshoot and undershoot in the nitrogen partial pressures persists even with the inclusion of molecule-wall collisions; see Figure 10a. This implies that uphill diffusion phenomena can be experienced for mesopores; uphill diffusion arises because of the differences in the binary pair M-S diffusivities of the constituent binary pairs  $D_{12}, D_{13}, D_{23}$ .

For mesopore capillary,  $d_p = 2 \text{ nm}$ , molecule-wall collisions are dominant and the contribution of molecule-molecule collisions is negligible. Therefore, no overshoots or undershoots are experienced by nitrogen during transient equilibration.

It is also interesting to examine the partial pressure profiles along the capillary tube at any instant of time,  $t$ . The analytic solution to the partial profiles as a function of distance,  $z$ , when two semi-infinite slabs are brought into contact with each other are given by (see the Supporting Information accompany the paper by Krishna<sup>26</sup>)

$$(p(z, t)) = \frac{1}{2}(p_L + p_R) + \frac{1}{2} \operatorname{erf} \left[ -\frac{z}{\sqrt{4[B]^{-1}t}} \right] (p_R - p_L) \quad (36)$$

The position  $z = 0$  is mid-way between the two ends of the capillary.

Figure 12 shows the component partial pressure profiles, along the distance of the 200 nm capillary tube. These profiles are for time,  $t = 10$  h from the start. The overshoot, and undershoot in the partial pressure of nitrogen is evident.

## 7. Description of Tuchlenski, Yang, and Veldsink experiments

Figure 13 presents a schematic showing the two-compartment membrane set-up used in the dynamic experiments reported by Tuchlenski et al.,<sup>9</sup> Yang et al.,<sup>27</sup> and Veldsink et al.<sup>28</sup> The two compartments are separated by a porous membrane. The Tuchlenski and Yang experiments are for a mesoporous Vycor glass membrane; the average pore size of the membrane has values in the range 3.8 to 4.7 nm (data from Table 1 of Tuchlenski paper). The Veldsink experiments are for an alumina membrane with an average pore diameter  $\approx 100$  nm (see page 285 of Veldsink paper). The physical characteristics of the membranes, determined from fitting of noble gas permeation experiments, are summarized in Table 2, Table 3, and Table 4, for the Tuchlenski, Yang, and Veldsink experiments, respectively.

The experiments reported by Tuchlenski, Yang, and Veldsink are for binary mixtures and are analogous in character. The upstream compartment is maintained at constant composition maintaining a through-flow of the gas mixture at constant composition (a stirrer device is also used in the Veldsink experiments). The feed to the upstream compartment occurs at such a rate as to maintain constant compositions in the upstream compartment that correspond to the inlet feed composition. The total

system pressure in the upstream compartment is  $10^5$  Pa. The downstream compartment is closed, and is initially maintained at  $p_{t0} = 10^5$  Pa.

In order to elucidate the experiments, let us consider the experimental data reported by Tuchlenski et al.,<sup>9</sup> for He-Ar mixtures at 293 K; their experimental data are indicated by the symbols in Figure 14. For each mixture, two sets of experiments were performed. In the first set of experiments, the downstream compartment is initially filled with pure Ar, and the upstream compartment is fed with pure He. Initially, the total system pressure in the downstream compartment is  $p_{t0} = 10^5$  Pa. Due to rapid diffusion of He into the downstream compartment, the total pressure,  $p_t$ , in the downstream compartment increases in magnitude. This pressure increase is measured and are indicated in Figure 14 by circles. The plotted data are for  $(p_t - p_{t0})$ . The system will evolve to a steady state wherein the total downstream pressure will equilibrate to  $10^5$  Pa, corresponding also the total system pressure in the upstream compartment.

In the second experiment, the compositions in the upstream and downstream compartments are reversed. Initially, the downstream compartment contains pure He and the upstream compartment is fed with pure Ar. The rapid efflux of He from the downstream compartment, with concomitant influx of Ar, results in a decrease in the downstream pressure,  $p_t$ ; the experimental data are shown by the square symbols in Figure 14.

A differential balance over the “closed” downstream compartment (volume =  $V_{\text{compartment}}$ ) results in

$$V_{\text{compartment}} \frac{1}{RT} \frac{\partial p_t(t)}{\partial t} = A_{\text{membrane}} (N_1(t) + N_2(t)) \quad (37)$$

The solution to the set of equations (5) and (37) need to be carried out numerically, as explained by Veldsink et al.<sup>28</sup> and Tuchlenski et al.<sup>9</sup> The numerical solution procedure is simplified by using the linearization technique suggested by Krishna,<sup>13</sup> as explained below.

In our simulations, the “hold-up” of either component within the membrane layer due to any species adsorption is neglected. This assumption is justified for the following reasons. In Table 5 we present the calculations of the total volume of the pores to that of the downstream compartment; the value

$\frac{V_{pore}}{V_{compartment}} = 1.7 \times 10^{-3}$  for the Tuchlenski and Yang experiments. Therefore, the hold-up within the pores

of the membrane can be neglected without loss of accuracy.

For adsorbing species  $i$ , we adjust the value of  $D_i$  to be a fraction of the value of the corresponding value of the Knudsen diffusivity  $D_{i,Kn}$ , calculated from equation (4). To be consistent with the M-S formulation, we do not account for viscous flow effects; any such effects are subsumed into the values of chosen values of  $D_i$ . It must be pointed out that for the Vycor glass membrane, viscous flow effects are of negligible importance. For the macroporous membrane used in the Veldsink experiments, the viscous flow effects are non-negligible, but small.

The “linearization” procedure essentially involves the assumption that the matrix  $[B]$ , defined in equation (9) for DGM and by equation (27) for the M-S model, can be considered to be constant during the discretized time interval, provided it is evaluated at the average compositions  $\bar{x}_1$  and  $\bar{x}_2$  within the membrane, of thickness  $\delta$ , for the duration of the discretized time interval for integration of equation (37). Essentially, the linearization procedure allows the explicit evaluation of the fluxes for the discretized time interval. The linearized model results in the following expression at time  $t$

$$\begin{pmatrix} N_1(t) \\ N_2(t) \end{pmatrix} = \frac{1}{RT} \frac{[B]^{-1}}{\delta} \begin{pmatrix} (p_{10} - p_{1\delta}(t)) + \bar{x}_1(t) \left( \frac{B_0 p_{1\delta}(t)}{\eta D_{1,Kn}} + 1 \right) (p_0 - p_{1\delta}(t)) \\ (p_{20} - p_{2\delta}(t)) + \bar{x}_2(t) \left( \frac{B_0 p_{1\delta}(t)}{\eta D_{2,Kn}} + 1 \right) (p_0 - p_{1\delta}(t)) \end{pmatrix} \quad (38)$$

For the M-S model, the viscous flow contribution in the second right member of equation (38) is neglected.

Veldsink et al.<sup>28</sup> provides a comparison of the linearized procedure for calculation of the fluxes, with the exact solution to the DGM and has reported “remarkable agreement” between the two sets. In view of this finding, for all the simulations of the Veldsink, Tuchlenski, and Yang experiments, reported below, the linearized procedure was implemented in MathCad 15.<sup>29</sup>

From equations (37) and (38), we see that the geometrical parameter  $\frac{V_{compartment}\delta}{A_{membrane}}$  is relevant for the dynamic pressure increase. For the simulations of the Tuchlenski, and Yang experiments, the value of  $\frac{V_{compartment}\delta}{A_{membrane}}$  used in the simulations were calculated using geometrical details provided in Table 1 of Tuchlenski et al.<sup>9</sup> The detailed calculations are also provided in Table 5. Indeed,  $\frac{V_{compartment}\delta}{A_{membrane}}$  is not a fit parameter in our simulations of the Tuchlenski and Yang experiments. These experiments were also simulated by Schlünder et al.<sup>30</sup> but in their simulations the values of  $\frac{V_{compartment}\delta}{A_{membrane}}$  were fitted separately for each individual experiment for each experiment.

The input data for the simulations of Tuchlenski, Yang, and Veldsink experiments are conveniently summarized in Table 2, Table 3, and Table 4 in order to enable interested readers to reproduce our calculations.

## 8. Simulations of transient experiments with poorly adsorbing gases

Let us begin by considering the set of experiments with binary mixture consisting of components that have poor adsorption on the pore surfaces.

Consider first the He(1)-Ar(2) experiments of Tuchlenski for permeation across a Vycor glass membrane with a pore size  $d_p \approx 4$  nm; see Figure 14. The viscous flow contributions are small; the term

$\frac{B_0 p_t}{\eta} \left( \frac{x_1}{D_{1,Kn}} + \frac{x_2}{D_{2,Kn}} \right)$  indicates the fractional contribution of viscous flow to the changes in the total

pressure. The fractional viscous flow contribution to changes in total pressure is negligibly small

$\frac{B_0 p_t}{\eta} \left( \frac{x_1}{D_{1,Kn}} + \frac{x_2}{D_{2,Kn}} \right) = 8.8 \times 10^{-3}$ . The transport fluxes are dominated by molecule-wall interactions, as

is evident from the values  $\frac{D_{1,Kn}^e}{D_{12}^e} = \frac{D_{1,Kn}}{D_{12}} = 0.05$  and  $\frac{D_{2,Kn}^e}{D_{12}^e} = \frac{D_{2,Kn}}{D_{12}} = 0.016$ . The continuous solid lines in

Figure 14 are the solutions to equation (37), in combination with equation (10) obtained from a numerical algorithm implemented in MathCad 15. There is excellent agreement between the experimental data and the DGM model. Similar good agreement is also reported by Tuchlenski et al;<sup>9</sup> see Figure 5 of their paper.

Figure 15 shows the experimental data of Yang et al.<sup>27</sup> for the dynamic pressure increase in the downstream compartment for He(1)-N<sub>2</sub>(2) mixtures at 293 K. The viscous flow contributions are small

but finite; the term  $\frac{B_0 p_t}{\eta} \left( \frac{x_1}{D_{1,Kn}} + \frac{x_2}{D_{2,Kn}} \right)$  indicates the fractional contribution of viscous flow to the

changes in the total pressure. The fractional viscous flow contribution to changes in total pressure is

$\frac{B_0 p_t}{\eta} \left( \frac{x_1}{D_{1,Kn}} + \frac{x_2}{D_{2,Kn}} \right) = 0.165$ . The continuous solid lines are the calculations using the DGM model.

We note that there is excellent agreement between experiments and simulations, as is to be expected for poorly adsorbing gases.

Consider next the data of Veldsink et al.<sup>28</sup> for He-Ar mixtures; the Veldsink experiments are for an alumina membrane with an average pore size  $d_p \approx 100$  nm. The viscous flow contributions are small but

finite; the term  $\frac{B_0 p_t}{\eta} \left( \frac{x_1}{D_{1,Kn}} + \frac{x_2}{D_{2,Kn}} \right)$  indicates the fractional contribution of viscous flow to the changes

in the total pressure. The fractional viscous flow contribution to changes in total pressure is

$\frac{B_0 p_t}{\eta} \left( \frac{x_1}{D_{1,Kn}} + \frac{x_2}{D_{2,Kn}} \right) = 0.098$ . The transport fluxes are dictated by both molecule-wall and molecule-

molecule interactions, as is evident from the values  $\frac{D_{1,Kn}^e}{D_{12}^e} = 0.916$  and  $\frac{D_{2,Kn}^e}{D_{12}^e} = 0.29$ . The continuous

solid lines in Figure 16a are the solutions to equation (37), in combination with equation (10) obtained from a numerical algorithm implemented in MathCad 15. There is excellent agreement between the

experimental data and the DGM model. Similar good agreement for He-Ar mixtures is also reported by

Veldsink et al.<sup>28</sup>

Figure 16b presents a comparison of the experimental data of Veldsink et al.<sup>28</sup> for He-N<sub>2</sub> mixtures with the solution to the DGM model. The viscous flow contributions are small but finite; the term

$\frac{B_0 p_t}{\eta} \left( \frac{x_1}{D_{1,Kn}} + \frac{x_2}{D_{2,Kn}} \right)$  indicates the fractional contribution of viscous flow to the changes in the total

pressure. The fractional viscous flow contribution to changes in total pressure is

$\frac{B_0 p_t}{\eta} \left( \frac{x_1}{D_{1,Kn}} + \frac{x_2}{D_{2,Kn}} \right) = 0.108$ . The transport fluxes are dictated by both molecule-wall and molecule-

molecule interactions, as is evident from the values  $\frac{D_{1,Kn}^e}{D_{12}^e} = 0.946$  and  $\frac{D_{2,Kn}^e}{D_{12}^e} = 0.358$ . Again, excellent

agreement between the DGM model and experiments is realized, in agreement with the findings of Veldsink et al.<sup>28</sup>

## 9. Transient overshoots/undershoots for mixture uptake within adsorbent particles

Overshoots, and undershoots are also possible for mixture diffusion inside mesoporous and macroporous particles. In order to demonstrate this, we perform simulations for uptake of binary He-Armixtures inside a spherical mesoporous adsorbent particle.

For transient unary uptake within a spherical particle of radius  $r_c$ , the radial distribution of pore concentrations,  $c_i$ , is obtained from a solution of a set of differential equations describing the uptake

$$\varepsilon \frac{\partial c_i(r,t)}{\partial t} = -\frac{1}{r^2} \frac{\partial}{\partial r} (r^2 N_i) \quad (39)$$

At any time  $t$ , during the transient approach to thermodynamic equilibrium, the spatially averaged molar concentration within the adsorbent particle of radius  $r_c$  is obtained by integration of the radial loading profile

$$\bar{c}_i(t) = \frac{3}{r_c^3} \int_0^{r_c} c_i(r,t) r^2 dr \quad (40)$$



An analytical solution to equation (39) is only possible for the special case in which the matrix  $[B]$ , defined by equation (9) can be considered constant for the range of concentrations encountered within the particle.

Let us consider a particle that has the uniform concentration ( $c_0$ ). At time  $t = 0$ , the external surface is brought into contact with a mixture of composition ( $c_{r=rc}$ ). The surface concentration ( $c_{r=rc}$ ) is maintained for the entire duration of the equilibration process. The expression for fractional approach departure from equilibrium is given by the 2-dimensional matrix equation

$$\left(\bar{c}(t) - c_{r=rc}\right) = [Q](c_0 - c_{r=rc}); \quad [Q] \equiv \frac{6}{\pi^2} \sum_{m=1}^{\infty} \frac{1}{m^2} \exp\left[-m^2 \pi^2 \frac{[B]^{-1} t}{r_c^2}\right] \quad (41)$$

The matrix  $[Q]$  quantifies the departure from equilibrium. The Sylvester theorem, detailed in Appendix A of Taylor and Krishna,<sup>31</sup> is required for explicit calculation of the composition trajectories described by Equation (41).

Figure 17 shows the simulations for transient uptake of He-Ar mixtures in a spherical adsorbent particle of radius 2 mm. The chosen temperature of operation is 293 K, and the structural parameters used to calculate the intra-particle diffusivities are the same as those used to model the Tuchlenski experiments; these are specified in Table 2. Initially, the partial pressures of He, and Ar are  $p_{10} = 0$  kPa,  $p_{20} = 100$  kPa, respectively. At time  $t = 0$ , the external surface is maintained at  $p_{1,eq} = 100$  kPa,  $p_{2,eq} = 0$  kPa. The time-evolution of the partial pressures, and total pressures are shown.

There is an overshoot in the total pressure, due to rapid influx of the more mobile helium inside the pores of the particle.

Pressure overshoots are also observed for transient uptake inside particle made of mesoporous Vycor glass exposed to a gas phase He(1)/N<sub>2</sub>(2) mixture at 293 K. The structural information about Vycor glass has been taken from Yang et al.<sup>27</sup> The average pore diameter is 4 nm. For mesoporous particles, there is a core region in which the molecules do not experience any interactions with the pore wall. The molecule-molecule interactions are described by the bulk gas phase diffusivity for He-N<sub>2</sub> mixtures at 293 K, that can be calculated from the FSG method:  $D_{12} = 7.168 \times 10^{-5} \text{ m}^2 \text{ s}^{-1}$ . We performed uptake

simulations for a spherical particle made of radius = 2 mm, in which the particle is first equilibrated with partial pressures are  $p_1 = 0$  kPa;  $p_2 = 100$  kPa, For times,  $t \geq 0$ , the partial pressures of the components in the bulk gas phase are maintained at  $p_1 = 100$  kPa;  $p_2 = 0$ . This implies that there is influx of the more mobile He molecules and efflux of the tardier  $N_2$ . Due to the more rapid influx of He, there is an overshoot in the total pressure,  $p_t = p_1 + p_2$ , during the earlier transience; see Figure 18.

Pressure overshoots within mesoporous catalysts are not uncommon; see Jackson<sup>32</sup> for detailed discussions.

## 10. Simulations of Tuchlenski experiments with adsorbing gases

Tuchlenski et al.<sup>9</sup> report experimental data for dynamic pressure changes during permeation of He-CO<sub>2</sub>, and He-C<sub>3</sub>H<sub>8</sub> mixtures at 293 K, at 343 K. Their experimental data are shown by the circle and square symbols in Figure 19, and Figure 20. The simulations using the DGM equation (5) do not yield good agreement with the He-CO<sub>2</sub> and He-C<sub>3</sub>H<sub>8</sub> experimental data. Tuchlenski et al.<sup>9</sup> properly recognize that the deviations are due to finite adsorption on the pore walls of CO<sub>2</sub>, and C<sub>3</sub>H<sub>8</sub>. In the DGM concept (see Figure 1), surface diffusion is an additive and parallel contribution to the component fluxes. Tuchlenski et al.<sup>9</sup> have modelled the dynamic permeation experiments by means of a surface diffusion model developed by Krishna.<sup>7, 8</sup> In Table 5 of the Tuchlenski paper, values of surface diffusivities of CO<sub>2</sub>, and C<sub>3</sub>H<sub>8</sub> are reported for 293 K, at 343 K; these values may be regarded as “fitted parameters”. The fitted values of the surface diffusivities have values in the range  $2.2$  to  $4 \times 10^{-9} \text{ m}^2 \text{ s}^{-1}$ .

We adopt a different approach to simulating the Tuchlenski experiments, using the Maxwell-Stefan Equation (22), as applied to mesoporous materials.<sup>15-18</sup> Using MD simulations for a wide variety of unary and binary systems in pores ranging from 2 nm to 20 nm in size,<sup>15-19, 21-23, 33-36</sup> we anticipate that the M-S diffusivity  $\bar{D}_i$  to be lower than the corresponding Knudsen diffusivity  $D_{i,Kn}$  by a factor that depends on the adsorption strength.

Tuchlenski et al.<sup>9</sup> have also measured the adsorption isotherm for CO<sub>2</sub> and C<sub>3</sub>H<sub>8</sub> at 293 K and 343 K; see Table 2 of their paper for the Langmuir adsorption constants. Based on the adsorption isotherms we

note that CO<sub>2</sub> has stronger adsorption strength than C<sub>3</sub>H<sub>8</sub>. We should therefore expect that the following hierarchy of M-S diffusivities:  $D_{CO_2} < D_{C_3H_8}$ . Since the adsorption strength decreases with increasing temperature, we should also expect  $D_{CO_2,293K} < D_{CO_2,343K}$ , and  $D_{C_3H_8,293K} < D_{C_3H_8,343K}$ .

In applying the M-S equations to model the Tuchlenski experiments in Figure 19, and Figure 20, there are only two adjustable parameters, viz.  $D_{CO_2}$ , and  $D_{C_3H_8}$ .

For the He-CO<sub>2</sub> mixture permeation data at 293 K, and 343 K shown in Figure 19, reasonably good match with experiments are obtained by taking  $D_{CO_2} = 0.55D_{CO_2,Kn}$  for 293 K data, and  $D_{CO_2} = 0.7D_{CO_2,Kn}$  for 343 K data. The higher value of  $D_{CO_2}$  at 343 K is because the adsorption strength is lower at the higher temperature.

For the He-C<sub>3</sub>H<sub>8</sub> mixture permeation data at 293 K, and 343 K in Figure 20, reasonably good match with experiments are obtained by taking  $D_{C_3H_8} = 0.78D_{C_3H_8,Kn}$  for 293 K data, and  $D_{C_3H_8} = 0.87D_{C_3H_8,Kn}$  for 343 K data. The higher value of  $D_{C_3H_8}$  at 343 K is because the adsorption strength is lower at the higher temperature.

Tuchlenski et al.<sup>9</sup> have also published experimental data for CO<sub>2</sub>-C<sub>3</sub>H<sub>8</sub> mixtures at 293 K; see Figure 21. The two set of experiments are for switching pure CO<sub>2</sub> with 1:1 CO<sub>2</sub>/C<sub>3</sub>H<sub>8</sub> mixture and vice versa. In this case, the DGM equation (5) predicts a pressure increase close to zero because the values of the Knudsen diffusivities for both CO<sub>2</sub>, and C<sub>3</sub>H<sub>8</sub> are almost identical because of their near-equal molar masses. This is also evident from Equation (8) for equimolar counter-diffusion; if both Knudsen diffusivities are identical, the total flux  $N_t$ , calculated from the DGM neglecting surface diffusion, and there is no change in the total system pressure,  $p_t$ .

The experimental data in Figure 21 provide us with an opportunity to test the predictive capability of the M-S formulation because the values  $D_{CO_2} = 0.55D_{CO_2,Kn}$ , and  $D_{C_3H_8} = 0.78D_{C_3H_8,Kn}$  at 293 K have already available from the earlier fits. The dashed lines in Figure 21 are the calculations from the M-S model using these input data values. The agreement between the simulations and experimental data is remarkably good and confirms the predictive capability of the M-S theory.

The M-S model calculations are extremely sensitive to the choice of the values of the M-S diffusivities  $D_{CO_2}$ , and  $D_{C_3H_8}$ . In order to demonstrate this, we compare the experimental data with different scenarios for  $D_{CO_2}$ , while maintaining the value  $D_{C_3H_8} = 0.78D_{C_3H_8,Kn}$ . For the experiment in which the downstream compartment is pure  $CO_2$ , and the upstream compartment contains a 1:1  $CO_2/C_3H_8$  mixture of constant composition, the M-S model calculations taking  $D_{CO_2}$  as a factor 1.0, 0.78, 0.55, and 0.45 times the Knudsen value are shown in Figure 22. For the choice  $D_{CO_2} = 1.0D_{CO_2,Kn}$ , the model predicts a decrease in the downstream compartment pressure, because  $C_3H_8$  is the tardier component in this scenario. The choice  $D_{CO_2} = 0.78D_{CO_2,Kn}$  anticipates no increase or decrease in the total pressure, because the mobilities of both guest species are the same. In other words, the changes in the downstream pressure are linked to differences in the mobilities of the guest molecules. The choice  $D_{CO_2} = 0.45D_{CO_2,Kn}$  predicts a significantly larger increase in the downstream pressure than observed in the experiments.

In order to elucidate the differences in the DGM model neglecting surface diffusion and the M-S model with adjusted values of  $D_{CO_2}$ , and  $D_{C_3H_8}$ , Figure 23a provides a comparison of the transmembrane fluxes calculated by the DGM (continuous solid lines) and Maxwell-Stefan (dashed lines) models for the Tuchlenski experiments for  $CO_2-C_3H_8$  mixtures at 293 K in which the downstream compartment is initially filled with  $CO_2$ , and the upstream compartment is maintained at constant composition with a 1:1  $CO_2-C_3H_8$  mixture at  $10^5$  Pa. Since the Knudsen diffusivities of  $D_{CO_2,Kn}$ , and  $D_{C_3H_8,Kn}$  are almost identical, the transmembrane fluxes sum to zero,  $N_1 + N_2 = N_t \approx 0$ ; this follows directly from Equation (8). Due to stronger adsorption of  $CO_2$ , this component moves more tardily within the pores. This implies that  $CO_2$  vacates the downstream compartment less quickly than the influx of  $C_3H_8$  from the left compartment. The net result is a positive total flux  $N_1 + N_2 = N_t > 0$  directed into the downstream compartment; see the dashed lines in Figure 23a; this net flux results in a pressure increase during transient equilibration.

Figure 23b shows the calculations of the component permeances  $\Pi_i$  using the DGM and M-S model calculations

$$\Pi_i = \frac{N_i}{p_{i0} - p_{i\delta}(t)} \quad (42)$$

From DGM calculations, the permeances of  $\text{CO}_2$  and  $\text{C}_3\text{H}_8$  are indistinguishable from each other because of the use of the Knudsen prescriptions. The M-S model calculations, on the other hand, show the permeance of  $\text{CO}_2$  is lower than that of  $\text{C}_3\text{H}_8$  by about 25% to 45%.

Our analysis of the Tuchlenski experiments with the M-S model leads to the conclusion that the permeance of  $\text{CO}_2$  should indeed be lower than that of  $\text{C}_3\text{H}_8$  due to its stronger adsorption.

## 11. Simulations of Yang experiments with adsorbing gases

Figure 24 presents a comparison of experimental data of Yang et al.<sup>27</sup> for the dynamic pressure increase in the downstream compartment for He- $\text{CO}_2$  mixtures at 293 K with model calculations. The continuous solid lines are the calculations using the DGM equation (5). The dashed lines are the calculations using the M-S equation (25), taking  $D_{\text{He}} = D_{\text{He,Kn}}$  and  $D_{\text{CO}_2} = 0.55D_{\text{CO}_2,\text{Kn}}$ . These results are analogous to those presented in Figure 19 for analysis of Tuchlenski data. The adjusted M-S diffusivity of  $\text{CO}_2$  for use in the modelling of the Yang experiments is nearly the same as those used to model the Tuchlenski experiments. The M-S diffusivity of  $\text{CO}_2$  is lowered below the corresponding Knudsen prescription because of strong adsorption on the pore walls.

Figure 25 compares the experimental data of Yang et al.<sup>27</sup> for the dynamic pressure increase in the downstream compartment for  $\text{CO}_2$ - $\text{C}_3\text{H}_8$  mixtures at 293 K with the DGM and M-S models. The two sets of experiments are for switching pure  $\text{CO}_2$  with pure  $\text{C}_3\text{H}_8$ , and vice versa. The continuous solid lines are the calculations using the DGM equation (5). In this case, the DGM equation (5) predicts a pressure increase close to zero because the values of the Knudsen diffusivities for both  $\text{CO}_2$ , and  $\text{C}_3\text{H}_8$  are almost identical because of their near-equal molar masses. This is also evident from Equation (8); if

both Knudsen diffusivities are identical, the total flux  $N_t$ , calculated from the DGM neglecting surface diffusion, and there is no change in the total system pressure,  $p_t$ .

The dashed lines are the calculations using the M-S equation (25), taking  $D_{CO_2} = 0.55D_{CO_2,Kn}$  and  $D_{C_3H_8} = 0.88D_{C_3H_8,Kn}$ . These results are entirely analogous to those presented in Figure 21 for the Tuchlenski data analysis.

In order to explain the differences in the DGM model, neglecting surface diffusion, and the M-S model with adjusted values of  $D_{CO_2}$ , and  $D_{C_3H_8}$ , Figure 26a provides a comparison of the transmembrane fluxes calculated by the DGM (continuous solid lines) and Maxwell-Stefan (dashed lines) models for the Yang experiments for  $CO_2$ - $C_3H_8$  mixtures at 293 K in which the downstream compartment is initially filled with  $CO_2$ , and the upstream compartment is flushed with pure  $C_3H_8$  at  $10^5$  Pa. Since the Knudsen diffusivities of  $D_{CO_2,Kn}$ , and  $D_{C_3H_8,Kn}$  are almost identical, the transmembrane fluxes sum to zero,  $N_1 + N_2 = N_t \approx 0$ ; this follows directly from Equation (8). Due to stronger adsorption of  $CO_2$ , this component moves more tardily within the pores. This implies that  $CO_2$  vacates the downstream compartment less quickly than the influx of  $C_3H_8$  from the left compartment. The net result is a positive total flux  $N_1 + N_2 = N_t > 0$  directed into the downstream compartment; see the dashed lines in Figure 26a; this net flux results in a pressure increase during transient equilibration.

Figure 26b shows the calculations of the component permeances  $\Pi_i$  using the DGM and M-S model calculations. From DGM calculations, the permeances of  $CO_2$  and  $C_3H_8$  are indistinguishable from each other because of the use of the Knudsen prescriptions. The M-S model calculations, on the other hand, show the permeance of  $CO_2$  is lower than that of  $C_3H_8$  by about 25% to 45%.

Our analysis of the Yang experiments with the M-S model leads to the conclusion that the permeance of  $CO_2$  should indeed be lower than that of  $C_3H_8$  due to its stronger adsorption.

## 12. Ratio of M-S diffusivity to Knudsen diffusivity plotted as a function of Henry coefficient for adsorption

Figure 27 presents a plot of the ratio,  $D_i/D_{i,Kn}$ , determined as explained in the foregoing analysis of both Tuchlenski and Yang experiments, plotted as a function of the Henry coefficient for adsorption. This plot, which is entirely analogous to that derived from MD simulations in Figure 6; this confirms that the lowering in the M-S diffusivity below the Knudsen prescription increases with increasing adsorption strength. The information contained in this graph, provides an engineering approach to the estimation of the M-S diffusivity  $D_i$  by using the Knudsen diffusivity  $D_{i,Kn}$  as a pivotal value for that species.

We list below further experimental data in the literature that strengthen the findings in Figure 6.

In the work of Tsuru et al.<sup>37</sup>, the experimentally determined permeance of strongly adsorbing H<sub>2</sub>O molecules across silica membranes, is significantly lower than anticipated on the basis of its molecular size. This is most likely due to the strong adsorption of H<sub>2</sub>O molecules on the pore walls, causing violation of the Knudsen prescription.

In the experimental study of Katsanos et al.<sup>38</sup>, the ratio  $D_i/D_{i,Kn}$  for diffusion of nC5, nC6 and nC7 in  $\alpha$ -alumina ( $d_p = 21.6$  nm) and  $\gamma$ -alumina ( $d_p = 10.6$  nm) were found to be in the range of 0.1 – 0.27.

Further experimental evidence on departure from the Knudsen prescription is provided by the experimental data reported by Petukhov and Eliseev<sup>39</sup> on the permeances of CO<sub>2</sub>, and C<sub>3</sub>H<sub>8</sub> across an alumina membrane with an average pore diameter  $d_p = 45$  nm. Their data show that permeance of CO<sub>2</sub> is about 90% lower than that of C<sub>3</sub>H<sub>8</sub>. From equation (28),  $\Pi_i = (\varepsilon/\tau)D_i/RT\delta$  for the scenario in which molecule-wall collisions dominate. The data of Petukhov indicate that  $D_{CO_2} \approx 0.9D_{C_3H_8}$ , at variance with the expectations from equation (4).

## 13. Simulations of Veldsink experiments with adsorbing gases

Veldsink et al.<sup>28</sup> report experimental data on the dynamic pressure changes for He-CO<sub>2</sub> mixtures at 293 K, and at 434 K; see Figure 28a, and Figure 28b. Good agreement is obtained with the M-S

formulation taking  $D_{CO_2} = 0.85D_{CO_2,Kn}$  at 293 K and  $D_{CO_2} = 0.9D_{CO_2,Kn}$  at 434 K. The fitted values are somewhat higher than the corresponding values obtained for fitting the corresponding Tuchlenski data (see Figure 19). The reason is that the pore size of the membrane in the Veldsink experiments is 100 nm, considerably larger than the 4 nm pore sized membrane used in the Tuchlenski and Yang experiments. The larger the pore size, the closer is the approach of the M-S diffusivity  $D_{CO_2}$  to the Knudsen limit; this is in conformity with MD simulation data reported in the literature.<sup>15-19, 21-23, 33-36</sup>

The experimental data of Veldsink et al.<sup>28</sup> for He-C<sub>3</sub>H<sub>8</sub> mixtures at 293 K, and 416 K are shown in Figure 29. These data can be matched well by taking  $D_{C_3H_8} = 0.95D_{C_3H_8,Kn}$  at 293 K and  $D_{C_3H_8} = 0.98D_{C_3H_8,Kn}$  at 416 K. These M-S diffusivity values are higher than the corresponding values for CO<sub>2</sub> (see Figure 28) because of the lower adsorption strength of C<sub>3</sub>H<sub>8</sub>.

#### 14. Comparison of Tuchlenski CO<sub>2</sub>/C<sub>3</sub>H<sub>8</sub> experiments with surface diffusion model

In the foregoing analysis of Tuchlenski experiments with CO<sub>2</sub>-C<sub>3</sub>H<sub>8</sub> mixtures, no explicit account was taken of surface diffusion. The model calculations were based on the assumption that the influence of adsorption on the pore walls is to introduce a bias into the hops, and reduce the M-S diffusivities  $D_{CO_2}$ , and  $D_{C_3H_8}$  below those prescribed by the Knudsen formula.

A different modelling approach is to assume that the mechanism of transport of both CO<sub>2</sub>, and C<sub>3</sub>H<sub>8</sub> is exclusively by diffusion along the surface. Since molecule-molecule interactions are of negligible importance, the component fluxes are described by equation (11).

In 2-dimensional matrix, the flux relations are

$$\begin{pmatrix} N_1(t) \\ N_2(t) \end{pmatrix} = \frac{(\varepsilon/\tau)}{\delta} \begin{bmatrix} D_{1,s} & 0 \\ 0 & D_{2,s} \end{bmatrix} \begin{bmatrix} \Gamma_{11} & \Gamma_{12} \\ \Gamma_{21} & \Gamma_{22} \end{bmatrix} \begin{pmatrix} c_{10} - c_{1\delta}(t) \\ c_{20} - c_{2\delta}(t) \end{pmatrix} \quad (43)$$

Equation (43) is used in place of equation (38) for calculation of the fluxes. The driving forces are the differences in the molar concentrations in the pore at the upstream face ( $c_{i0}$ , maintained constant) and



the downstream face of the membrane, ( $c_{i\delta}(t)$ , varying with time). The pore concentrations are calculated using mixed-gas Langmuir model

$$\frac{c_1}{c_{1,sat}} = \theta_1 = \frac{b_1 p_1}{1 + b_1 p_1 + b_2 p_2}; \quad \frac{c_2}{c_{2,sat}} = \theta_2 = \frac{b_2 p_2}{1 + b_1 p_1 + b_2 p_2} \quad (44)$$

using the partial pressures  $p_{i0}$ , and  $p_{i\delta}(t)$ .

For the mixed-gas Langmuir model, equation (44), we can derive simple analytic expressions for the four elements of the matrix of thermodynamic factors:<sup>40</sup>

$$\begin{bmatrix} \Gamma_{11} & \Gamma_{12} \\ \Gamma_{21} & \Gamma_{22} \end{bmatrix} = \frac{1}{1 - \theta_1 - \theta_2} \begin{bmatrix} 1 - \theta_2 & \frac{c_{1,sat}}{c_{2,sat}} \theta_1 \\ \frac{c_{2,sat}}{c_{1,sat}} \theta_2 & 1 - \theta_1 \end{bmatrix} \quad (45)$$

The Langmuir parameters are provided in Table 2 of Tuchlenski et al.<sup>9</sup> To retain thermodynamic consistency, we use the Langmuir fit parameters in which the component saturation capacities of CO<sub>2</sub>, and C<sub>3</sub>H<sub>8</sub> are identical.

We now attempt to try to determine the surface diffusivities,  $D_{i,s}$ , of CO<sub>2</sub>, and C<sub>3</sub>H<sub>8</sub> by matching with experimental data. For this purpose, we assume that the surface diffusivities are independent of pore concentrations. A reasonably good match of the experimental data of Tuchlenski et al.<sup>9</sup> is obtained by taking the values of the M-S surface diffusivities  $D_{CO_2,s} = 0.5D_{CO_2,Kn}$ , and  $D_{C_3H_8,s} = 0.85D_{C_3H_8,Kn}$ ; see the simulation results indicated by the continuous solid lines in Figure 30. The calculations of the surface diffusion model are in fair agreement with the “mesopore diffusion” model in which the M-S diffusivities for hopping along the pore walls was taken as  $D_{CO_2} = 0.55D_{CO_2,Kn}$ , and  $D_{C_3H_8} = 0.78D_{C_3H_8,Kn}$ ; these results were discussed earlier in the context of Figure 21. Remarkably, the use of the surface diffusion model also leads to the conclusion that the M-S surface diffusivities are lowered below the Knudsen prescription, by approximately the same factor as determined from the “mesopore diffusion” model.

Implicit in the results presented in Figure 30 is that the surface diffusion should not be viewed as an additional contribution to the fluxes as is suggested by schematic in Figure 1 that was put forward by Mason and Malinauskas.<sup>1</sup>

## 15. Comparison of Yang CO<sub>2</sub>/C<sub>3</sub>H<sub>8</sub> experiments with surface diffusion model

In the foregoing analysis of Yang experiments with CO<sub>2</sub>-C<sub>3</sub>H<sub>8</sub> mixtures, no explicit account was taken of surface diffusion. The model calculations were based on the assumption that the influence of adsorption on the pore walls is to introduce a bias into the hops, and reduce the M-S diffusivities  $D_{CO_2}$ , and  $D_{C_3H_8}$  below those prescribed by the Knudsen formula.

We now attempt to model the Yang experiments for CO<sub>2</sub>-C<sub>3</sub>H<sub>8</sub> mixtures using the surface diffusion model, described in an earlier section. The Langmuir parameters are provided in Table 1 of Yang et al.<sup>27</sup> To retain thermodynamic consistency we use the Langmuir fit parameters in which the component saturation capacities of CO<sub>2</sub>, and C<sub>3</sub>H<sub>8</sub> are identical.

We now attempt to try to determine the surface diffusivities,  $D_{i,s}$ , of CO<sub>2</sub>, and C<sub>3</sub>H<sub>8</sub> by matching with experimental data. For this purpose, we assume that the surface diffusivities are independent of pore concentrations. A reasonably good match of the experimental data presented in Figure 6 of Yang et al.<sup>27</sup> is obtained by taking the values of the M-S surface diffusivities  $D_{CO_2,s} = 0.35D_{CO_2,Kn}$ , and  $D_{C_3H_8,s} = 0.85D_{C_3H_8,Kn}$ ; see the simulation results indicated by the continuous solid lines in Figure 31.

The calculations of the surface diffusion model are in fair agreement with the “mesopore diffusion” model in which the M-S diffusivities for hopping along the pore walls was taken as  $D_{CO_2} = 0.55D_{CO_2,Kn}$ , and  $D_{C_3H_8} = 0.88D_{C_3H_8,Kn}$ ; these results were discussed earlier in the context of Figure 25. Remarkably, the use of the surface diffusion model also leads to the conclusion that the M-S surface diffusivities are lowered below the Knudsen prescription, by approximately the same factor as determined from the “mesopore diffusion” model.

In Figure 7 of Yang et al,<sup>27</sup> experimental data are presented for dynamic pressure increases in the downstream compartment for varying compositions. For the experiments in which 3:7 CO<sub>2</sub>-C<sub>3</sub>H<sub>8</sub> mixture in the downstream compartment is displaced by 1:9 CO<sub>2</sub>-C<sub>3</sub>H<sub>8</sub> in the upstream compartment, and vice versa, the experimental data on transient pressure changes are properly captured by the surface diffusion model using the same set of values of the M-S surface diffusivities  $D_{CO_2,s} = 0.35D_{CO_2,Kn}$ , and  $D_{C_3H_8,s} = 0.85D_{C_3H_8,Kn}$  as used earlier (in the other set of experiments discussed earlier in Figure 31); see comparisons of simulations with experiment in Figure 32.

## 16. Notation

$A_{\text{membrane}}$	cross-sectional area of membrane, $\text{m}^2$
$B_0$	permeability of pore, $\text{m}^2$
$[B]$	matrix defined by equation (9) for DGM and (27) for M-S model, $\text{m}^{-2} \text{s}$
$c_i$	molar concentration of species $i$ , $\text{mol m}^{-3}$
$c_{i,\text{sat}}$	molar concentration of adsorbed species $i$ at saturation, $\text{mol m}^{-3}$
$c_t$	total molar concentration of mixture, $\text{mol m}^{-3}$
$d_p$	diameter of pore, $\text{m}$
$D_i$	M-S diffusivity for molecule-wall interaction, $\text{m}^2 \text{s}^{-1}$
$D_{i,s}$	M-S diffusivity for surface diffusion, $\text{m}^2 \text{s}^{-1}$
$D_{i,\text{Kn}}$	Knudsen diffusivity of species $i$ , $\text{m}^2 \text{s}^{-1}$
$D_{ij}$	Maxwell-Stefan diffusivity for $i$ - $j$ pair, $\text{m}^2 \text{s}^{-1}$
$K_0$	effective pore size, also called Knudsen number, $\text{m}$
$n$	number of species in the mixture, dimensionless
$N_i$	molar flux of species $i$ with respect to framework, $\text{mol m}^{-2} \text{s}^{-1}$
$p_i$	partial pressure of species $i$ in mixture, $\text{Pa}$
$p_t$	total system pressure, $\text{Pa}$
$r_c$	radius of adsorbent particle, $\text{m}$
$R$	gas constant, $8.314 \text{ J mol}^{-1} \text{ K}^{-1}$
$u_i$	velocity of motion of species $i$ with respect to pore wall, $\text{m s}^{-1}$
$V_{\text{compartment}}$	volume of downstream compartment, $\text{m}^3$
$V_p$	pore volume, $\text{m}^3 \text{ kg}^{-1}$
$x_i$	mole fraction of species $i$ within pore, dimensionless
$T$	absolute temperature, $\text{K}$
$z$	distance coordinate, $\text{m}$

### ***Greek letters***

$\delta$	thickness of membrane, m
$\varepsilon$	pore voidage, dimensionless
$\Gamma_{ij}$	thermodynamic factors, dimensionless
$[\Gamma]$	matrix of thermodynamic factors, dimensionless
$\mu_i$	molar chemical potential of component $i$ , J mol <sup>-1</sup>
$\Pi_i$	permeance of species $i$ in mixture mol m <sup>-2</sup> s <sup>-1</sup> Pa <sup>-1</sup>
$\eta$	viscosity of gas mixture, Pa s
$\theta_i$	fractional occupancy of component $i$ , dimensionless
$\rho$	framework density, kg m <sup>-3</sup>
$\sigma$	Lennard-Jones size parameter, m
$\tau$	tortuosity, dimensionless

### ***Subscripts***

$i$	referring to component $i$
$t$	referring to total mixture

### ***Superscripts***

$e$	effective parameter inside pore
-----	---------------------------------

Table S1. Input data for simulation of Tuchlenski et al.<sup>9</sup> experiments for unary CO<sub>2</sub> permeation. These data are taken from Tables 2, 3 and 5 of Tuchlenski et al.<sup>9</sup> The viscosity data taken from the paper by Veldsink et al.<sup>28</sup>

$$\text{Porosity/Tortuosity: } \frac{\varepsilon}{\tau} = 0.03;$$

$$K_0 = \frac{d_p}{4} \frac{\varepsilon}{\tau} = 6.58 \times 10^{-11} \text{ m};$$

$$\text{Permeability: } B_0^e = \frac{d_p^2}{32} \frac{\varepsilon}{\tau} = 10.8 \times 10^{-20} \text{ m}^2;$$

$$A_{\text{membrane}} = 2.796 \times 10^{-3} \text{ m}^2; \text{ Transfer area from upstream to downstream compartments.}$$

$$\text{Membrane thickness, } \delta = 1.1 \times 10^{-3} \text{ m};$$

Gas phase viscosities:

$$\text{CO}_2 \text{ at 293 K: } \eta = 1.73 \times 10^{-5} \text{ Pa s};$$

$$\text{CO}_2 \text{ at 343 K: } \eta = 2.33 \times 10^{-5} \text{ Pa s};$$

The surface diffusivities are from Table 5 of Tuchlenski et al.<sup>9</sup>

$$\text{CO}_2 \text{ at 293 K: } D_{i,s} = 2.2 \times 10^{-9} \text{ m}^2 \text{ s}^{-1};$$

$$\text{CO}_2 \text{ at 343 K: } D_{i,s} = 2.8 \times 10^{-9} \text{ m}^2 \text{ s}^{-1};$$

Please note that the isotherm data reported by Tuchlenski use  $c_i$  defined in terms of mol of species  $i$  per m<sup>3</sup> of solid material.

Table S2. Input data for simulation of Tuchlenski et al.<sup>9</sup> experiments. These data are taken from Tables 1, 2 and 3 of Tuchlenski et al.<sup>9</sup> The viscosity data taken from the paper by Veldsink et al.<sup>28</sup>

$$\text{Porosity/Tortuosity: } \frac{\varepsilon}{\tau} = 0.03;$$

$$K_0 = \frac{d_p}{4} \frac{\varepsilon}{\tau} = 6.58 \times 10^{-11} \text{ m};$$

$$\text{Permeability: } B_0^e = \frac{d_p^2}{32} \frac{\varepsilon}{\tau} = 10.8 \times 10^{-20} \text{ m}^2;$$

$$\frac{V_{\text{compartment}}}{A_{\text{membrane}}} \delta = 4 \times 10^{-6} \text{ m}^2;$$

1-site Langmuir parameters for CO<sub>2</sub> and C<sub>3</sub>H<sub>8</sub> in Vycor glass. From Table 2 of Tuchlenski.

	$q_{\text{sat}}$ mol kg <sup>-1</sup>	$b$ Pa <sup>-1</sup>
CO <sub>2</sub>	1.35	6.01 × 10 <sup>-6</sup>
C <sub>3</sub> H <sub>8</sub>	1.35	2.87 × 10 <sup>-6</sup>

Bulk gas phase diffusivities, and gas phase viscosities:

$$\text{He-Ar at 293 K: } D_{12} = 7.34 \times 10^{-5} \text{ m}^2 \text{ s}^{-1}; \eta = 2.32 \times 10^{-5} \text{ Pa s};$$

$$\text{He-CO}_2 \text{ at 293 K: } D_{12} = 5.792 \times 10^{-5} \text{ m}^2 \text{ s}^{-1}; \eta = 1.73 \times 10^{-5} \text{ Pa s};$$

$$\text{He-CO}_2 \text{ at 343 K: } D_{12} = 7.541 \times 10^{-5} \text{ m}^2 \text{ s}^{-1}; \eta = 2.33 \times 10^{-5} \text{ Pa s};$$

$$\text{He-C}_3\text{H}_8 \text{ at 293 K: } D_{12} = 4 \times 10^{-5} \text{ m}^2 \text{ s}^{-1}; \eta = 1.04 \times 10^{-5} \text{ Pa s};$$

$$\text{He-C}_3\text{H}_8 \text{ at 343 K: } D_{12} = 5.23 \times 10^{-5} \text{ m}^2 \text{ s}^{-1}; \eta = 1.36 \times 10^{-5} \text{ Pa s};$$

$$\text{CO}_2\text{-C}_3\text{H}_8 \text{ at 293 K: } D_{12} = 9 \times 10^{-6} \text{ m}^2 \text{ s}^{-1}; \text{estimated for the Fuller-Schettler-Giddings method.}^{2,3}$$

$$\eta = 1.04 \times 10^{-5} \text{ Pa s};$$

Note: All of the above parameters are input data for DGM equation (5). In using the M-S equation (25), the viscous flow contribution is omitted.

Table S3. Input data for simulation of Yang et al.<sup>27</sup> experiments. These data are taken from Tables 1 and 2 of Yang et al.<sup>27</sup> The viscosity data taken from the paper by Veldsink et al.<sup>28</sup>

$$\text{Porosity/Tortuosity: } \frac{\varepsilon}{\tau} = 0.039;$$

$$K_0 = \frac{d_p}{4} \frac{\varepsilon}{\tau} = 6.346 \times 10^{-11} \text{ m};$$

$$\text{Permeability: } B_0^e = \frac{d_p^2}{32} \frac{\varepsilon}{\tau} = 1.748 \times 10^{-18} \text{ m}^2;$$

$$\frac{V_{\text{compartment}} \delta}{A_{\text{membrane}}} = 4 \times 10^{-6} \text{ m}^2;$$

1-site Langmuir parameters for CO<sub>2</sub> and C<sub>3</sub>H<sub>8</sub> in Vycor glass; from Table 1 of Yang.

	$q_{\text{sat}}$ mol kg <sup>-1</sup>	$b$ Pa <sup>-1</sup>
CO <sub>2</sub>	0.8264	8.54×10 <sup>-6</sup>
C <sub>3</sub> H <sub>8</sub>	0.8264	4.01×10 <sup>-6</sup>

Bulk gas phase diffusivities, and gas phase viscosities:

$$\text{He-N}_2 \text{ at } 293 \text{ K: } D_{12} = 7.168 \times 10^{-5} \text{ m}^2 \text{ s}^{-1}; \eta = 1.83 \times 10^{-5} \text{ Pa s};$$

$$\text{He-CO}_2 \text{ at } 293 \text{ K: } D_{12} = 5.792 \times 10^{-5} \text{ m}^2 \text{ s}^{-1}; \eta = 1.73 \times 10^{-5} \text{ Pa s};$$

$$\text{CO}_2\text{-C}_3\text{H}_8 \text{ at } 293 \text{ K: } D_{12} = 9 \times 10^{-6} \text{ m}^2 \text{ s}^{-1}; \text{ estimated for the Fuller-Schettler-Giddings method.}^{2,3}$$

$$\eta = 1.04 \times 10^{-5} \text{ Pa s};$$

Note: All of the above parameters are input data for DGM equation (5). In using the M-S equation (25), the viscous flow contribution is omitted.



Table S4. Input data for simulation of Veldsink<sup>28</sup> experiments. These data are taken from Table 5 of Veldsink et al.<sup>28</sup> The viscosity data are taken from the legends to Figures 9, 11, 12, 13, 14, and 15 of Veldsink et al.<sup>28</sup>

$$\text{Porosity/Tortuosity: } \frac{\varepsilon}{\tau} = 0.08;$$

$$K_0 = \frac{d_p}{4} \frac{\varepsilon}{\tau} = 3.24 \times 10^{-9} \text{ m; Pore diameter: } d_p = 0.162 \text{ } \mu\text{m};$$

$$\text{Permeability: } B_0^e = \frac{d_p^2}{32} \frac{\varepsilon}{\tau} = 5.89 \times 10^{-17} \text{ m}^2;$$

$$\frac{V_{\text{compartment}} \delta}{A_{\text{membrane}}} = 5.625 \times 10^{-5} \text{ m}^2;$$

Bulk gas phase diffusivities, and gas phase viscosities:

$$\text{He-Ar at 293 K: } D_{12} = 7.34 \times 10^{-5} \text{ m}^2 \text{ s}^{-1}; \eta = 2.32 \times 10^{-5} \text{ Pa s};$$

$$\text{He-N}_2 \text{ at 298 K: } D_{12} = 7.168 \times 10^{-5} \text{ m}^2 \text{ s}^{-1}; \eta = 1.83 \times 10^{-5} \text{ Pa s};$$

$$\text{He-CO}_2 \text{ at 293 K: } D_{12} = 5.792 \times 10^{-5} \text{ m}^2 \text{ s}^{-1}; \eta = 1.73 \times 10^{-5} \text{ Pa s};$$

$$\text{He-CO}_2 \text{ at 434 K: } D_{12} = 11.384 \times 10^{-5} \text{ m}^2 \text{ s}^{-1}; \eta = 2.33 \times 10^{-5} \text{ Pa s};$$

$$\text{He-C}_3\text{H}_8 \text{ at 298 K: } D_{12} = 4.158 \times 10^{-5} \text{ m}^2 \text{ s}^{-1}; \eta = 1.04 \times 10^{-5} \text{ Pa s};$$

$$\text{He-C}_3\text{H}_8 \text{ at 416 K: } D_{12} = 7.336 \times 10^{-5} \text{ m}^2 \text{ s}^{-1}; \eta = 1.36 \times 10^{-5} \text{ Pa s};$$

Note: All of the above parameters are input data for DGM equation (5). In using the M-S equation (25), the viscous flow contribution is omitted.

Table S5. Membrane geometry for Tuchlenski and Yang experiments. The geometrical details are taken from Table 1 of Tuchlenski et al.<sup>9</sup>

Inner radius of membrane:  $r_1 = 3.9 \times 10^{-3}$  m;

Outer radius of membrane:  $r_2 = 5 \times 10^{-3}$  m;

Thickness of membrane:  $\delta = 1.1 \times 10^{-3}$  m;

Membrane length:  $L = 0.1$  m;

Volume of downstream compartment:  $V_{compartment} = 10.4 \times 10^{-6}$  m<sup>3</sup>;

Area of membrane for calculation of fluxes:  $A_{membrane} = 2\pi \left( \frac{r_1 + r_2}{2} \right) L = 2.796 \times 10^{-3}$  m<sup>2</sup>;

From above data we calculate:  $\frac{V_{compartment} \delta}{A_{membrane}} = 4.1 \times 10^{-6}$  m<sup>2</sup>;

The value used in the simulation of Tuchlenski and Yang experiments:  $\frac{V_{compartment} \delta}{A_{membrane}} = 4 \times 10^{-6}$  m<sup>2</sup>;

Porosity of membrane  $\varepsilon = 0.284$ .

Total volume of pores within membrane layer:  $V_{pore} = \pi(r_2^2 - r_1^2)L\varepsilon = 1.77 \times 10^{-8}$ .

Ratio of total pore volume to downstream compartment volume  $\frac{V_{pore}}{V_{compartment}} = 1.7 \times 10^{-3}$

## 17. References

- (1) Mason, E. A.; Malinauskas, A. P. *Gas Transport in Porous Media: The Dusty-Gas Model*; Elsevier: Amsterdam, 1983.
- (2) Fuller, E. N.; Schettler, P. D.; Giddings, J. C. A New Method for Prediction of Binary Gas-phase Diffusion Coefficients. *Ind. Eng. Chem.* **1966**, *58*, 19.
- (3) Reid, R.C.; Prausnitz, J. M.; Poling, B. E. *The Properties of Gases and Liquids*; 4th Edition, McGraw-Hill: New York, 1986.
- (4) Knudsen, M. Die Gesetze der Molekularströmung und der inneren Reibungsströmung der Gase durch Röhren. *Ann. Phys.* **1909**, *333*, 75.
- (5) Smoluchowski, M. Zur Kinetischen Theorie der Transpiration und Diffusion verdünnter Gase. *Ann. Phys.* **1910**, *338*, 1559.
- (6) Gruener, S.; Huber, P. Knudsen Diffusion in Dilicon Nanochannels. *Phys. Rev. Lett.* **2008**, *100*, 064502.
- (7) Krishna, R. Multicomponent Surface Diffusion of Adsorbed Species - A Description Based on the Generalized Maxwell-Stefan Equations. *Chem. Eng. Sci.* **1990**, *45*, 1779.
- (8) Krishna, R. Problems and Pitfalls in the Use of the Fick Formulation for Intraparticle Diffusion. *Chem. Eng. Sci.* **1993**, *48*, 845.
- (9) Tuchlenski, A.; Uchytel, P.; Seidel-Morgenstern, A. An Experimental Study of Combined Gas Phase and Surface Diffusion in Porous Glass. *J. Membr. Sci.* **1998**, *140*, 165.
- (10) Wu, K.; Li, X.; Wang, C.; Yu, W.; Chen, Z. Model for Surface Diffusion of Adsorbed Gas in Nanopores of Shale Gas Reservoirs. *Ind. Eng. Chem. Res.* **2015**, *54*, 3225.
- (11) Young, J. B.; Todd, B. Modelling of Multi-Component Gas Flows in Capillaries and Porous Solids. *Int. J. Heat Mass Transfer* **2005**, *48*, 5338.
- (12) Kerkhof, P. J. A. M. A Modified Maxwell-Stefan Model for Transport Through Inert Membranes: The Binary Friction Model. *Chem. Eng. J.* **1996**, *64*, 319.
- (13) Krishna, R. A Simplified Procedure for the Solution of the Dusty Gas Model Equations for Steady-State Transport in Non-Reacting Systems. *Chem. Eng. J.* **1987**, *35*, 75.
- (14) Remick, R. R.; Geankoplis, C. J. Ternary Diffusion of Gases in Capillaries in the Transition Region Between Knudsen and Molecular Diffusion. *Chem. Eng. Sci.* **1974**, *29*, 1447.
- (15) Krishna, R.; van Baten, J. M. An Investigation of the Characteristics of Maxwell-Stefan Diffusivities of Binary Mixtures in Silica Nanopores. *Chem. Eng. Sci.* **2009**, *64*, 870.
- (16) Krishna, R.; van Baten, J. M. Unified Maxwell-Stefan Description of Binary Mixture Diffusion in Micro- and Meso- Porous Materials. *Chem. Eng. Sci.* **2009**, *64*, 3159.
- (17) Krishna, R. Describing the Diffusion of Guest Molecules inside Porous Structures. *J. Phys. Chem. C* **2009**, *113*, 19756.
- (18) Krishna, R. Diffusion in Porous Crystalline Materials. *Chem. Soc. Rev.* **2012**, *41*, 3099.
- (19) Krishna, R.; van Baten, J. M. Influence of Adsorption on the Diffusion Selectivity for Mixture Permeation across Mesoporous Membranes. *J. Membr. Sci.* **2011**, *369*, 545.
- (20) Krishna, R.; Wesselingh, J. A. The Maxwell-Stefan Approach to Mass Transfer. *Chem. Eng. Sci.* **1997**, *52*, 861.
- (21) Bhatia, S. K.; Bonilla, M. R.; Nicholson, D. Molecular Transport in Nanopores: A Theoretical Perspective. *Phys. Chem. Chem. Phys.* **2011**, *13*, 15350.
- (22) Krishna, R.; van Baten, J. M. A Molecular Dynamics Investigation of the Unusual Concentration Dependencies of Fick Diffusivities in Silica Mesopores. *Microporous Mesoporous Mater.* **2011**, *138*, 228.

- (23) Krishna, R.; van Baten, J. M. Investigating the Validity of the Knudsen Prescription for Diffusivities in a Mesoporous Covalent Organic Framework. *Ind. Eng. Chem. Res.* **2011**, *50*, 7083.
- (24) Krishna, R.; van Baten, J. M. Investigating the Validity of the Bosanquet Formula for Estimation of Diffusivities in Mesopores. *Chem. Eng. Sci.* **2012**, *69*, 684.
- (25) Duncan, J. B.; Toor, H. L. An Experimental Study of Three Component Gas Diffusion. *A.I.Ch.E.J.* **1962**, *8*, 38.
- (26) Krishna, R. Uphill Diffusion in Multicomponent Mixtures. *Chem. Soc. Rev.* **2015**, *44*, 2812.
- (27) Yang, J.; Čermáková, J.; Uchytíl, P.; Hamel, C.; Seidel-Morgenstern, A. Gas Phase Transport, Adsorption and Surface Diffusion in a Porous Glass Membrane. *Catal. Today* **2005**, *104*, 344.
- (28) Veldsink, J. W.; Versteeg, G. F.; Van Swaaij, W. P. M. An Experimental Study of Diffusion and Convection of Multicomponent Gases through Catalytic and Non-Catalytic Membranes. *J. Membr. Sci.* **1994**, *92*, 275.
- (29) PTC MathCad 15.0. <http://www.ptc.com/>, PTC Corporate Headquarters, Needham, 3 November 2015.
- (30) Schlünder, E. U.; Yang, J.; Seidel-Morgenstern, A. Competitive Diffusion and Adsorption in Vycor Glass Membranes—A Lumped Parameter Approach. *Catal. Today* **2006**, *118*, 113.
- (31) Taylor, R.; Krishna, R. *Multicomponent mass transfer*; John Wiley: New York, 1993.
- (32) Jackson, R. *Transport in Porous Catalysts*; Elsevier: Amsterdam, 1977.
- (33) Bhatia, S. K.; Nicholson, D. Comments on ‘‘Diffusion in a Mesoporous Silica Membrane: Validity of the Knudsen Diffusion Model’’. *Chem. Eng. Sci.* **2010**, *65*, 4519.
- (34) Bhatia, S. K.; Jepps, O.; Nicholson, D. Tractable Molecular Theory of Transport of Lennard-Jones Fluids in Nanopores. *J. Chem. Phys.* **2004**, *120*, 4472.
- (35) Bhatia, S. K.; Nicholson, D. Transport of Simple Fluids in Nanopores: Theory and Simulation. *A.I.Ch.E.J.* **2006**, *52*, 29.
- (36) Bhatia, S. K. Modeling Pure Gas Permeation in Nanoporous Materials and Membranes. *Langmuir* **2010**, *26*, 8373.
- (37) Tsuru, T.; Igi, R.; Kanezashi, M.; Yoshioka, T.; Fujisaki, S.; Iwamoto, Y. Permeation Properties of Hydrogen and Water Vapor Through Porous Silica Membranes at High Temperatures. *A.I.Ch.E.J.* **2011**, *57*, 618.
- (38) Katsanos, N. A.; Bakaoukas, N.; Koliadima, A.; Karaiskakis, G. Diffusion and Adsorption Measurements in Porous Solids by Inverse Gas Chromatography. *J. Phys. Chem. B* **2005**, *109*, 11240.
- (39) Petukhov, D. I.; Eliseev, A. A. Gas Permeation Through Nanoporous Membranes in the Transitional Flow Region. *Nanotechnology* **2016**, *27*, 085707.
- (40) Krishna, R.; Baur, R. Modelling Issues in Zeolite Based Separation Processes. *Sep. Purif. Technol.* **2003**, *33*, 213.

## 18. Caption for Figures

Figure S1. Electric analog circuit picturing the flux of the diffusing species within a porous medium. Adapted from Mason and Malinauskas,<sup>1</sup>

Figure S2. (a) Knudsen ( $D_{\text{He,Kn}}$ ,  $D_{\text{Ar,Kn}}$ ), and bulk diffusivities ( $D_{\text{He,Ar}}$ ) of He/Ar mixtures at 293 K in cylindrical mesopores and macropores. The calculations of the bulk diffusivities  $D_{\text{He,Ar}}$  are at total pressures of 0.1 MPa. (b) Influence of total system pressure on the bulk diffusivities  $D_{\text{He,Ar}}$ .

Figure S3. (a) Experimental data (shown by symbols) of Remick and Geankoplis<sup>14</sup> for the fluxes of helium (1), neon (2) and argon (3) across a porous capillary diffusion cell made up of cylindrical capillaries of diameter  $d_p = 39.1 \mu\text{m}$ , and length  $\delta = 9.6 \text{ mm}$ . The fluxes are plotted as a function of the average system pressure. The continuous solid lines are the calculations using the linearized equation (15). The matrix  $[B]$  is evaluated at the average composition at either ends of the capillaries at the average system pressure. (b) Calculations of the fluxes as a function of the capillary diameter, maintaining the total pressure =  $10^3 \text{ Pa}$ .

Figure S4. Unary  $\text{CO}_2$  permeation fluxes across Vycor glass membrane at (a) 293 K, and (b) 343 K with calculations using the combination of the DGM model, both including and neglecting surface diffusion. The input data are provided in Table S1.

Figure S5. (a) MD data on the Maxwell-Stefan diffusivity  $D_{12}$ , for equimolar ( $c_1 = c_2$ ) binary mixture of CH<sub>4</sub>-Ar in silica pores with diameters in the range 2 nm to 10 nm. Also shown (square symbols) are the  $D_{12,fl}$  data for binary fluid CH<sub>4</sub>-Ar mixture diffusion, obtained from independent MD simulations. (b, c, d, e) MD data on the Maxwell-Stefan diffusivity for equimolar ( $c_1 = c_2$ ) binary mixtures (b) CO<sub>2</sub>- CH<sub>4</sub>, (c) CH<sub>4</sub>- H<sub>2</sub>, (d) CO<sub>2</sub>- H<sub>2</sub>, and (e) Ar- H<sub>2</sub> in BTP-COF compared with the corresponding values of the  $D_{12,fl}$  data for binary fluid mixture diffusion, obtained from independent MD simulations. The straight line represents the estimations of the gas phase diffusivity  $D_{12,fl}$  using the Fuller-Schettler-Giddings method.<sup>2, 3</sup>

Figure S6. (a) MD data of Krishna and van Baten<sup>23</sup> on the M-S diffusivity  $D_i$  for various guest molecules (hydrogen, argon, carbon dioxide, methane, ethane, propane) in BTP-COF, plotted as function of the pore concentration,  $c_i$ . (b) Ratio of the MD data of Krishna and van Baten<sup>23</sup> on the zero-loading diffusivity to the calculated Knudsen diffusivity,  $D_i(0)/D_{i,Kn}$ , for various guest molecules for various guest molecules (H<sub>2</sub>, Ar, CH<sub>4</sub>, C<sub>2</sub>H<sub>6</sub>, C<sub>3</sub>H<sub>8</sub>, nC<sub>4</sub>H<sub>10</sub>, nC<sub>5</sub>H<sub>12</sub>, nC<sub>6</sub>H<sub>14</sub>) in BTP-COF, plotted as function of the Henry coefficient for adsorption of the corresponding species. (c) Ratio of the MD data of Krishna and van Baten<sup>15, 16, 23</sup> on the zero-loading diffusivity to the calculated Knudsen diffusivity,  $D_i(0)/D_{i,Kn}$ , for linear alkanes as a function of C number in BTP-COF, 2 nm cylindrical silica pore, and 3 nm cylindrical pore.

Figure S7. MD data of M-S diffusivity at zero-loading,  $D_i$ , of (a) CH<sub>4</sub>, (b) Ar, (c) CO<sub>2</sub>, and (c) C<sub>3</sub>H<sub>8</sub> in zeolites, MOFs, and silica mesopores, plotted as a function of the pore dimension. The data has been culled from various MD simulation data sources.<sup>15-17</sup>

Figure S8. The two-bulb diffusion experiment of Duncan and Toor<sup>25</sup> with H<sub>2</sub>(1)/N<sub>2</sub>(2)/CO<sub>2</sub>(3) gas mixture.

Figure S9. (a) Experimental data of Duncan and Toor<sup>25</sup> on the transient approach to equilibrium in the two-bulb diffusion experiments for H<sub>2</sub>(1)/N<sub>2</sub>(2)/CO<sub>2</sub>(3) mixtures. (b) Equilibration trajectories in composition space, followed in the two bulbs. The calculations using the Maxwell-Stefan diffusion equations, ignoring molecule-pore wall collisions are shown by the continuous solid lines (for Bulb A) and dashed lines (for Bulb B).

Figure S10. (a) Partial pressures of each component, and (b) total pressure in Bulb A and Bulb B for 200 nm capillary tube joining A and B.

Figure S11. (a) Partial pressures of each component, and (b) total pressure in Bulb A and Bulb B for 2 nm capillary tube joining A and B.

Figure S12. Component partial pressure profiles, along the distance of the 200 nm capillary tube. These profiles are for time,  $t = 10$  h from the start. The position  $z = 0$  corresponds to the center point between the two semi-infinite slabs.

Figure S13. Schematic showing the two-compartment membrane set-up used in the experiments reported by Tuchlenski et al.,<sup>9</sup> Yang et al.<sup>27</sup> and Veldsink et al.<sup>28</sup>

Figure S14. Experimental data of Tuchlenski et al.<sup>9</sup> for the dynamic pressure increase in the downstream compartment (data scanned from Figure 5 of Tuchlenski paper) for He-Ar mixtures at 293 K. The continuous solid lines are the calculations using the DGM equation (5). Input data in Table S2.

Figure S15. Experimental data of Yang et al.<sup>27</sup> for the dynamic pressure increase in the downstream compartment (data scanned from Figure 4 of Yang paper) for He-N<sub>2</sub> mixtures at 293 K. The continuous solid lines are the calculations using the DGM equation (5). Input data in Table S3.

Figure S16. Experimental data of Veldsink et al.<sup>28</sup> for the dynamic pressure increase in the downstream compartment (data scanned from Figure 9 and Figure 11 of Veldsink paper) for (a) He-Ar mixtures at 293 K, and (b) He-N<sub>2</sub> mixtures at 298 K. The continuous solid lines are the calculations using the DGM equation (5). Input data in Table S4.

Figure S17. Transient uptake of He-Ar mixtures at 293 K in a spherical adsorbent particle of diameter 4 mm. Initially, the partial pressures of He, and Ar are  $p_{10} = 0$  kPa,  $p_{20} = 100$  kPa, respectively. At time  $t = 0$ , the external surface is maintained at  $p_{1,\text{eq}} = 100$  kPa,  $p_{2,\text{eq}} = 0$  kPa. The time-evolution of the partial pressures, and total pressures are shown. The continuous solid lines are the calculations using the DGM equation (5). Input data in Table S2.



Figure S18. Transient uptake inside particle made of mesoporous Vycor glass exposed to a gas phase He<sub>2</sub>(1)/N<sub>2</sub>(2) mixture at 293 K. Initially, the particle is equilibrated with partial pressures are  $p_1 = 50$  kPa;  $p_2 = 50$  kPa. For times,  $t \geq 0$ , the partial pressures of the components in the bulk gas phase are maintained at  $p_1 = 100$  kPa;  $p_2 = 0$  kPa. The structural data are provided in Table S3.

Figure S19. Experimental data of Tuchlenski et al.<sup>9</sup> for the dynamic pressure increase in the downstream compartment (data scanned from Figure 7a and Figure 7b of Tuchlenski paper) for (a) He-CO<sub>2</sub> mixtures at 293 K, and (b) He-CO<sub>2</sub> mixtures at 343 K. The continuous solid lines are the calculations using the DGM equation (5). The dashed lines are the calculations using the M-S equation (25), taking  $D_{He} = D_{He,Kn}$  and  $D_{CO_2} = 0.55D_{CO_2,Kn}$  in (a)  $D_{He} = D_{He,Kn}$  and  $D_{CO_2} = 0.7D_{CO_2,Kn}$  in (b). Input data in Table S2.

Figure S20. Experimental data of Tuchlenski et al.<sup>9</sup> for the dynamic pressure increase in the downstream compartment (data scanned from Figure 7c and Figure 7d of Tuchlenski paper) for (a) He-C<sub>3</sub>H<sub>8</sub> mixtures at 293 K, and (b) He-C<sub>3</sub>H<sub>8</sub> mixtures at 343 K. The continuous solid lines are the calculations using the DGM equation (5). The dashed lines are the calculations using the M-S equation (25), taking  $D_{He} = D_{He,Kn}$  and  $D_{C_3H_8} = 0.78D_{C_3H_8,Kn}$  in (a)  $D_{He} = D_{He,Kn}$  and  $D_{C_3H_8} = 0.87D_{C_3H_8,Kn}$  in (b). Input data in Table S2.

Figure S21. Experimental data of Tuchlenski et al.<sup>9</sup> for the dynamic pressure increase in the downstream compartment (data scanned from Figure 10 of Tuchlenski paper) for CO<sub>2</sub>-C<sub>3</sub>H<sub>8</sub> mixtures at 293 K. The continuous solid lines are the calculations using the DGM equation (5). The dashed lines are

the calculations using the M-S equation (25), taking  $D_{CO_2} = 0.55D_{CO_2,Kn}$  and  $D_{C_3H_8} = 0.78D_{C_3H_8,Kn}$ .

Input data in Table S2.

Figure S22. Experimental data of Tuchlenski et al.<sup>9</sup> for the dynamic pressure increase in the downstream compartment, initially filled with CO<sub>2</sub>, for CO<sub>2</sub>-C<sub>3</sub>H<sub>8</sub> mixtures at 293 K. Comparison with M-S model calculations taking  $D_{C_3H_8} = 0.78D_{C_3H_8,Kn}$ , along with different values of  $D_{CO_2}$  as specified in the Figure 22.

Figure S23. (a) Comparing the transmembrane fluxes calculated by the DGM (continuous solid lines) and Maxwell-Stefan (dashed lines) models for the Tuchlenski experiments for CO<sub>2</sub>-C<sub>3</sub>H<sub>8</sub> mixtures at 293 K in which the downstream compartment is initially filled with CO<sub>2</sub>, and the upstream compartment is maintained at constant composition with a 1:1 CO<sub>2</sub>-C<sub>3</sub>H<sub>8</sub> mixture at 10<sup>5</sup> Pa. (b) Calculations of the component permeances  $\Pi_i$  using the DGM and M-S model calculations.

Figure S24. Experimental data of Yang et al.<sup>27</sup> for the dynamic pressure increase in the downstream compartment (data scanned from Figure 5 of Yang paper) for He-CO<sub>2</sub> mixtures at 293 K. The continuous solid lines are the calculations using the DGM equation (5). The dashed lines are the calculations using the M-S equation (25), taking  $D_{He} = D_{He,Kn}$  and  $D_{CO_2} = 0.55D_{CO_2,Kn}$ . Input data in Table S3.

Figure S25. Experimental data of Yang et al.<sup>27</sup> for the dynamic pressure increase in the downstream compartment (data scanned from Figure 6 of Yang paper) for CO<sub>2</sub>-C<sub>3</sub>H<sub>8</sub> mixtures at 293 K. The continuous solid lines are the calculations using the DGM equation (5). The dashed lines are the calculations using the M-S equation (25), taking  $D_{CO_2} = 0.55D_{CO_2,Kn}$  and  $D_{C_3H_8} = 0.88D_{C_3H_8,Kn}$ . Input data in Table S3.

Figure S26. (a) Comparing the transmembrane fluxes calculated by the DGM (continuous solid lines) and Maxwell-Stefan (dashed lines) models for the Yang experiments for CO<sub>2</sub>-C<sub>3</sub>H<sub>8</sub> mixtures at 293 K in which the downstream compartment is initially filled with CO<sub>2</sub>, and the upstream compartment is flushed with pure C<sub>3</sub>H<sub>8</sub> at 10<sup>5</sup> Pa. (b) Calculations of the component permeances  $\Pi_i$  using the DGM and M-S model calculations.

Figure S27. Ratio  $D_i/D_{i,Kn}$ , obtained from the simulations of Tuchlenski and Yang experiments plotted as a function of the Henry coefficient for adsorption. The Henry coefficient is determined from the Langmuir constants for the unary isotherms as reported in Table 2 of Tuchlenski et al.<sup>9</sup> and Table 1 of Yang et al.<sup>27</sup> The Henry coefficients are calculated as the product of the saturation capacity,  $c_{i,sat}$  (units: mol m<sup>-3</sup>), and the Langmuir constant,  $b_i$  (units: Pa<sup>-1</sup>), divided by the skeletal density,  $\rho$  (= 2057 kg m<sup>-3</sup>).

Please note that the isotherm data reported by Tuchlenski and Yang use  $c_i$  defined in terms of mol of species  $i$  per m<sup>3</sup> of solid material; for this reason we use the skeletal density in the calculation of the Henry constant.

Figure S28. Experimental data of Veldsink et al.<sup>28</sup> for the dynamic pressure increase in the downstream compartment (data scanned from Figure 12 and Figure 13 of Veldsink paper) for (a) He-CO<sub>2</sub> mixtures at

293 K, and (b) He-CO<sub>2</sub> mixtures at 434 K. The continuous solid lines are the calculations using the DGM equation (5). The dashed lines are the calculations using the M-S equation (25), taking  $D_{He} = D_{He,Kn}$  and  $D_{CO_2} = 0.85D_{CO_2,Kn}$  in (a) and  $D_{He} = D_{He,Kn}$  and  $D_{CO_2} = 0.9D_{CO_2,Kn}$  in (b). Input data in Table S4.

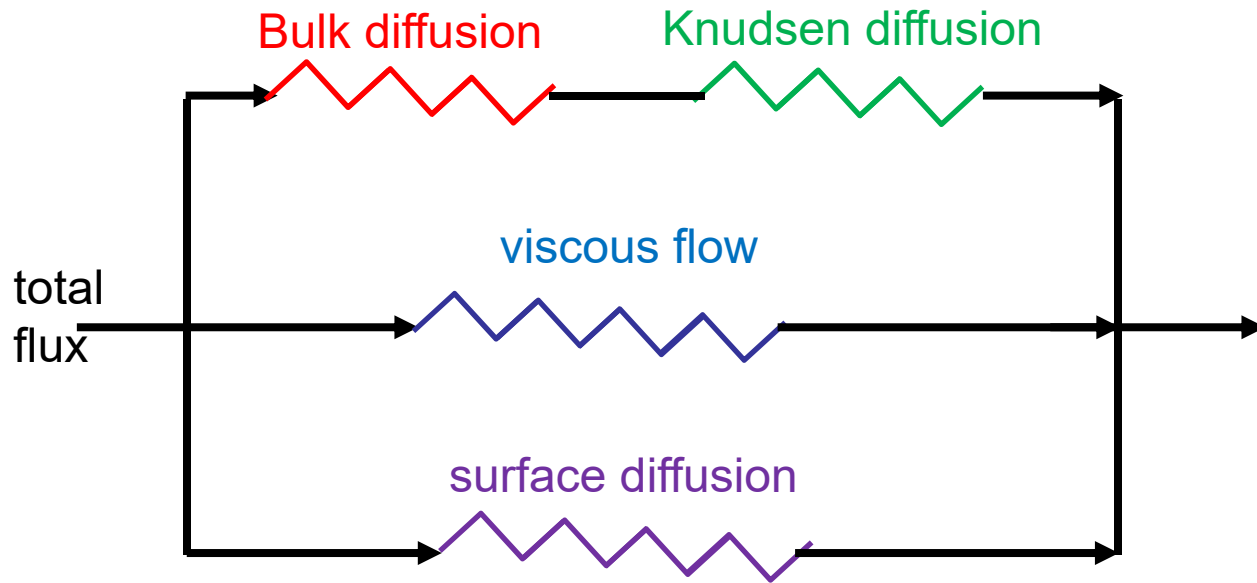
Figure S29. Experimental data of Veldsink et al.<sup>28</sup> for the dynamic pressure increase in the downstream compartment (data scanned from Figure 14 and Figure 15 of Veldsink paper) for (a) He-C<sub>3</sub>H<sub>8</sub> mixtures at 293 K, and (b) He-C<sub>3</sub>H<sub>8</sub> mixtures at 416 K. The continuous solid lines are the calculations using the DGM equation (5). The dashed lines are the calculations using the M-S equation (25), taking  $D_{He} = D_{He,Kn}$  and  $D_{C_3H_8} = 0.95D_{C_3H_8,Kn}$  in (a) and  $D_{He} = D_{He,Kn}$  and  $D_{C_3H_8} = 0.98D_{C_3H_8,Kn}$  in (b). Input data in Table S4.

Figure S30. Experimental data of Tuchlenski et al.<sup>9</sup> for the dynamic pressure increase in the downstream compartment for CO<sub>2</sub>-C<sub>3</sub>H<sub>8</sub> mixtures at 293 K. Comparison of mesopore diffusion model with surface diffusion model.

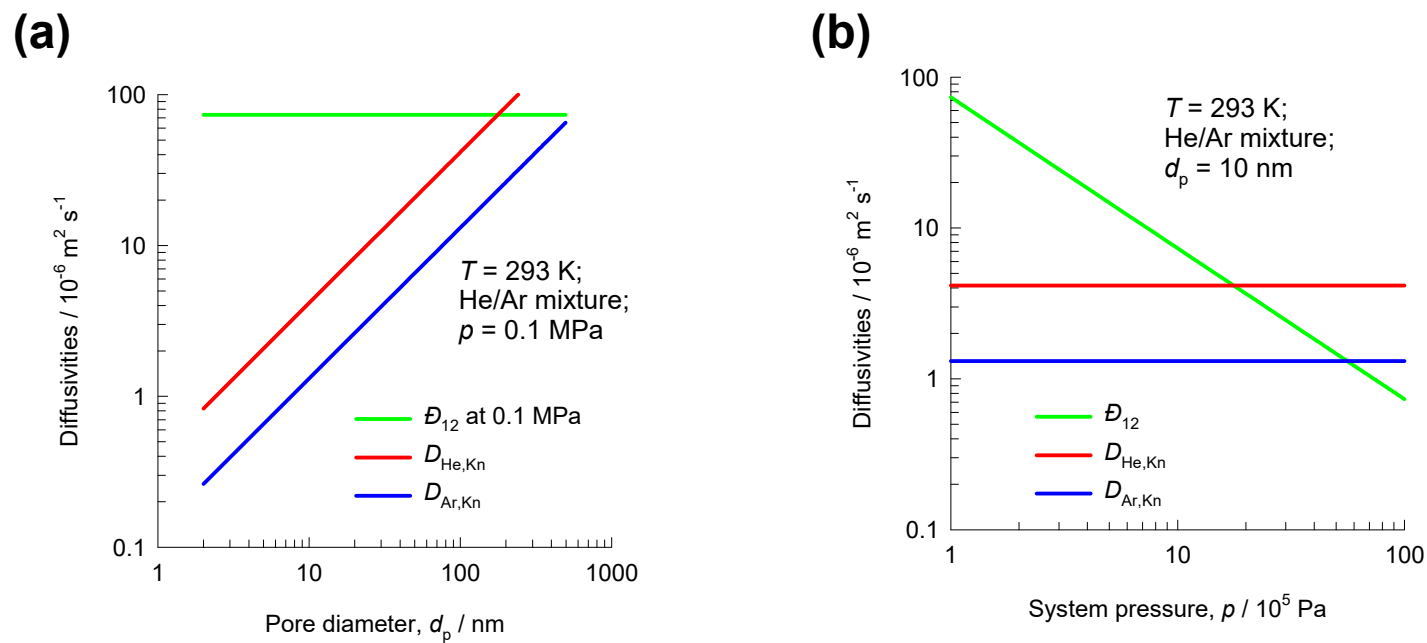
Figure S31. Experimental data of Yang et al.<sup>27</sup> for the dynamic pressure increase in the downstream compartment for CO<sub>2</sub>-C<sub>3</sub>H<sub>8</sub> mixtures (data scanned from Figure 6 of Yang paper) at 293 K. Comparison of mesopore diffusion model with surface diffusion model.

Figure S32. Experimental data of Yang et al.<sup>27</sup> for the dynamic pressure increase in the downstream compartment for CO<sub>2</sub>-C<sub>3</sub>H<sub>8</sub> mixtures (data scanned from Figure 7 of Yang paper) at 293 K. Comparison with surface diffusion model.

# The Dusty Gas Model

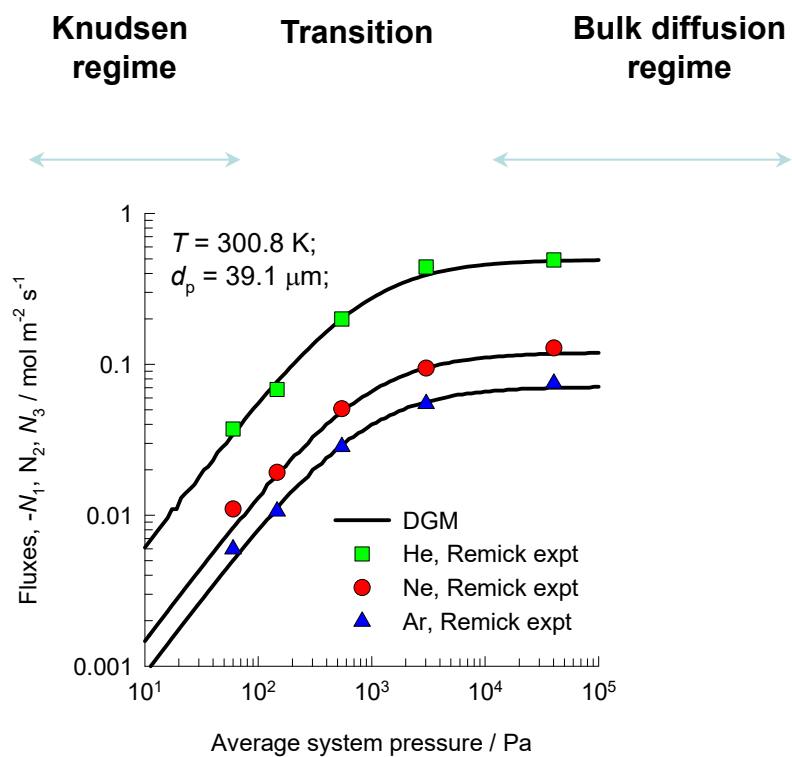


# Knudsen and bulk diffusivities

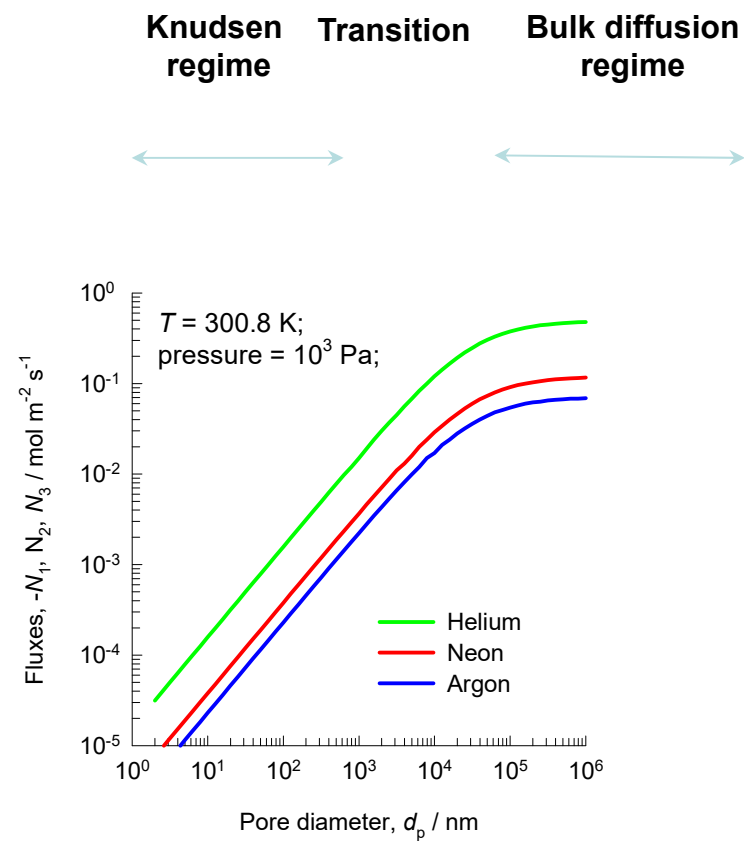


# Linearized DGM vs Remick Expt

(a)



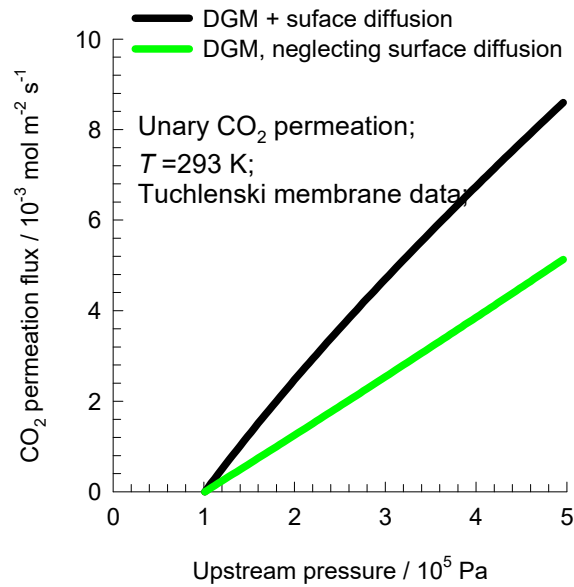
(b)





# Combining Knudsen, Viscous flow and Surface diffusion

(a)



(b)

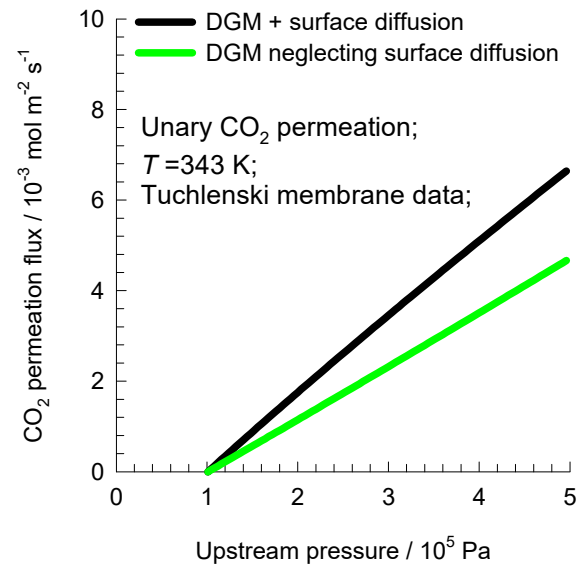


Figure S5

# Molecule-Molecule interactions

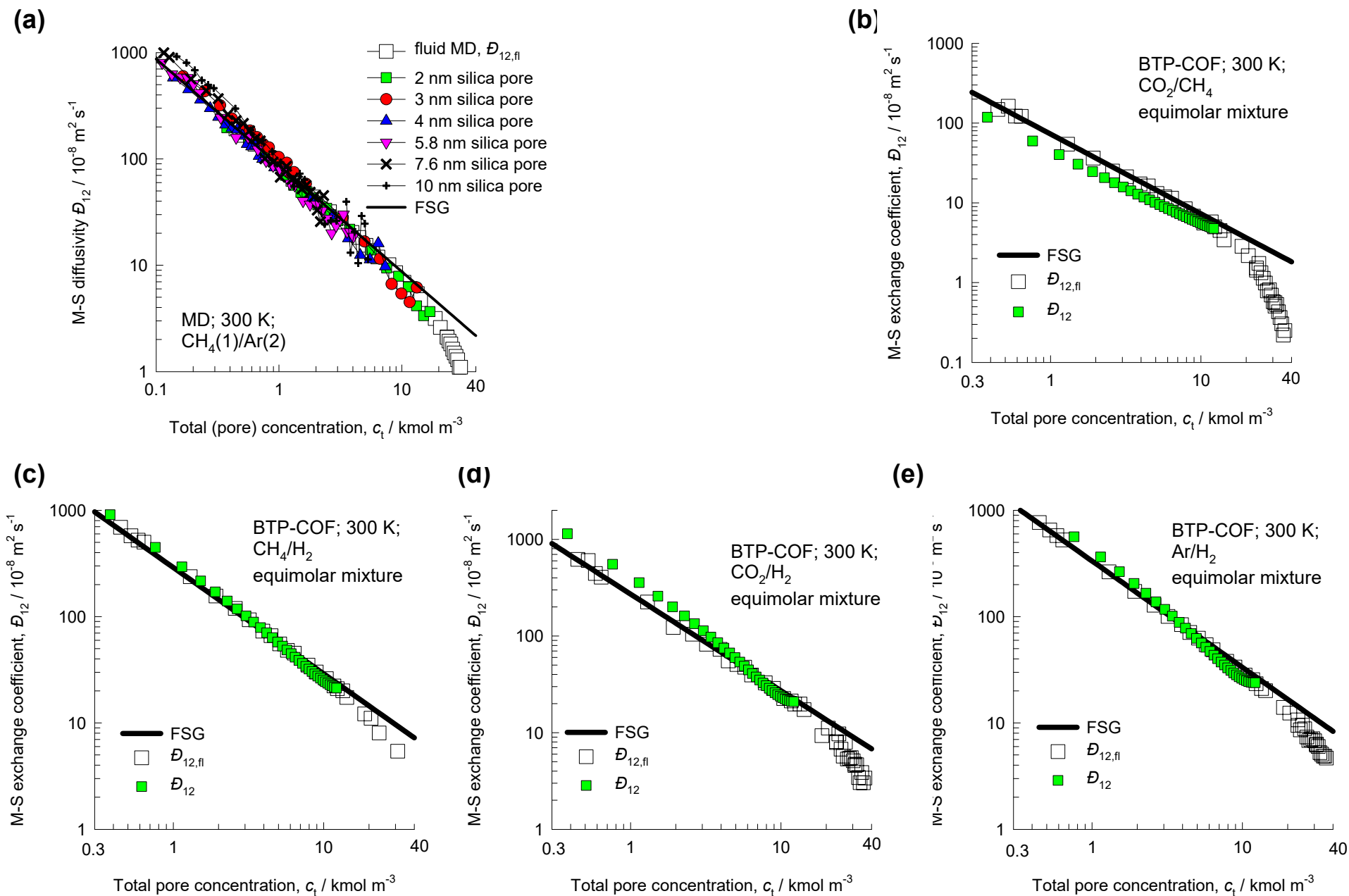
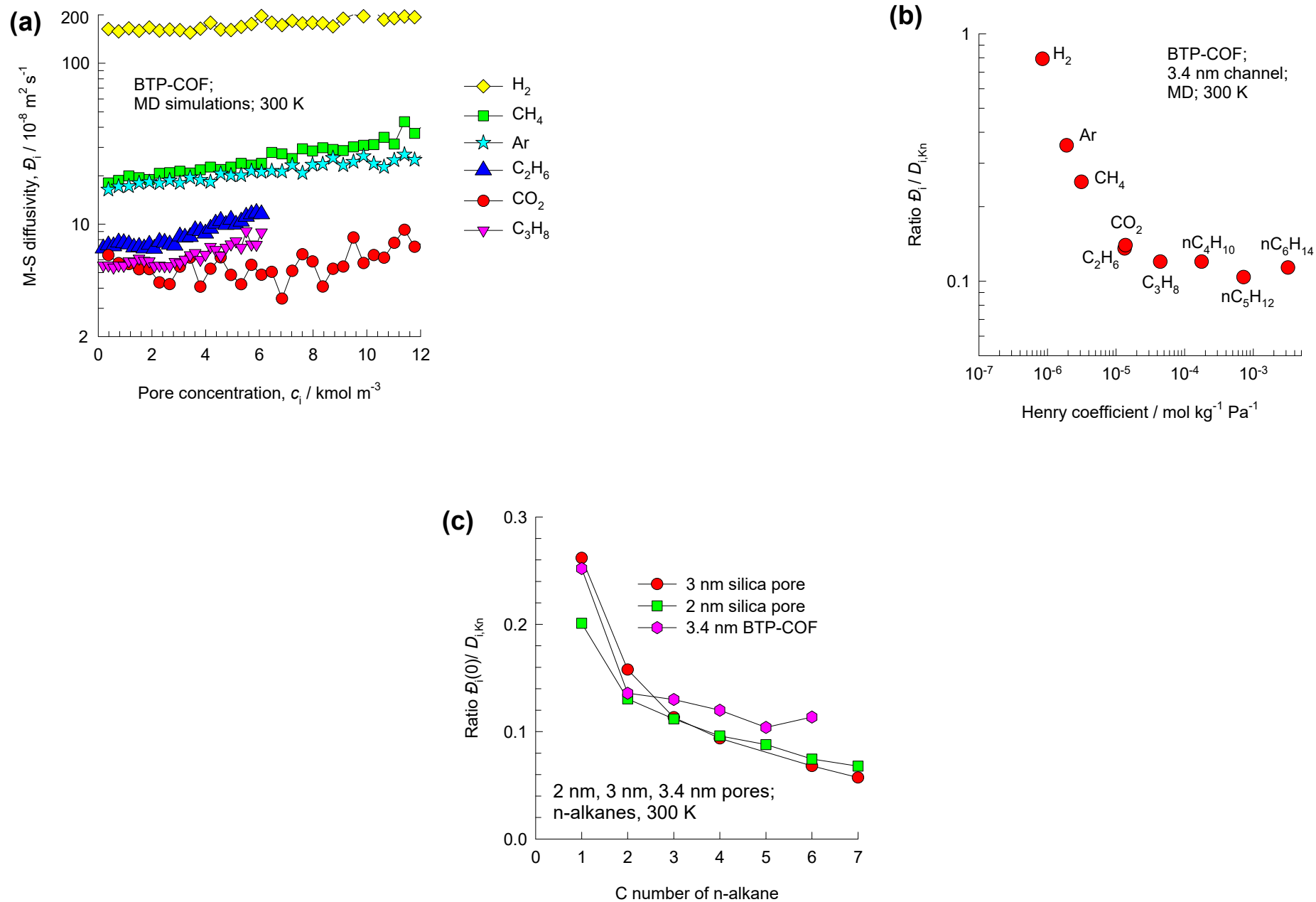
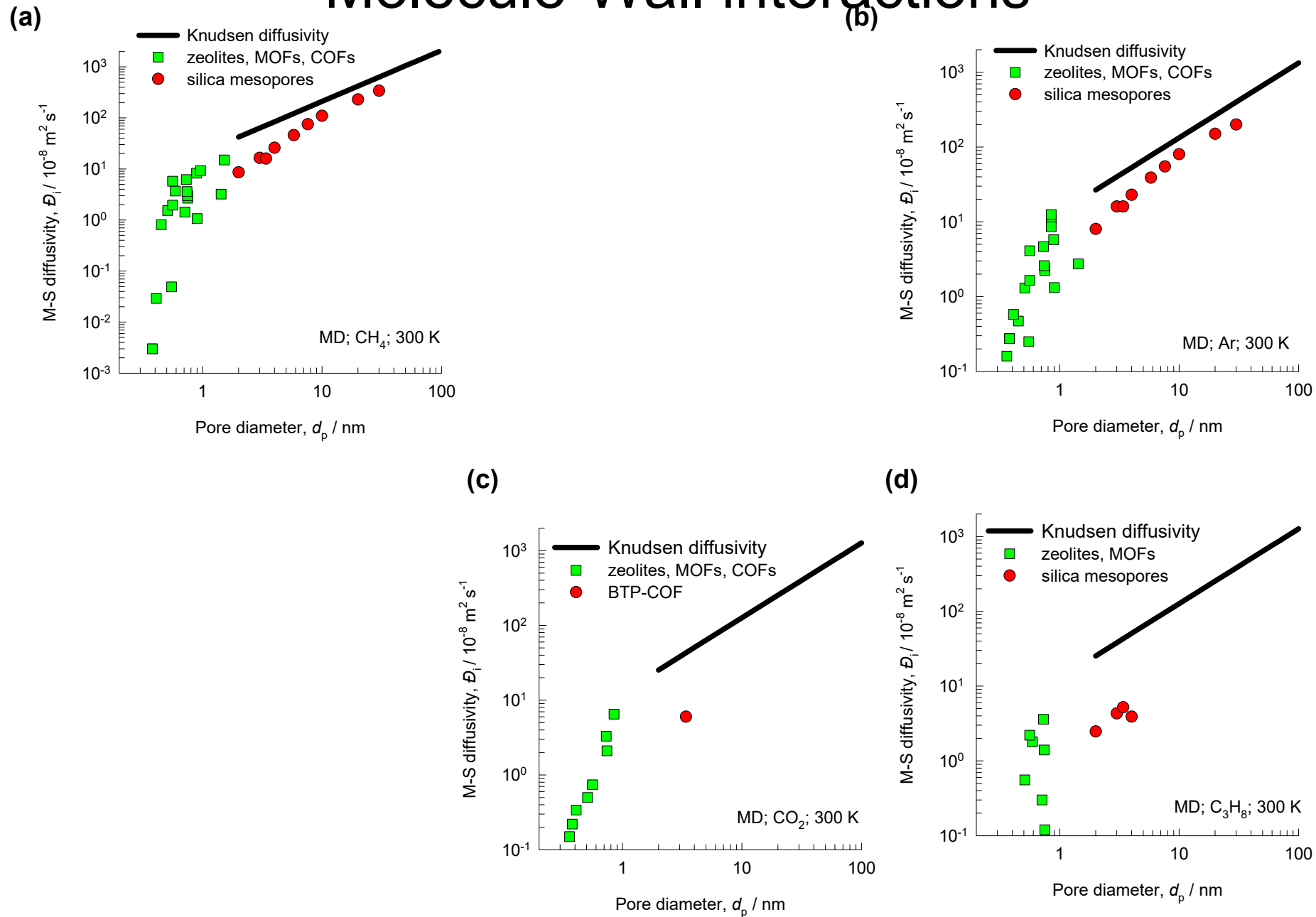


Figure S6

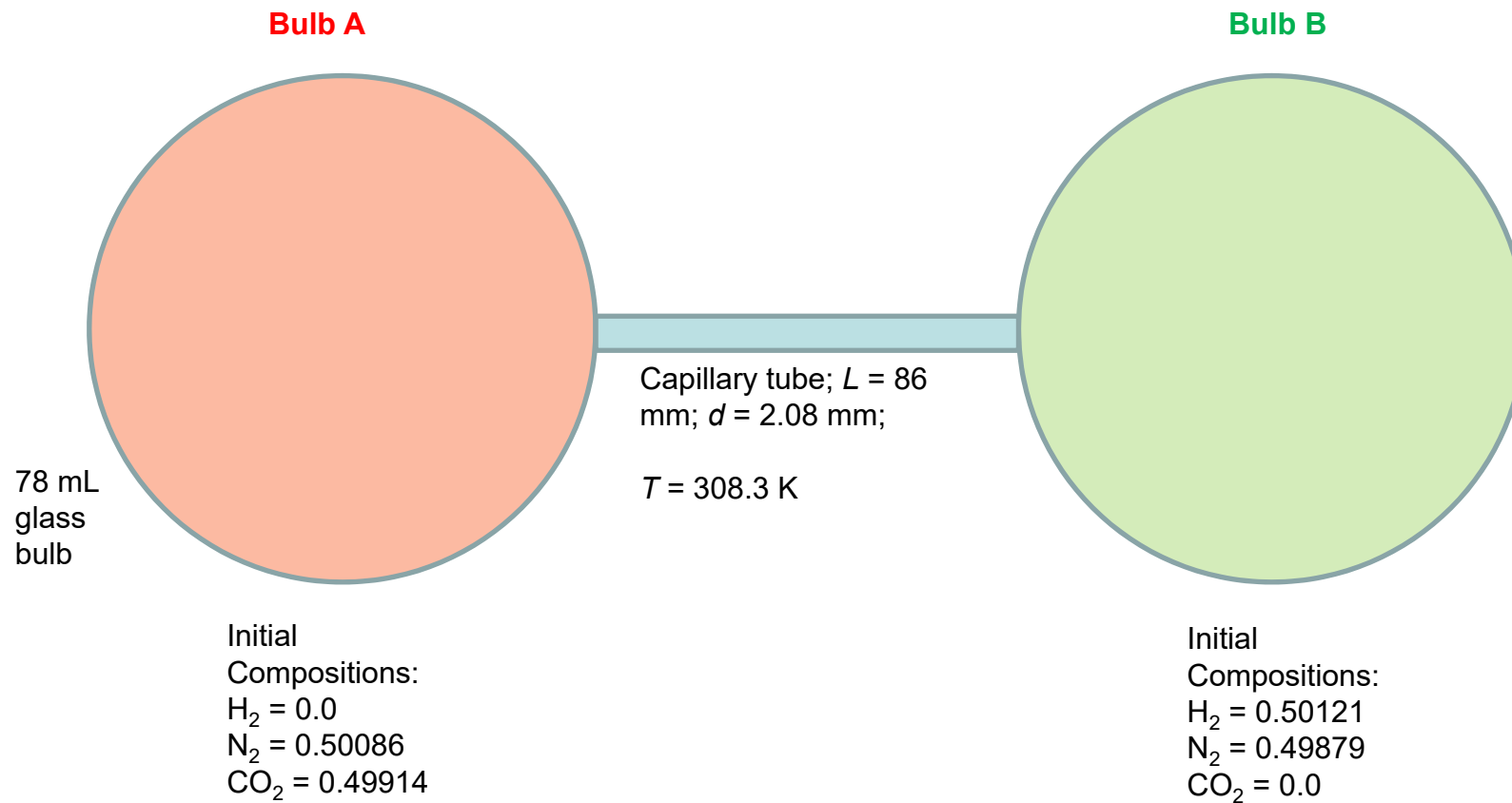
## Molecule-Wall interactions



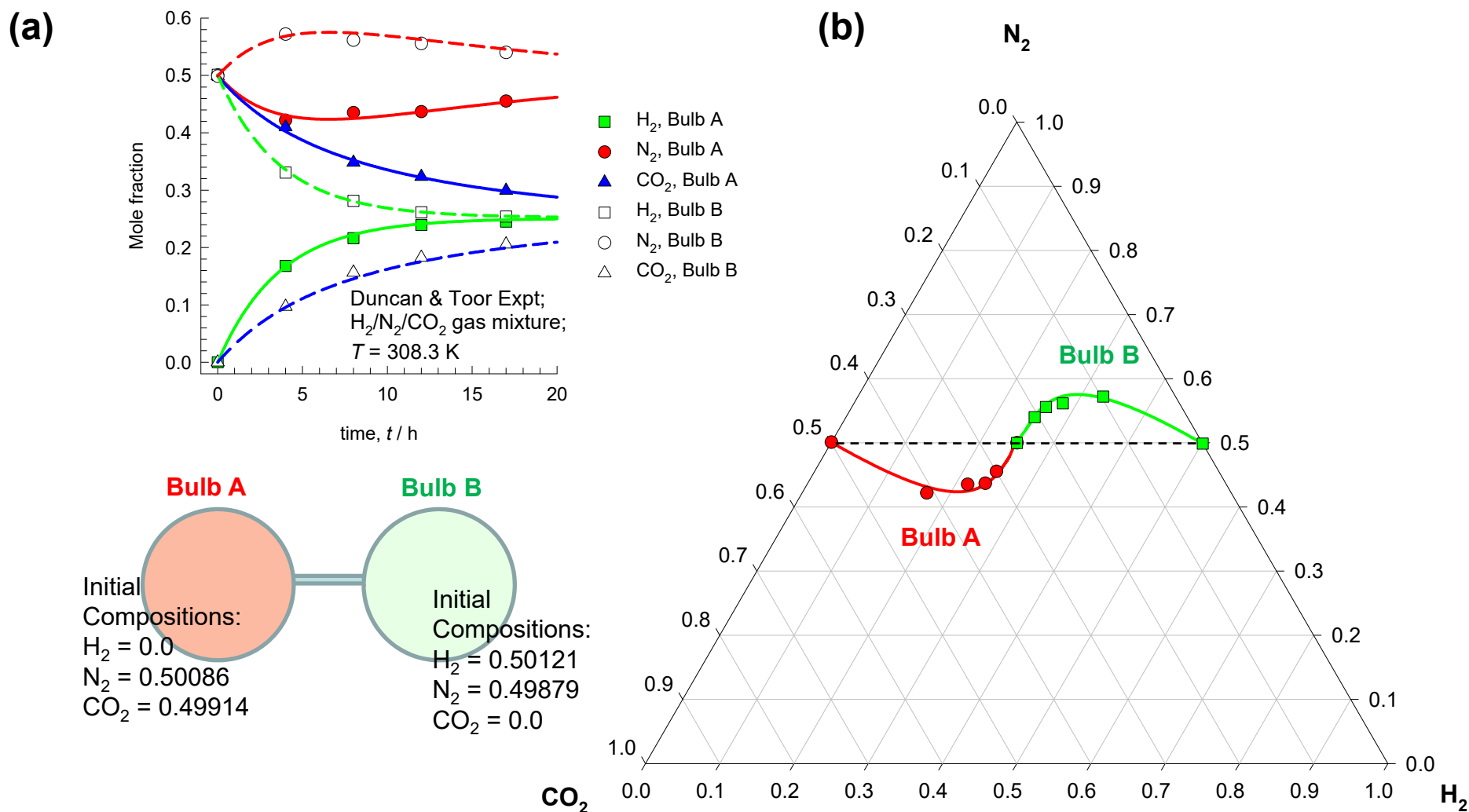
## Molecule-Wall interactions



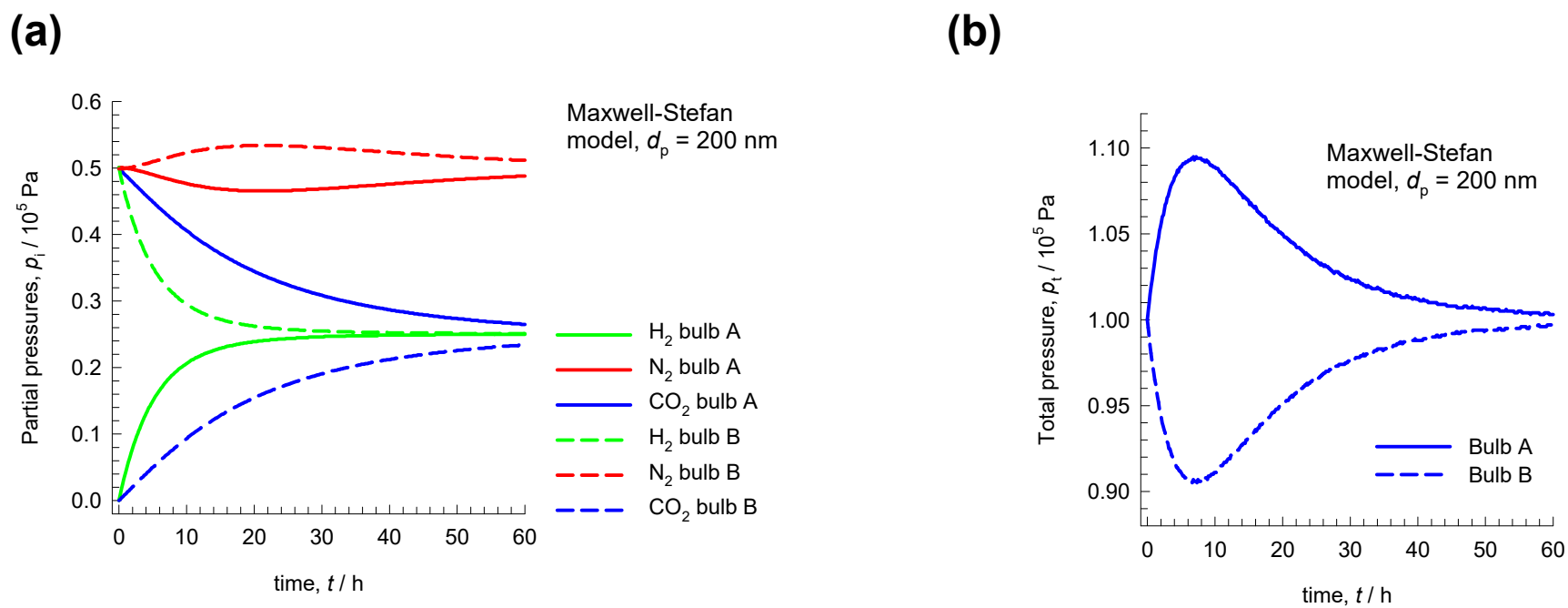
# H<sub>2</sub>/N<sub>2</sub>/CO<sub>2</sub> gas mixture diffusion



# H<sub>2</sub>/N<sub>2</sub>/CO<sub>2</sub> gas mixture diffusion



# H<sub>2</sub>/N<sub>2</sub>/CO<sub>2</sub> gas mixture diffusion



# H<sub>2</sub>/N<sub>2</sub>/CO<sub>2</sub> gas mixture diffusion

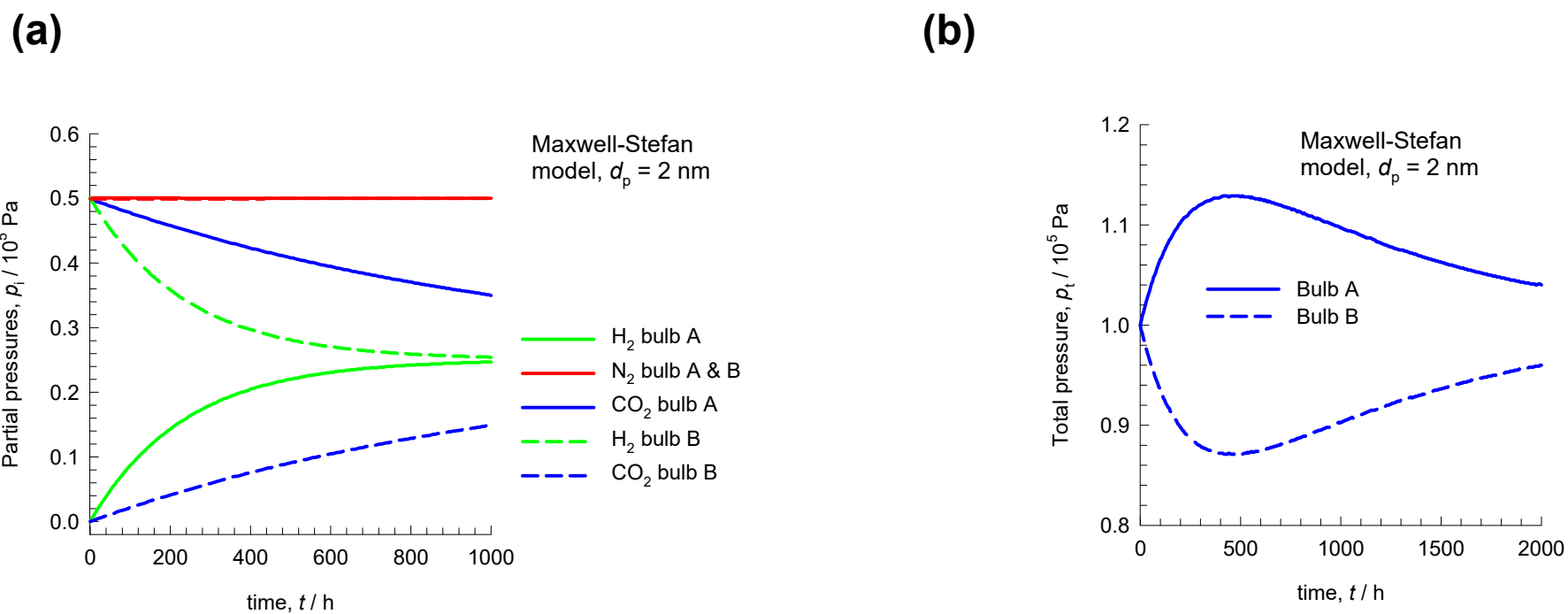
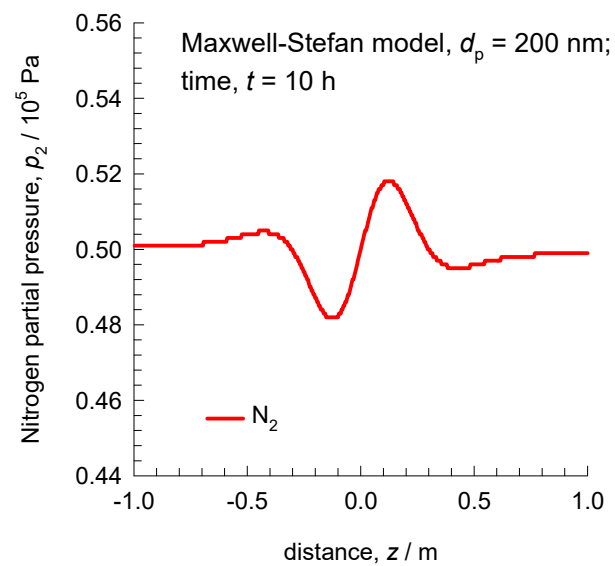
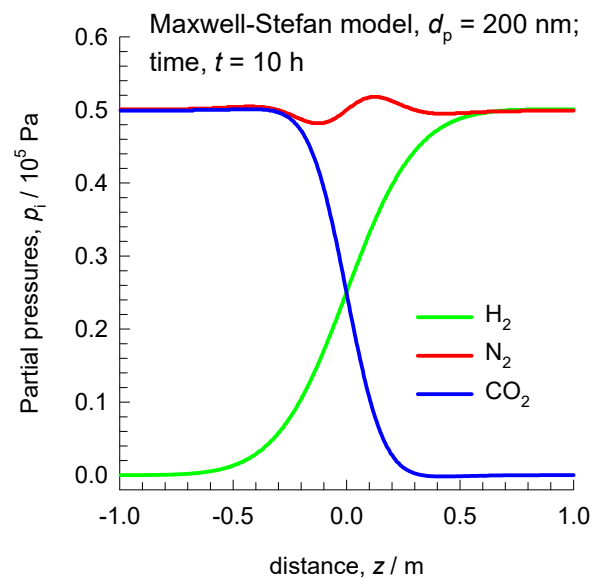


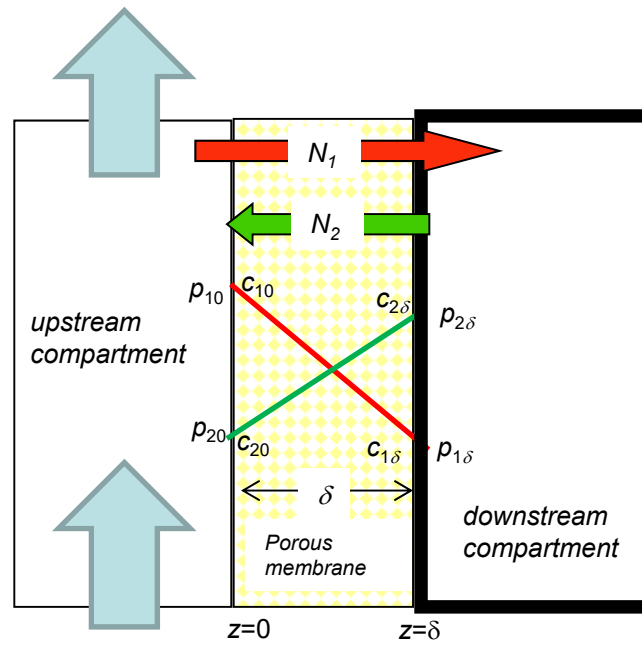


Figure S12

# H<sub>2</sub>/N<sub>2</sub>/CO<sub>2</sub> gas mixture diffusion

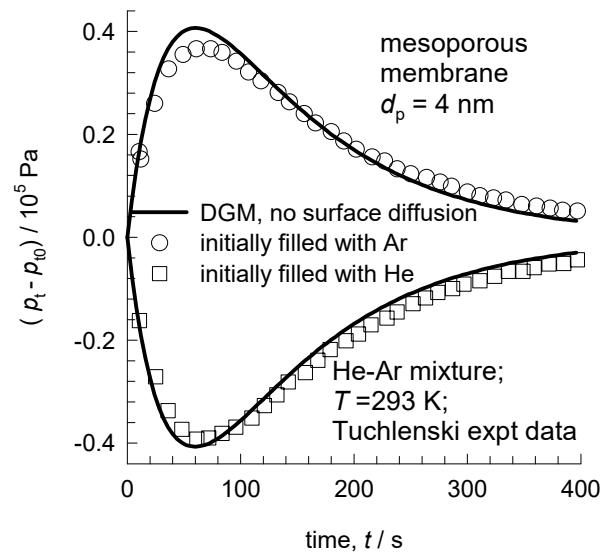


# Velsink, Tuchlenski, and Yang expt set-ups <sup>Figure S13</sup>

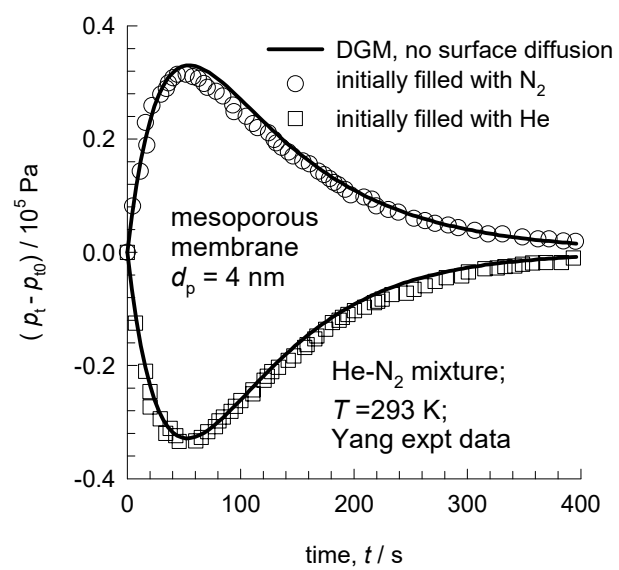


# Tuchlenski transient experiments

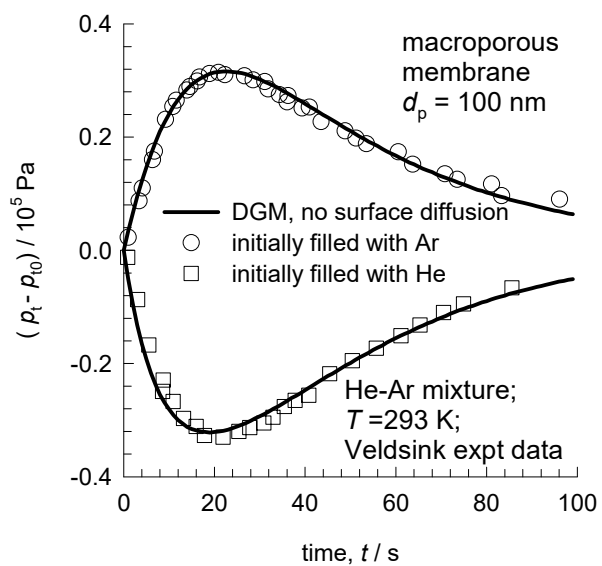
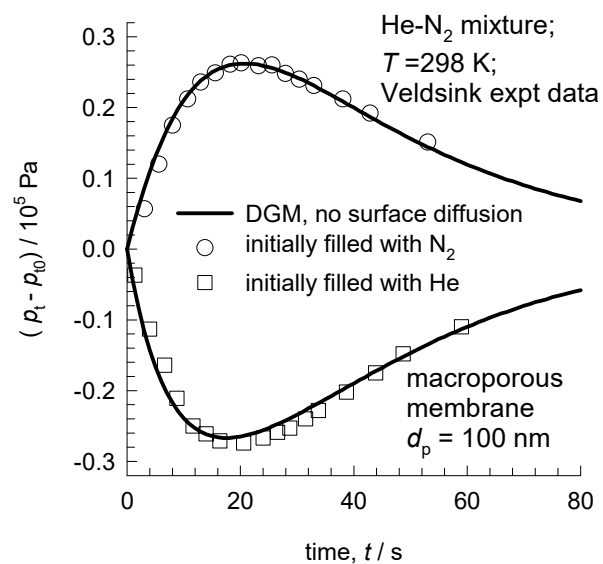
Figure S14



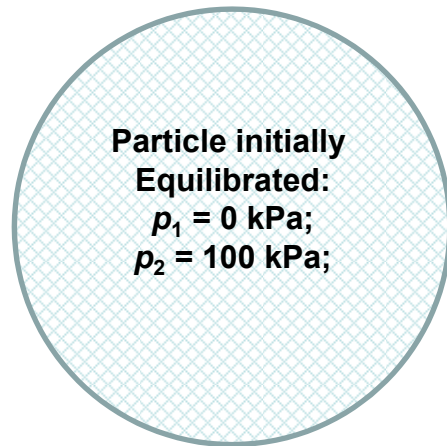
# Yang transient experiments



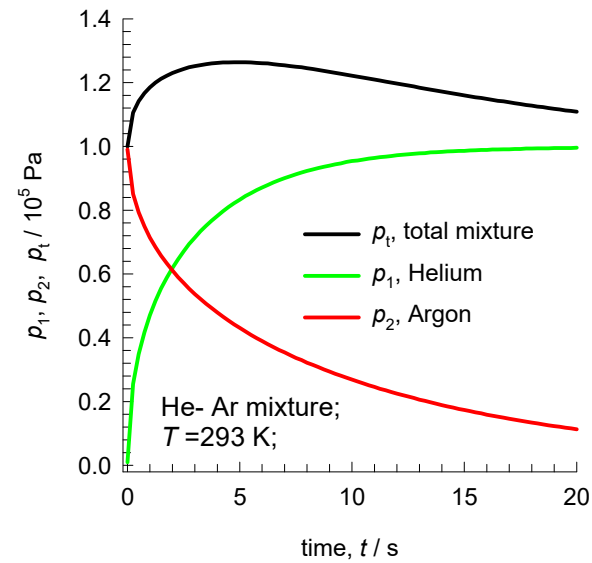
# Veldsink transient experiments

**(a)****(b)**

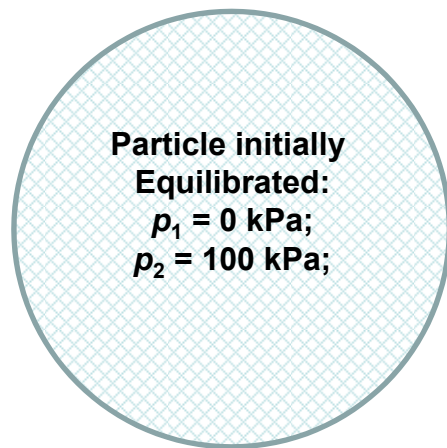
# Transient uptake inside particles



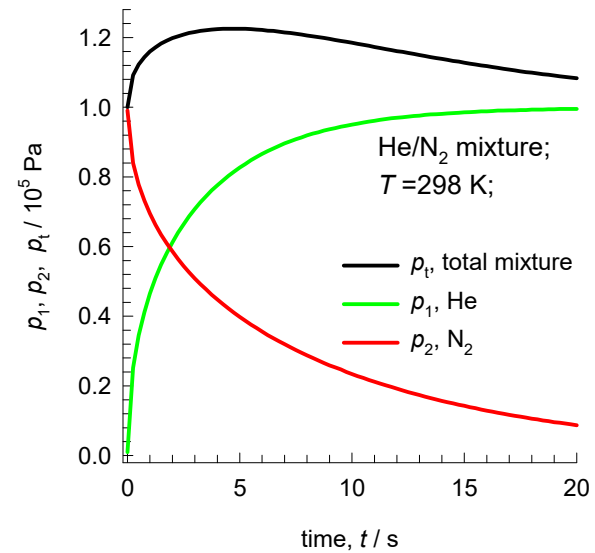
Bulk maintained at:  
 $p_1 = 100$  kPa;  
 $p_2 = 0$  kPa;



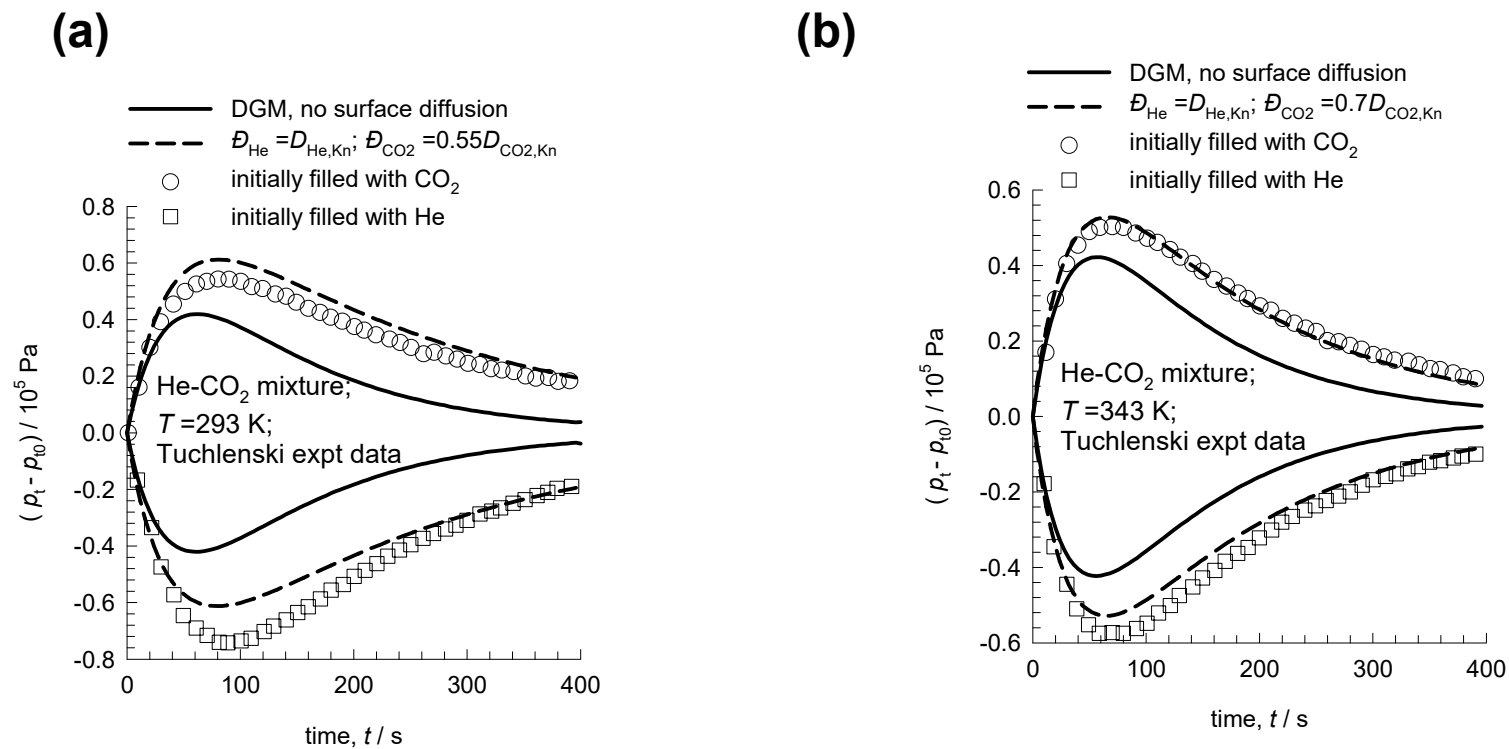
# Total pressure overshoot: mesoporous particle



Bulk maintained at:  
 $p_1 = 100$  kPa;  
 $p_2 = 0$  kPa;

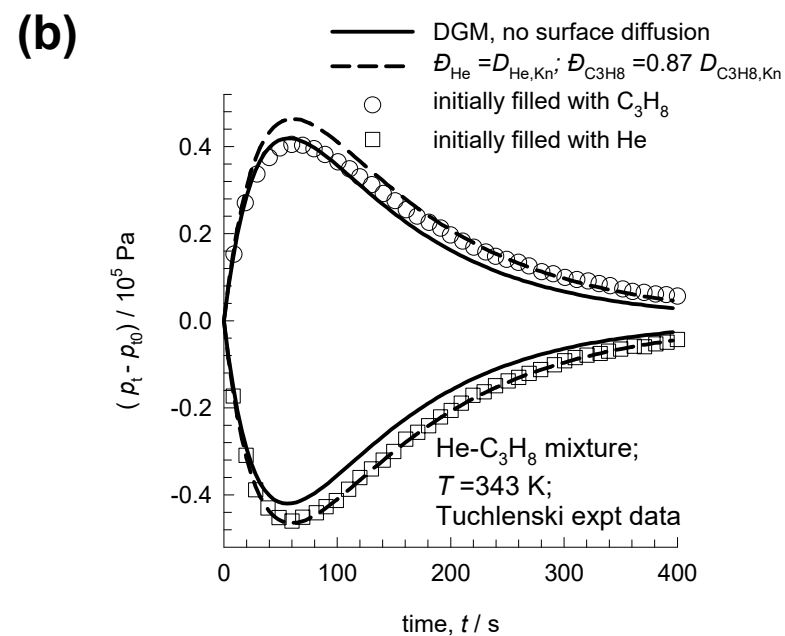
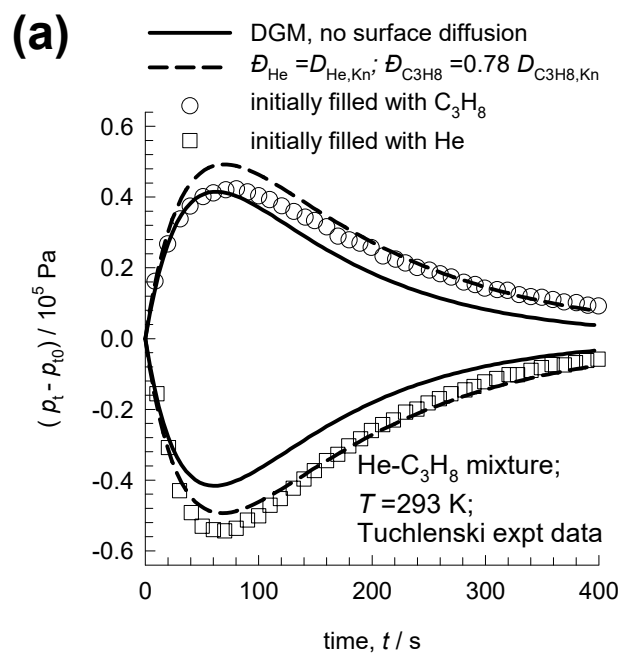


# Tuchlenski transient experiments



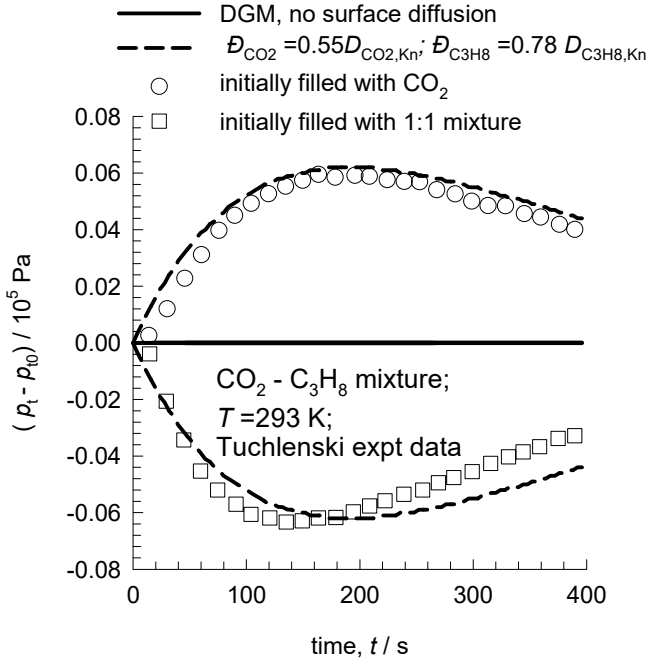


# Tuchlenski transient experiments



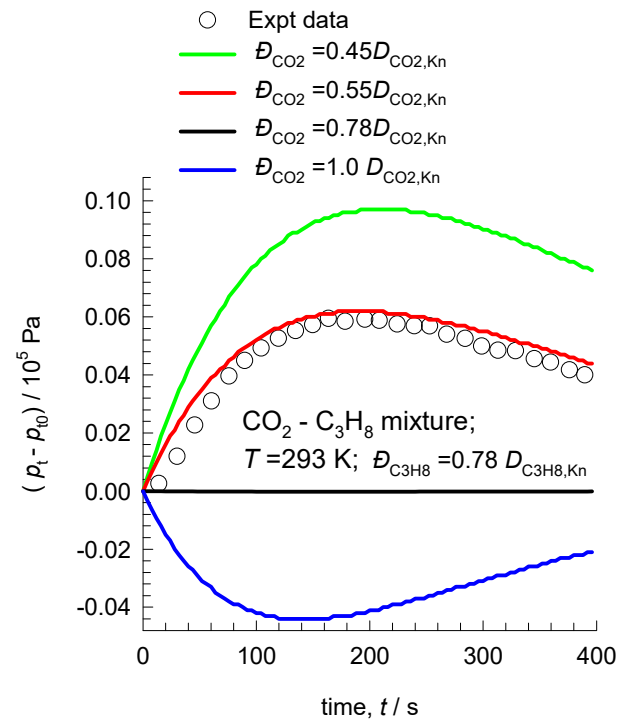
# Tuchlenski transient experiments

Figure S21

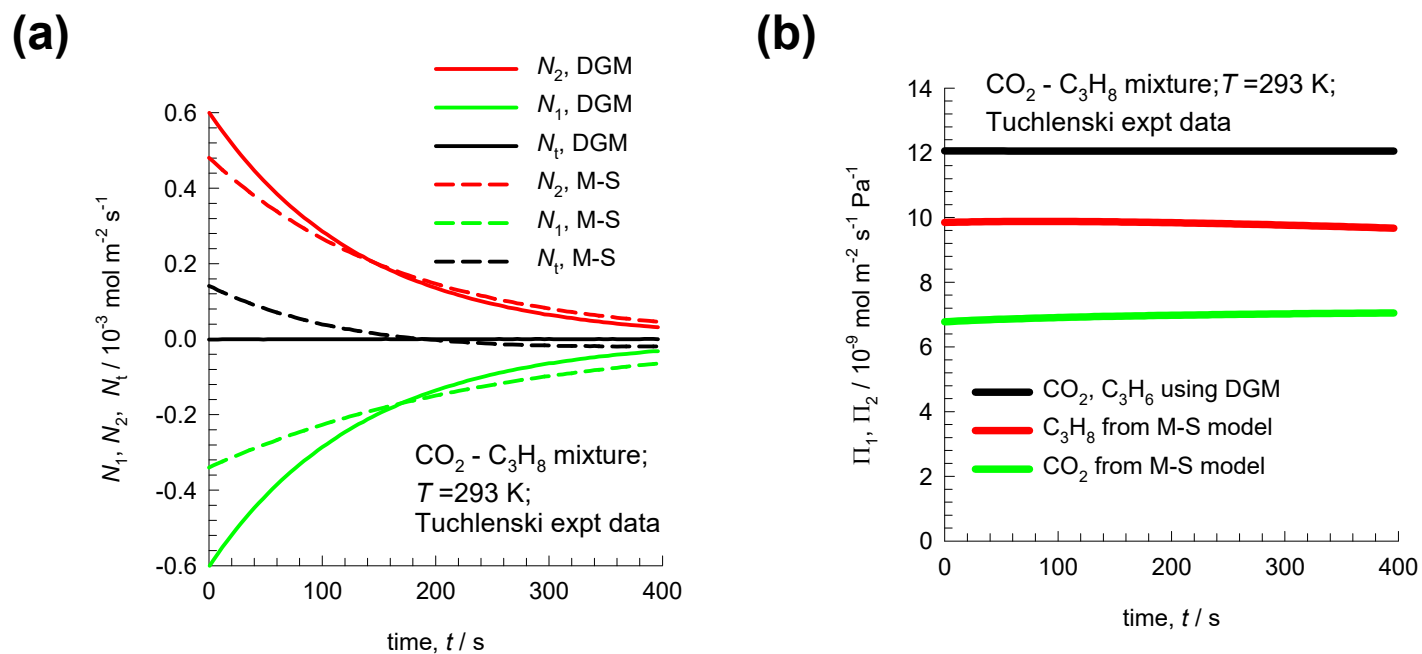


# Tuchlenski transient experiments

Figure S22

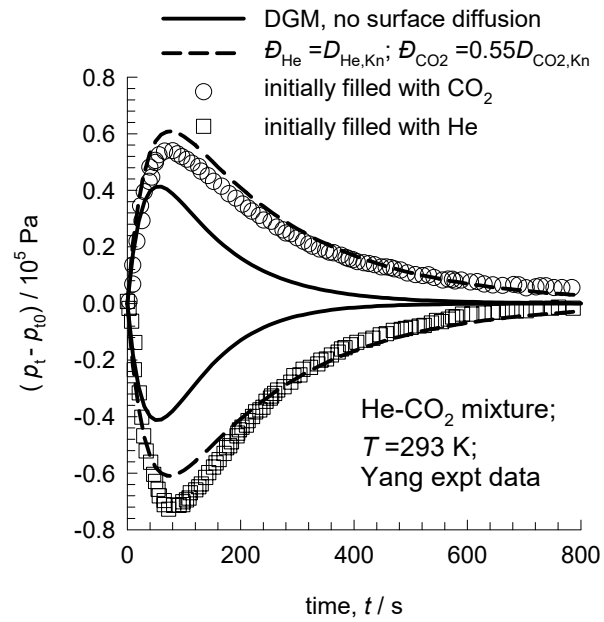


# Tuchlenski transient experiments



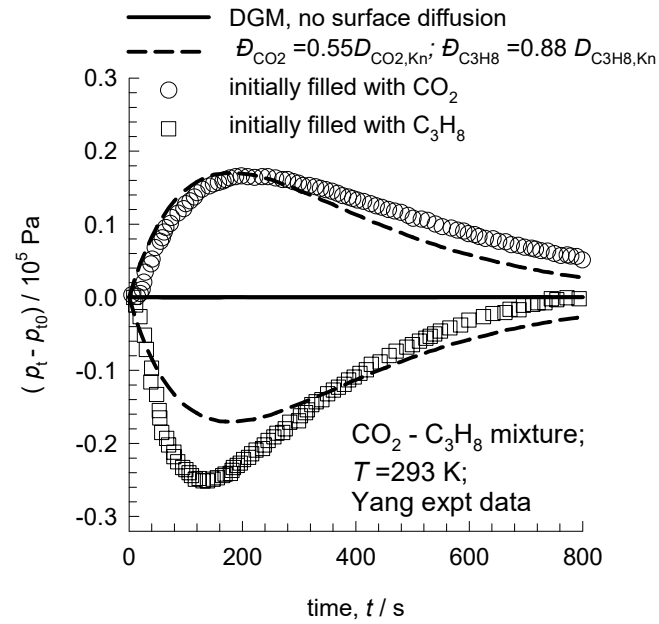
# Transient Yang experiments

Figure S24



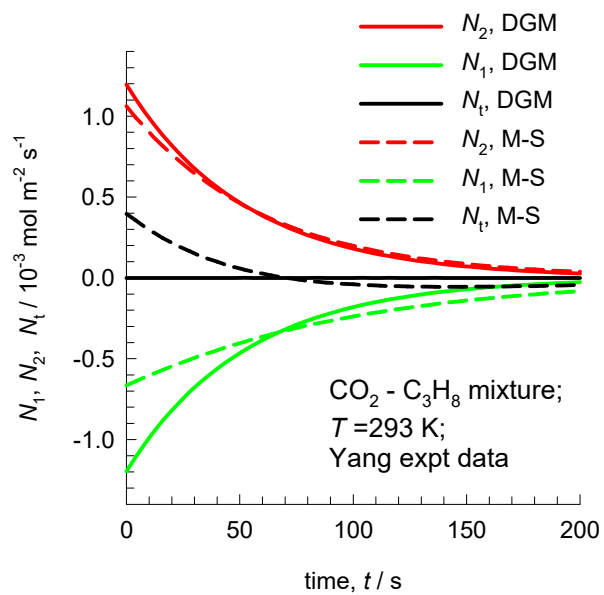
# Transient Yang experiments

Figure S25

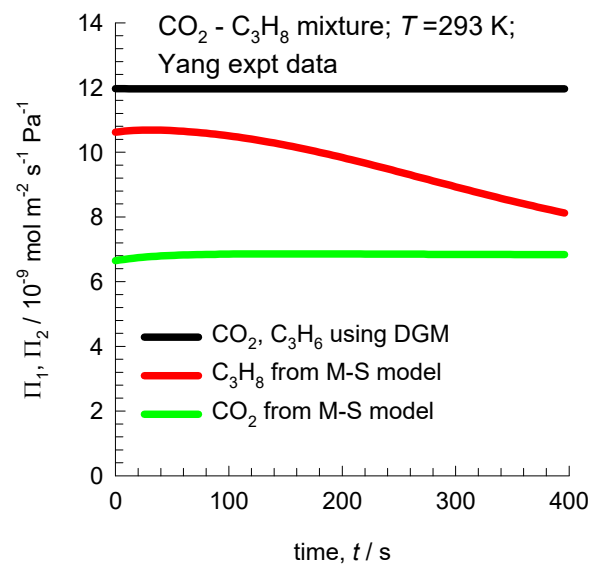


# Transient Yang experiments

(a)

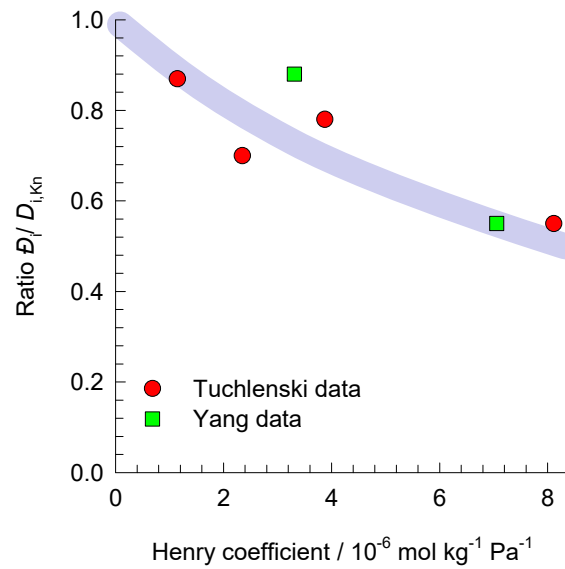


(b)



# Influence of adsorption on molecule-wall interactions

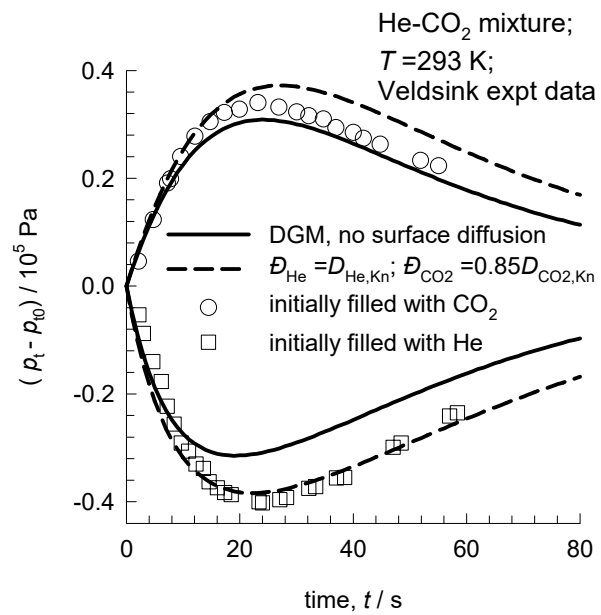
Figure S27



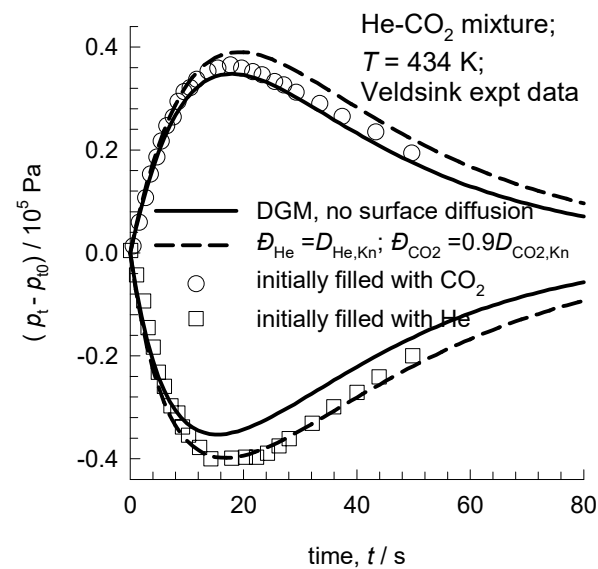


# Veldsink transient experiments

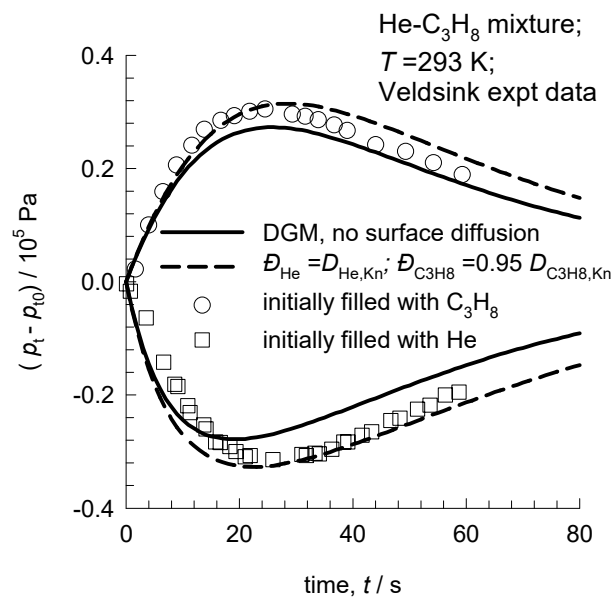
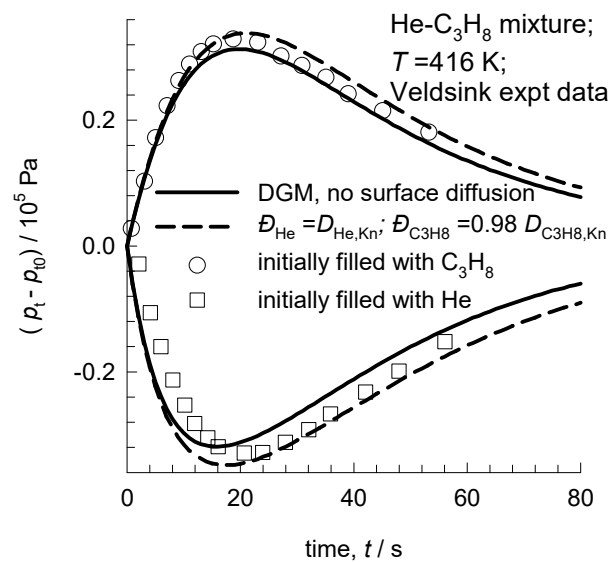
(a)



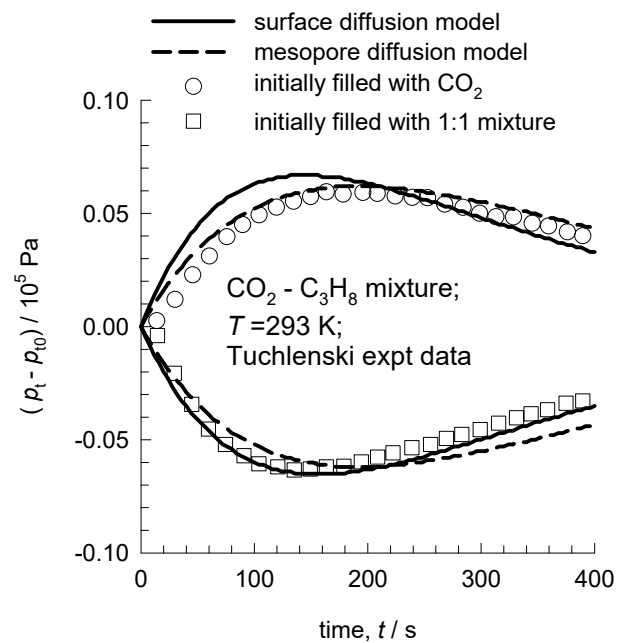
(b)



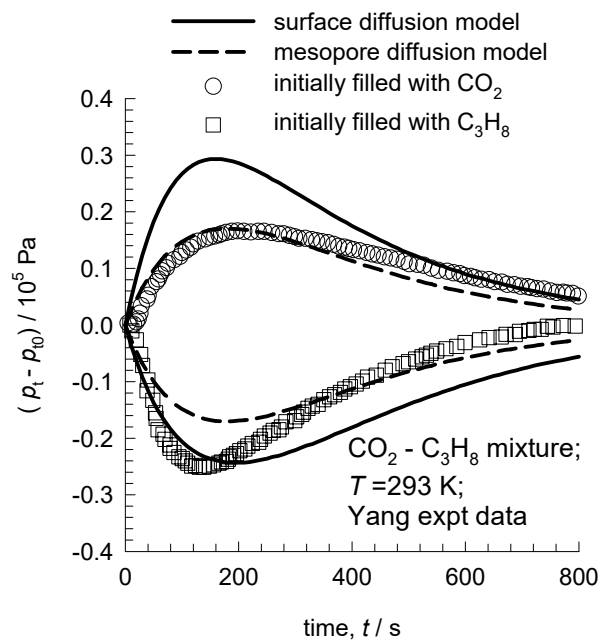
# Veldsink transient experiments

**(a)****(b)**

## Surface diffusion model for Tuchlenski expts



# Surface diffusion model for Yang expts



# Surface diffusion model for Yang expts

